Feasibility Study of a Natural Uranium Neutron Spallation Target using FLiBe as a Coolant

Andrew James Boulanger

Thesis submitted to the faculty of the Virginia Polytechnic Institute and State University in partial fulfillment of the requirements for the degree of

Master of Science

In

Mechanical Engineering

Mark A. Pierson (Chair)

Eugene F. Brown

Robert B. Vogelaar

May 10, 2011

Blacksburg, Virginia

Keywords: Neutron, Proton, Spallation, CFD, FLiBe, Uranium

Feasibility Study of a Natural Uranium Neutron Spallation Target using FLiBe as a Coolant

Andrew James Boulanger

Abstract

The research conducted was a feasibility study using Lithium Fluoride-Beryllium Fluoride (LiF-Be FLiBe as a coolant with a natural uranium neutron spallation source applied to an accelerator driven sub-critical molten salt reactor. The study utilized two different software tools, MCNPX 2.6 and FLUENT 12.1. MCNPX was used to determine the neutronics and heat deposited in the spallation target structure while FLUENT was used to determine the feasibility of cooling the target structure with FLiBe. Several target structures were analyzed using a variety of plates and large cylinders of natural uranium with a proton beam incident on a Hastelloy-N window. The supporting structures were created from Hastelloy-N due to their anti-corrosive properties of molten salts such as FLiBe and their resistance to neutron damage. The final design chosen was a "Sandwich" design utilizing a section of thick plates followed by several smaller plates then finally a section of thick plates to stop any protons from irradiating the bottom of the target support structure or the containment vessel of the reactor. Utilizing a proton beam with 0.81 MW of proton beam power at 1.35 mA with proton kinetic energies of 600 MeV, the total heat generated in the spallation target was about 0.9 MW due to fissions in the natural uranium. Additionally, the neutrons produced from the final design of the spallation target were approximately $1.25x10^{18}$ neutrons per second which were mainly fast neutrons. The use of a natural uranium target proved to be very promising. However, cooling the target using FLiBe would require further optimization or investigation into alternate coolants. Specifically, the final design developed using FLiBe as a coolant was not practically feasible due to the hydraulic forces resulting from the high flow rates necessary to keep the natural uranium target structures cooled. The primary reason for the lack of a feasible solution was the FLiBe as a coolant; FLiBe is unable to pull enough heat generated in the target out of the target structure. Due to the high energy density of a natural uranium spallation target structure, a more effective method of cooling will be required to avoid high hydraulic forces, such as a liquid metal coolant like lead-bismuth eutectic.

Acknowledgements

I would like to thank Dr. Mark Pierson for his input, recommendations and advice through this research as well as Dr. Eugene Brown and Dr. Bruce Vogelaar. I would like to thank the Nuclear Regulatory Commission Fellowship which allowed funding for this research. I would like to thank Matt Lippy and Debamoy Sen for their continual recommendations and advice. I would like to thank all my friends for their support throughout my college career.

I would like to thank my parents for constant support as well as my sister who had to deal with me as a roommate for two more extra years through my undergraduate and graduate studies.

Table of Contents

List of Figures

List of Tables

Chapter 1: Introduction

The research performed was intended to be a feasibility study towards a potential application of a natural uranium neutron spallation target using FLiBe as a coolant. Simple and complex geometries and scenarios were created to explore as many options as possible towards determining some degree of validity.

The purpose of this chapter is to provide adequate background for neutron spallation targets and their applications in Accelerator Driven Subcritical Reactors (ADSRs) in the specific application of GEM*STAR. An overview of an ADSR is provided as well as high level details concerning the purpose of a neutron spallation target.

Overview of Accelerator Driven Subcritical Reactors

Currently, the purpose of an Accelerator Driven Subcritical Reactor (ADSR) is to provide an alternative to transmute waste and provide energy. ADSRs fall under the category of a Generation IV nuclear reactor. Generation IV nuclear reactors are those which use more advanced technologies compared to the Generation III and III+ Pressurized Water Reactors (PWRs) and Boiling Water Reactors (BWRs). In addition, the various designs of Generation IV nuclear reactors allow for altered fuel cycles which minimize waste and increase power densities and power outputs of nuclear power plants. ADSRs can potentially alleviate issues with the current nuclear fuel cycle and can work in conjunction with the current and future nuclear reactors.

Basic Principals of Accelerator Driven Subcritical Reactor

Figure 1 shows a simple schematic of a typical ADSR. A proton accelerator produces a proton beam at a power of approximately one megawatt for potential commercial applications. The proton beam then imparts its energy on a neutron spallation target which is usually a heavy metal. When a proton enters the target and strikes the nucleus of the material in the spallation target, neutrons are spalled or effectively thrown out of the target nucleus. The neutrons then leave the target and enter the reactor fissionable material (typically uranium) which allows the reactor to produce energy through the subcritical multiplication of neutrons produced by the spallation target. When the accelerator is turned off the fissionable material cannot go critical which makes the system inherently safe.

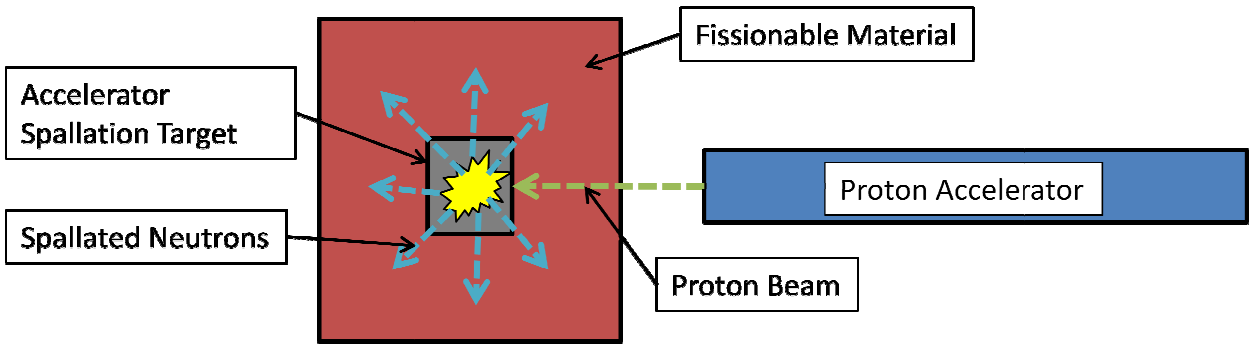

Figure 1: A basic schematic of a typical ADS system. The proton accelerator on the right produces a proton beam into an accelerator spallation target which produces fast and thermal neutrons which then interact with the fissionable material (typically Uranium) to produce heat which can be used to produce energy.

In order to make ADSR fission reactions sustainable, there is an energy feedback system into the proton accelerator. Figure 2 shows a schematic of the flow of energy for an ADSR system. The orange arrows indicate energy flow between various sections of a hypothetical ADSR power plant towards the power grid. The proton accelerator provides high energy protons for the target which then produces neutrons to allow for subcritical multiplication in the reactor and produce heat which can be turned into electricity. Some of the electricity is fed back into the proton accelerator while a majority of the energy goes to the power grid for commercial use.

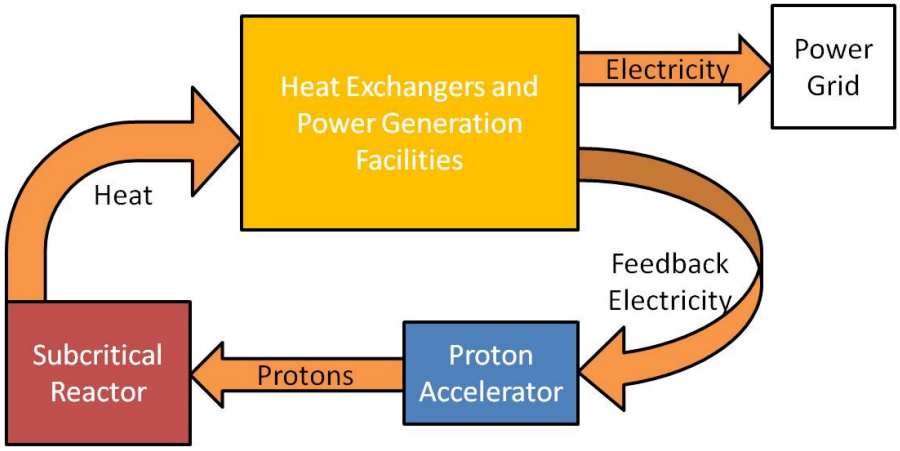

Figure 2: The flow of energy in a typical ADSR system. The process begins at the Proton Accelerator which accelerates protons towards a target in the Subcritical Reactor. The resulting fission reactors produce heat which is then utilized in the Heat Exchangers and Power Generation Facilities. Some of the power produced is then turned into Feedback Electricity to power the Proton Accelerator while a majority of the power is sent to the Power Grid for commercial use.

Proton Accelerator Background

Proton accelerators are a form of particle accelerators which are utilized for various scientific disciplines across the world. For the purposes of this paper, the discussion will be limited towards high energy protons with energies of several hundred mega-electron volts per particle. In order to obtain high energy levels, high frequency electric fields are necessary. These high frequency energy fields are obtained through cavities in the accelerator. These cavities essentially accelerate and increase the energy of the particle to sufficient levels before imparting their energy on a target.

Generally there are two types of accelerators, linear accelerators (linacs) and circular accelerators (synchrotrons). These two types of accelerators can be combined to reach higher energy levels as well. Figure 3 shows a simple flow diagram of how a linear accelerator works. A linear accelerator utilizes the high frequency cavities in series to increase the kinetic energy of the proton. Usually linacs are utilized for low level energy testing.

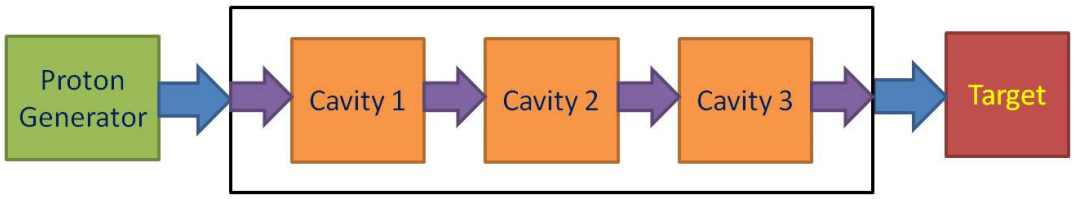

Figure 3: A simple diagram of a linear accelerator using a proton generator, three accelerator cavities and a target. The proton generator creates protons which are then accelerated in each of the cavities increasing the energy of the protons to appropriate levels before they impact the target.

In a linac, the proton only passes through those cavities once. Compared to a synchrotron, a particle can pass through the same cavity more than once which subsequently increases the energy of the particle to sufficient levels for testing. Figure 4 shows a simple flow chart of a proton synchrotron. Generally, linacs are used to initialize particle acceleration into a synchrotron where the energy levels are increased to much higher levels.

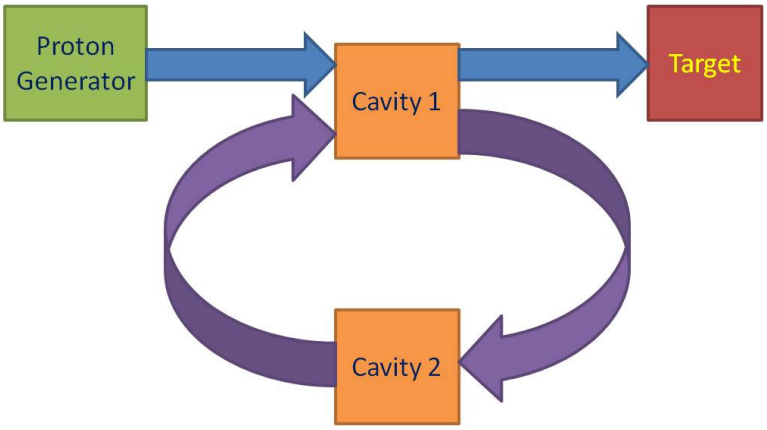

Figure 4: A simple flow diagram of a synchrotron. A proton generator sends the particle into a circular ring with resonance cavities which increase the proton energy to appropriate levels over multiple cycles. This diagram depicts two cavities, but there can be more cavities to increase the energy further. Once the energy is at the appropriate level, the protons are then directed at the target.

Neutron Spallation Basics

Essentially, a neutron spallation target multiplies the number of particles entering at high energy to many other particles at lower energies. Figure 5 shows a simple diagram of how neutron spallation works by impacting a proton onto a target nucleus. Conservation of energy still applies in this situation whether the energy transfer is elastic collisions, inelastic collisions or a mix of both. Ideally, a neutron spallation source would maximize the number of neutrons leaving the target. However, the recoil of the nuclei, which are impacted by the protons, results in heat generation in the target. Typically, neutrons, protons, photons, electrons and various heavy ions are produced from a spallation reaction. All of these particles then interact with the surrounding nuclei and cause heat generation as well as more spallation if the energy levels of the remaining particles are sufficiently high enough. For instance, the neutrons produced by the target can cause fission inside the target itself; if the material being spallated is a fissile material such as uranium. A fissile target can generate more heat than the beam power provides.

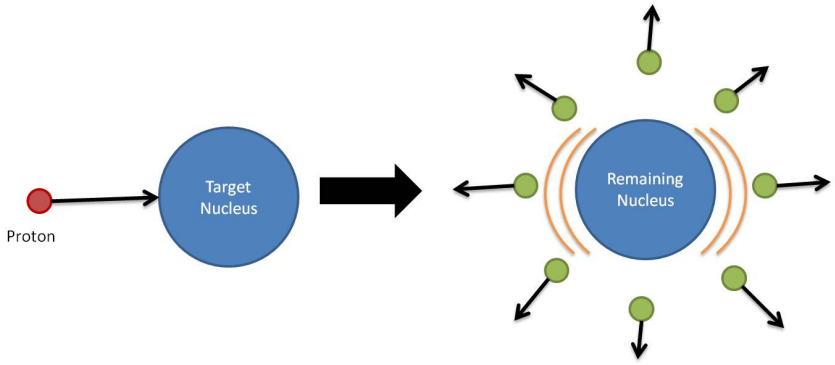

Figure 5: A simple diagram of a proton impacting a target nucleus. The nucleus then spallates neutrons and various other particles to rid itself of the excess energy. The remaining nucleus usually has a recoil energy which then produces heat.

Chapter 2: Literature Review

Resources associated with neutron spallation sources associated with ADSRs can be broken down into two major categories: principals of neutron spallation targets with respect to ADSRs and ADSR neutron spallation sources globally.

Principals of Neutron Spallation Targets and ADSRs

Neutron spallation targets are neutron sources for subcritical reactors. A subcritical reactor needs a continuous source of neutrons to cause sustainable fission in the subcritical blanket. A neutron spallation target functions by having a high energy proton impact a medium (either solid or liquid) and have the medium produce multiple neutrons per proton. The medium can also be considered a multiplying medium (Nifenecker, Meplan, & David, Accelerator Driven Subcritical Reactors, 2003). As described in Neutron Spallation Basics, the basic principal is to have a proton strike a target nucleus with a high enough energy to excite the nucleons to an energy level greater than their binding energy. Therefore, the nucleons will spallate off the nucleus into the medium or adjacent areas and materials.

To remove a nucleon from a nucleus, the energy imparted by the proton must exceed the binding energy of the neutron with the smallest binding energy to the nucleus. The binding energy of a nucleus can be calculated by first determining the total energy of the separate parts of the atom as seen in Equation (1)(Turner, 2007).

$$M(theoretical) = 931.49\frac{MeV}{AMU}\left(N_n\, M(n) + N_h\, M(h) + N_e\, M(e)\right) \quad (1)$$

Where *M(theoretical)* is the theoretical mass of the atom, N_n is the number of neutrons, N_h is the number of protons, N_e is the number of electrons, *M(n)* is the mass of a neutron, *M(h)* is the mass of a proton and *M(e)* is the mass of an electron. All masses are initially in atomic mass units (AMU) and then converted to MeV for *M(theoretical)*. The actual mass of the atom is calculated and usually referenced by accurate sources from experimental data. The two masses are then subtracted from each other as shown in Equation (2) (Turner, 2007).

$$TBE = M(theoretical) - M(actual) \quad (2)$$

Where *TBE* is the total binding energy of the atom and *M(actual)* is the actual mass of the atom being calculated. The total binding energy can then be divided by the atomic mass number to determine the average binding energy per nucleon. However, as nuclei decrease in size the average binding energy per nucleon will increase (assuming the target nucleus is heavier than iron) as shown in Figure 6 (Turner, 2007).

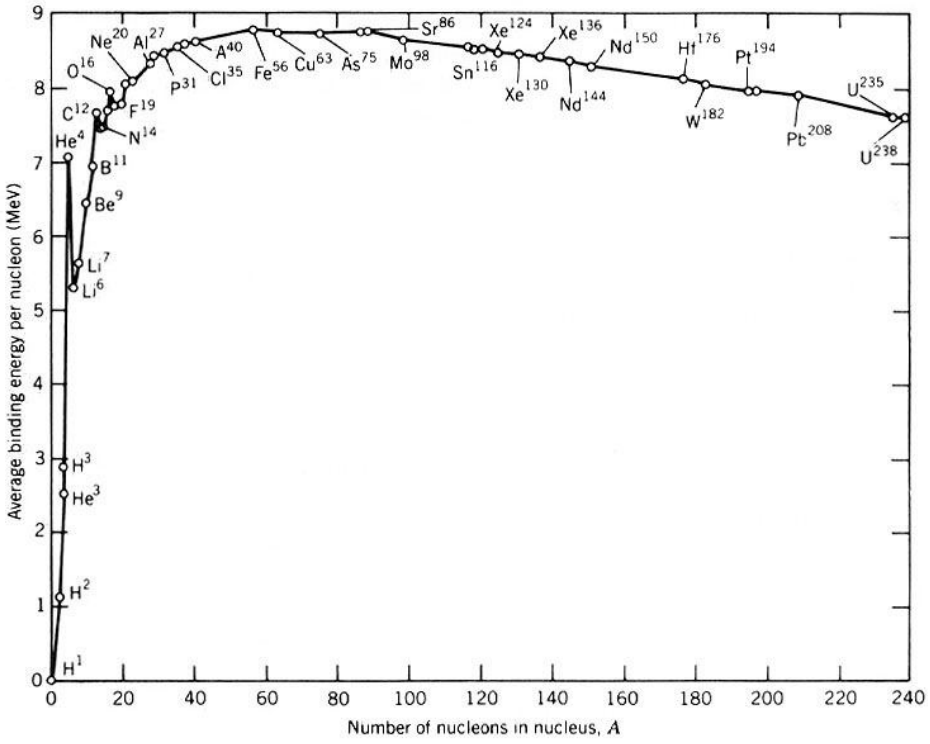

Figure 6: A trend line and various data points for the average binding energy per nucleon versus the atomic mass of an element, used under fair use guidelines, 2011 (Ask a Mathematician/Ask a Physicst, 2011).

Therefore, to calculate the energy required to remove one nucleon/neutron from a nucleus would be the smallest binding energy of a nucleon, known as the separation energy. Equation (3) shows the equation necessary to calculate the removal of one nucleon (Lamarsh & Baratta, 2001).

$$E_s = \left[M_n + M\left({}^{A-1}Z\right) - M\left({}^{A}Z\right)\right]931.49\ MeV/AMU \tag{3}$$

Where E_s (in MeV) is the binding energy or separation energy of the neutron which requires the least amount of energy to separate it from the nucleus, M_n is the mass of a neutron, $M({}^{A-1}Z)$ is the mass of an element with one less neutron, and $M({}^{A}Z)$ is the original mass of the nucleus. For example, the separation energy of ^{238}U is 6.153 MeV using data from the National Nuclear Data Center website (Audi, A.H., & C, 2003). Since the energy required to remove one neutron from a nucleus is approximately 6 MeV for a heavy element, combined with the data trends of binding energy shown in Figure 6; spallation utilizing protons at hundreds of MeV can produce significant quantities of high energy nucleons for further spallation and fission in an ADSR.

In an ADSR, a neutron source is available for the subcritical assembly. The neutrons produced from the spallation neutron source are the neutrons which cause the fissions inside the subcritical assemblies. Equation (4) shows the initial equation necessary to determine the secondary neutrons which were multiplied by the subcritical assembly (Nifenecker, Meplan, & David, ADSR Principals, 2003).

(4) $$N_1 = \frac{N_0}{(1-k)}$$

Where N_1 is the number of neutrons produced from the initial set of neutrons, N_0, and k is the multiplication factor of the multiplying medium or subcritical assembly. Maintaining a high neutron flux is necessary to maintain high power levels and a self sustaining reaction in an ADSR. For instance, the specific application of this research is for a thermal spectrum molten salt accelerator driven system called the Green Energy Multiplier Subcritical Technology for Alternative Reactors (GEM*STAR). For the extent of GEM*STAR, there will be two primary purposes, to burn up long lived trans-uranic elements and to provide enough energy to allow for a sustained reaction and economic production of power.

In order to produce enough neutrons to produce a long enough multiplication chain, a multiplying medium is necessary such as molten salt containing fissile fuel in a moderator in a subcritical design. This multiplying medium leads to an energy gain for the entire system which allows for heat to be produced and utilized for power generation facilities which feeds the proton accelerator and power grid if applicable. Equation (5) shows the energy gain of an ADSR system (Nifenecker, Meplan, & David, ADSR Principals, 2003).

(5) $$G = \frac{0.18\, k\, N_0}{v(1-k)E_p} = \frac{G_0 k}{1-k}$$

Where G is the energy gain of the system, v is the neutrons produced by low energy fissions which are approximately 2.5, E_p is the energy of the incident protons on the spallation target and G_0 is a constant dependent on the spallation material which is determined experimentally. The 0.18 coefficient comes from the kinetic energy of the spallation fragments which was determined by the CERN FEAT experiment (Nifenecker, Meplan, & David, ADSR Principals, 2003). The CERN FEAT experiment also determined that G_0k is approximately 3.0 for a uranium target which will be discussed in the section Neutron Spallation Sources Globally. By factoring in an ideal thermodynamic efficiency and the efficiency of high frequency cavities in the proton accelerator, an overall energy gain from a prospective ADSR power plant would be approximately 16 (Nifenecker, Meplan, & David, ADSR Principals, 2003).

The energy gain of an ADSR shown in equation (6) is for an ideal reactor in an infinite multiplying medium. However, in real world situations, there will be neutrons which will escape the reactor, similar to the comparison of a typical critical reactor where there is a difference between k_∞ and k_{eff}. Therefore, to calculate k_{eff} of an ADSR, the number of neutrons must be calculated which escape the reactor which is shown in equation (6) (Nifenecker, Meplan, & David, ADSR Principals, 2003).

(6) $$N_{esc} = \frac{N_0}{1-k_{eff}} \frac{k_\infty - k_{eff}}{k_\infty}$$

Where N_{esc} are the neutrons which escape, k_∞ determines the multiplication in an infinite medium and k_{eff} determines the multiplication in a finite medium. Determining the number of neutrons which escape

combined with the energy gain and the number of neutrons produced from the spallation source, a k_{eff} can be determined using simulations and empirical calculations. Equation (7) shows the number of fissions in a subcritical assembly which is used to determine the k value for the reactor (Kadi & A., 2006).

$$N_{fiss} = N_h \Gamma_h \frac{k}{(1-k)\nu} \tag{7}$$

Where N_{fiss} is the number of fissions in the sub-critical assembly, N_h is the number of fissions by high energy protons and Γ_h is the number of neutrons produced by high energy reactions in the assembly. Therefore, utilizing equation (8), the k value of the subcritical assembly can be determined from equation (8) which was found to be at least 0.7 for a lead spallation target at 1 GeV protons (Kadi & A., 2006).

$$k \geq \frac{1}{1 + \eta_{sp}\eta_b\eta_T \, E_f / (\nu E_p)} \approx 0.7 \tag{8}$$

Where k for this case is the multiplication factor, n_{sp} is the spallation neutron yield (material dependent), n_b is the electrical efficiency of the proton accelerator, n_T is the thermal efficiency of the power generation facilities, E_f is the energy generation per fission and E_p is the incident proton energy. Utilizing uranium, n_{sp} will be higher than lead which is approximately 30. In addition, this equation demonstrates that if the multiplication factor is increased above 0.7, by using more fissile material in the subcritical assembly, there is less proton current required to induce a sustaining fission scenario with a constant neutron source. However, for the purposes of this thesis and for GEM*STAR, a subcritical k_{eff} of 0.95 to 0.98 will be required to produce a large energy gain.

Neutron Spallation Sources Globally

There are many neutron spallation sources globally which are used for neutronics experiments or coupled ADSR systems. Many of the neutron spallation sources provide an insight as to the practical and feasible designs for ADSR systems.

The Spallation Neutron Source (SNS) at Oak Ridge National Labs (ORNL) utilizes a high energy proton beam which strikes a liquid mercury target to produce neutrons for scientific experiments across a broad range of disciplines. Unlike an ADSR, the SNS only houses a proton accelerator and a target. The neutrons emitted from the target are captured or utilized for various forms of neutron research. Table 1 shows the basic parameters of SNS. SNS utilizes four major components: the proton generator, the linear accelerator, the accumulator ring, and the spallation target. Not all the energy imparted on the target from the beam is turned into heat; a portion of the energy is utilized to produce neutrons.

Table 1: Various SNS parameters associated with the proton accelerator and mercury target (Oak Ridge National Lab, 2005).

Proton beam power on target	1.4 MW
Proton beam kinetic energy on target	1.0 GeV
Average beam current on target	1.4 mA
Pulse repetition rate	60 Hz
Protons per pulse on target	1.5×10^{14} protons
Target material	Liquid mercury
Target containment vessel material	Stainless steel

The target design of SNS utilizes liquid mercury as a neutron source because "(1) it is not damaged by radiation, as are solids; (2) it has a high atomic number making it a source of numerous neutrons (…); and (3) because it is a liquid at room temperature"(Oak Ridge National Lab). Figure 7 is a schematic of the SNS which depicts the mercury and water channels. In addition, the neutrons produced by the spallation target are moderated to low level neutrons. This is achieved by placing a water jacket around the spallation target. The fluid movement of the water and mercury allows for the system to be cooled effectively compared to a solid spallation source.

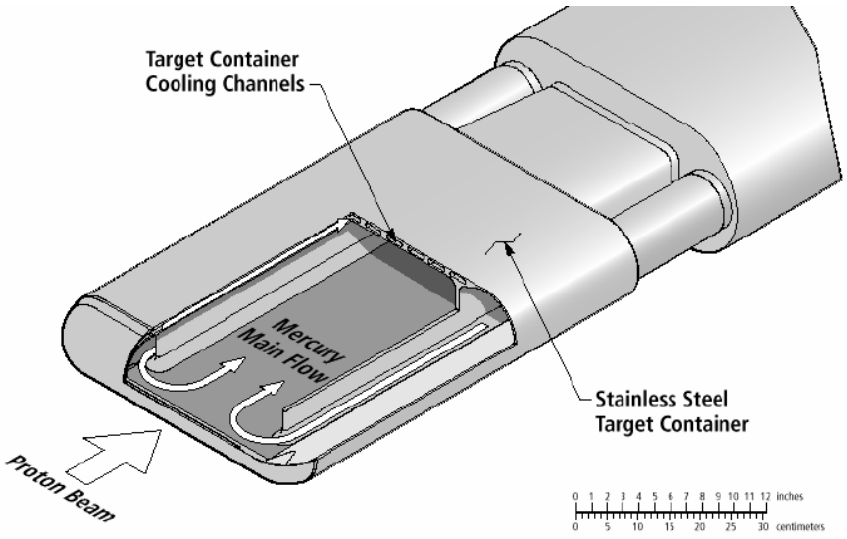

Figure 7: Is a schematic of the SNS liquid mercury target depicting the cooling channels around the main mercury flow. This structure would then be encapsulated in a water jacket to allow for additional cooling and the moderation of high energy neutrons, used under fair use guidelines, 2011 (Oak Ridge National Lab, 2006).

The SNS parameters list indicates the amount of heat and neutron flux associated with the design (Oak Ridge National Lab, 2005). The design in Figure 7 was meant to dissipate approximately 1.4 MW of thermal energy. The cross section of the beam on the target was approximately 7 centimeters by 20 centimeters with normal operating temperatures of 333 K to 363 K with an operating pressure of approximately 43 psi. The hull temperature of the target vessel was to be maintained below 200 °C

during operation. The operating temperatures of the neutron source indicated the high temperatures associated with neutron spallation sources for GEM*STAR at room temperatures.

The physical heating combined with high neutron and proton fluxes can alter the structural and thermal properties of the target containment vessel and associated structures. Figure 8 is a sample piece cut from the target where the proton beam was incident on the target vessel. The outer surface of the target appeared new before cleaning and sampling occurred. The damage on the inner surface of the cut samples were caused by cavitation of the mercury inside the target which was induced by the proton beam. However, the missing material was not accounted for in the filters of the system. This type of damage can limit the use of liquid targets unless extensive flow testing has occurred to determine cavitation areas. Additionally, the samples taken from the target were irradiated to approximately 10 rems per hour at one foot away during analysis (Ferguson, 2010). This particular design of the mercury target has embrittlement issues associated with the structures. Therefore, the neutron spallation target must be replaced periodically. Currently, ORNL is testing a rotational tungsten target as well as an updated SNS target (Ferguson, 2010).

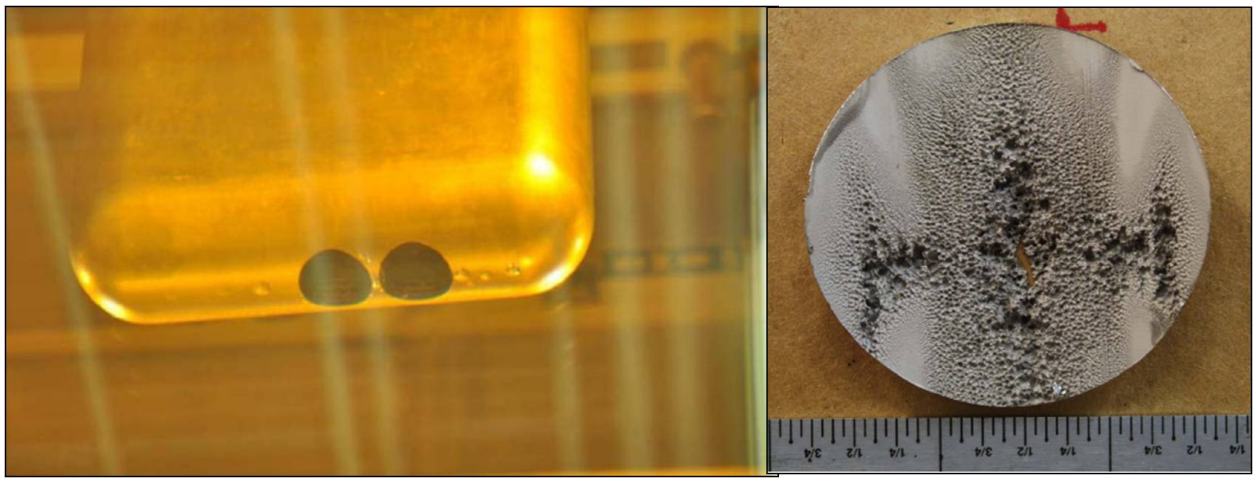

Figure 8: On the left are the samples cut from the SNS target at the area of the incident protons. The image on the right shows the cavitation damage caused by the mercury flow, used under fair use guidelines, 2011 (Ferguson, 2010).

The MEGAwatt PIlot Target Experiment (MEGAPIE) at the Paul Scherrer Institute (PSI) in Switzerland is another high profile neutron spallation source which utilized a liquid lead bismuth eutectic. The project was completed in December 2006 where dismantling and analysis was performed on the target.

MEGAPIE was a liquid lead-bismuth eutectic neutron spallation target for Swiss Neutron Spallation Source (SINQ) (Bauer, Salvatores, & Heusener, 2001). The initial neutron spallation at SINQ was a solid lead target with various experimental samples inside the target. MEGAPIE utilized a liquid target system similar to the SNS at ORNL. However, the setup at SINQ uses a vertical beam pointed upwards instead of a beam on a horizontal plane at SNS. MEGAPIE was placed in the middle of SINQ with the primary target

area at the bottom of the structure. Figure 9 is a schematic of the MEGAPIE neutron spallation source. The associated pumps and coolers of MEGAPIE are routed to the top of SINQ. The spallation material utilized for MEGAPIE was a liquid lead bismuth eutectic (LBE). Lead bismuth eutectic has a low melting point of 125 C and a boiling point at approximately 1600 C depending on the mixture of lead to bismuth.

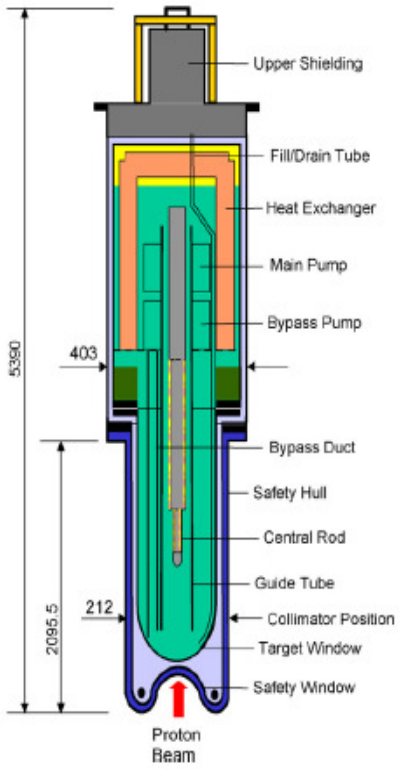

Figure 9: A cross section schematic of the MEGAPIE spallation neutron source at PSI (Smith, Leung, & Zucchini, 2007). Reprinted from Nuclear Engineering and Design, Vol 237, Coupled fluid/structure analyses of the MEGAPIE spallation source target during transients, pages 1656-1667, Copyright 2007, with permission from Elsevier.

MEGAPIE was designed to operate at a 1 MW beam power for an extended period of time to "demonstrate the safe operation of a liquid metal spallation target" (Paul Scherrer Institute, 2004). Figure 10 is an example temperature cross section depicting the heat generated inside the MEGAPIE target area. The design temperature of MEGAPIE was approximately 400 °C. Computational Fluid Dynamics (CFD) simulations were performed to determine the heat deposition in the target due to the energy deposited as heat in the flowing LBE and associated structures. The target area of MEGAPIE was approximately 20 centimeters across and 2 meters high. The majority of the energy was deposited in the target for approximately for the first 27 centimeters from the bottom of the target. Approximately 80% of the incident beam energy turns into heat in most accelerator spallation targets. Therefore, approximately 0.8 MW of heat energy is being deposited into a small volume of LBE which will require cooling to prevent boiling of the liquid and to prevent damage to the structural components of the target.

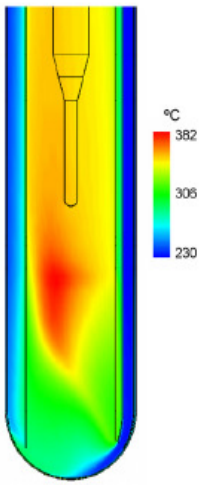

Figure 10: Steady state temperature cross section plot of the area with maximum energy deposition in MEGAPIE (Smith, Leung, & Zucchini, 2007). Reprinted from Nuclear Engineering and Design, Vol 237, Coupled fluid/structure analyses of the MEGAPIE spallation source target during transients, pages 1656-1667, Copyright 2007, with permission from Elsevier.

Upon dismantlement of the MEGAPIE neutron spallation source, there was significant material damage to the supporting structures associated with the primary energy deposition area (Ferguson, 2010). Using a high power proton beam indicated materials issues. Figure 11 is a comparison of the leak detector at the bottom of the MEGAPIE target window between before and after testing. The leak detector was severely damaged with dark unknown material deposits. Additionally, the beam window appeared to be whitish. The damage to the support structure materials leads to great concern to the longevity of a solid spallation target as well as temperatures associated with the structures in corrosive environments.

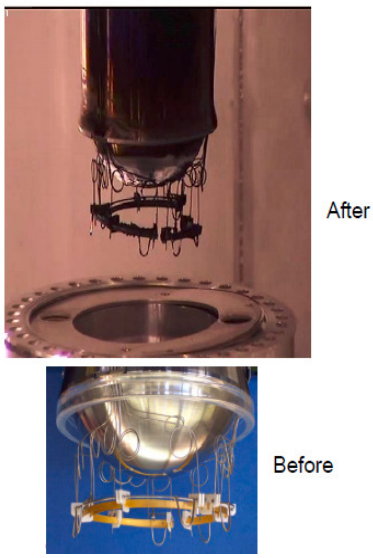

Figure 11: A before and after picture of the leak detector of MEGAPIE between the beam window and safety hull of the structure which depicts significant thermal and neutronics damage, used under fair use guidelines, 2011 (Ferguson, 2010).

MEGAPIE was deemed a success in determining the feasibility of using a liquid neutron spallation source for the application of an ADSR. MEGAPIE offered significant insight into the thermal and neutronics associated with high power neutron spallation targets for GEM*STAR. The high temperatures associated with MEGAPIE provided significant evidence towards a practical high temperature spallation target.

The Reactor Accelerator Coupling Experiments (RACE) Project was based around the investigation using an accelerator driven subcritical reactor system which took place from 2003 to 2006. The experiments began at Idaho State University (ISU) at the Idaho Accelerator Center and were concluded at the University of Texas (UT) at Austin (Beller, et al., 2006).

The RACE Project utilized a 25 MeV electron accelerator with a tungsten copper target on the side of a subcritical reactor assembly (Idaho Accelerator Center, 2007). The target produced 10^{10} to 10^{12} neutrons per second which can be used for fission reactions in the subcritical core. The reactor (also known as TRIGA) was designed to operate up to 1 MW_{th} and operated at a k_{eff} from complete shut down to 0.92. When the reactor was moved to UT, follow up experiments were performed from a k_{eff} of 0.92 up to critical (Beller, et al., 2006). The reactor was setup with various geometries and 2 primary types of fuels: 1) a 20% enriched uranium-aluminum alloy at ISU and 2) "FLIP" fuel (UZr-H) at two enrichments of 20% and 70% at UT (O'Kelly, 2008). Figure 12 was the setup associated with the RACE experiments which includes the electron accelerator and subcritical core.

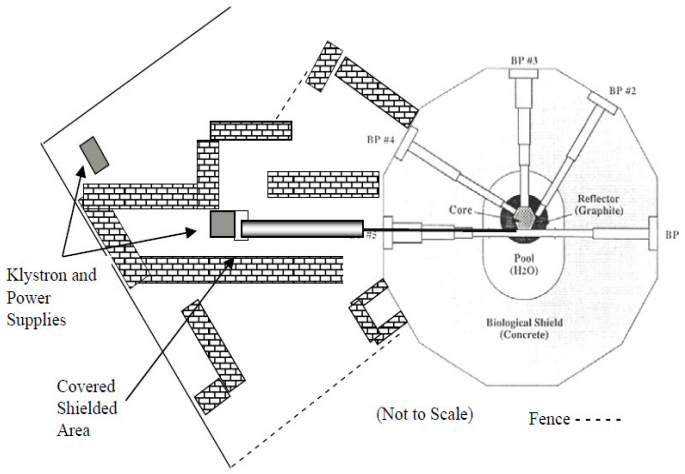

Figure 12: Is a not-to-scale schematic of the RACE couple experiment with the electron accelerator and subcritical core depicting several neutron beam windows for measurements, used under fair use guidelines, 2011 (O'Kelly, 2008).

Since funding was cancelled for the RACE project in 2006, no further work has been attempted to produce the planned high power RACE reactor with a 50 to 150 MW_{th} capability. A spallation target of tungsten plates was constructed at the University of Nevada, Las Vegas. The high powered experiments would allow $5x10^{13}$ to $5x10^{14}$ neutrons per second. The beam power utilized was approximately 20 kW which would be much less than the desired beam power of a proton beam associated with a natural uranium target. However, the tungsten plates required about 12 gallons per minute of de-mineralized

water with a flow velocity per plate of 2.52 meters per second with a temperature increase of the water coolant of 39 K (LeCounte, 2007).

Like MEGAPIE, RACE provided insight into coupling a neutron spallation target with a subcritical blanket core. Despite primary differences in the neutron spallation mechanism of an electron accelerator instead of a proton accelerator, the feasibility of an ADSR using a solid target for low power applications could allow for relatively high power applications as demonstrated in the research performed by Ryan LeCounte (LeCounte, 2007). In addition, the neutron spallation material was tungsten as opposed to the desired natural uranium for this research.

The CERN First Energy Amplifier Test (FEAT) was the first to couple a proton accelerator to a subcritical blanket (Nifenecker, Meplan, & David, Accelerator Driven Subcritical Reactors, 2003). Tests were performed to determine the energy gain from a proton's kinetic energy from 600 MeV through 3 GeV for a natural uranium spallation target. Their target used 3.6 tons of natural uranium which were placed in aluminum cladding which was then immersed in a normal water bath which acted as a moderator. The idea behind the test was to provide the energy gain associated with a spallation source from a spallation target. Figure 13 shows a plot of the energy gain based on the incident proton kinetic energy for the experiment (Kadi & A., 2006). The average energy gain from the CERN FEAT experiment was approximately 30 for proton kinetic energies above 1 GeV.

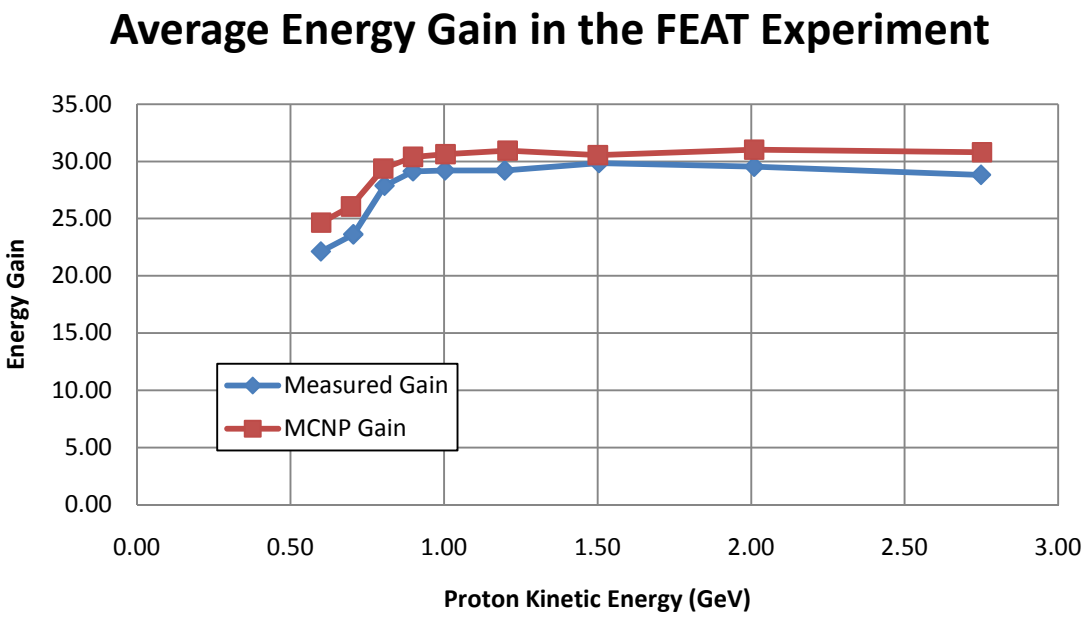

Figure 13: The energy gain of the FEAT experiment based on the proton kinetic energy, used under fair use guidelines, 2011 (Kadi & A., 2006).

Equation (9) shows the gain equation to be approximately 30 for the FEAT experiment using a G_0 of 3 and a k of 0.9 in accordance to the results obtained from Figure 13.

(9) $$G = \frac{G_0}{(1-k)}$$

The idea behind the CERN FEAT experiment was to use an ADSR to transmute waste from typical reactors in use today. A secondary benefit was to prove that an ADSR can provide enough heat to run a small power generation facility. The proof of concept from the CERN FEAT experiment was to demonstrate the elimination of typical control rods in critical reactors. The accelerator would provide the method of controlling the reactor during operations which would potentially allow for a reduction in cost and complexity of a potential ADSR system.

The FEAT experiment provided insight into using natural uranium as a spallation target for an ADSR which has great applications towards this feasibility study. Despite the relative direct application to GEM*STAR there were limited materials concerning the thermohydraulics of the spallation target associated with FEAT.

Chapter 3: GEM*STAR

The Green Energy Multiplier*Subcritical Technology for Alternative Reactors (GEM*STAR) is an ADSR design developed by the Accelerator Driven Neutron Applications Corporation (ADNA Corp). Currently, GEM*STAR is a subcritical thermal spectrum reactor utilizing a molten salt fuel within a graphite matrix. GEM*STAR operates at a k_{eff} between 0.95 to 0.99 depending on the recycling stage and the fissile fuel utilized. The design of GEM*STAR is not finalized at this point; however, GEM*STAR will utilize at least one proton accelerator to place a beam on the neutron spallation target. The accelerator power requirements can be supplemented by "green" sources of energy such as solar, wind or hydro electric sources.

The molten salt used by GEM*STAR is a uranium or thorium fluoride eutectic in a lithium-fluoride molten salt which is referred to as the enriched fuel salt. The advantage of utilizing a molten salt in a graphite matrix is a relatively uniform burn-up of the enriched fuel salt. The fuel salt is localized in the graphite matrix. The entire structure which contains the fuel salt will most likely use a modified Hastelloy-N alloy (Vogelaar & Bowman, 2010).

GEM*STAR utilizes several key technologies such as molten salt fuel, corrosion-resistant materials, graphite moderator, neutron spallation target and proton accelerators. The data obtained for the GEM*STAR research hinges on the Molten Salt Reactor Experiments which were completed at Oak Ridge National Labs in 1964 (Oak Ridge National Laboratory, 1964). The research associated with this thesis is primarily concerned about the thermohydraulics associated with the neutron spallation target.

Figure 14 shows a conceptual design of GEMSTAR. There could be two proton accelerators which will impart their energy on a natural uranium spallation source which is approximately in the center of the graphite matrix. The diagonal tubes contain the proton beams which then impact the spallation source. For the purposes of this feasibility study, the final beam path is assumed to be vertical with protons moving in the downward direction to simplify the design constraints (Vogelaar B. , 2010).

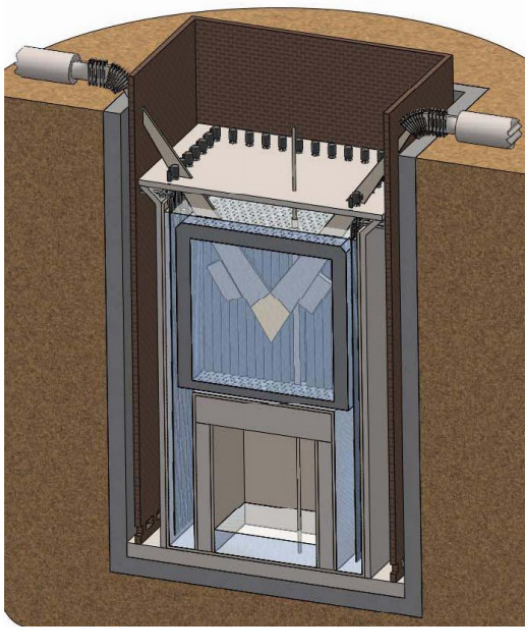

Figure 14: A conceptual design of GEM*STAR which is an underground reactor with two proton beams imparting their energy on a natural uranium neutron spallation target, used under fair use guidelines, 2011 (Vogelaar B. , 2010).

Chapter 4: Neutronics and Thermohydraulic Simulation Programs

This chapter will discuss the two primary programs, MCNPX 2.6 and FLUENT 12.1, utilized for the research associated with the feasibility study of using a natural uranium target with FLiBe as a coolant with a one MW proton beam.

MCNPX 2.6

MCNPX 2.6 is a Monte Carlo based radiation transport code created at the Los Alamos National Laboratory. The Monte Carlo method is a statistical random sampling method which utilizes a set of algorithms. MCNPX is a subset of a larger MCNP. MCNP has been developed over the course of approximately 70 years. In 1997, MCNPX 1.0 was developed for high energy particle modeling (Hendricks & Schwarz, 2010). MCNPX 2.6 is a more comprehensive code which includes many more nuclear database libraries than the original code. MCNPX has the ability to design complex geometries, generate particle sources, take various particle and physical tallies, and determine k value of a simulated nuclear reactor.

Even though MCNPX is a powerful piece of software, there are limitations surrounding the Monte Carlo method and the implementation of the code. The two main concerns are the particle physics limitations and statistical variance reduction.

Capabilities

MCNPX uses an input file which contains three primary sections. The first two sections are utilized to create the geometry of the simulation. The last section in the input file contains the information necessary to run the simulation, e.g. particle sources, particle tallies, variance reduction settings, particle physics, materials utilized, etc. Relatively complex geometries can be manually created in MCNPX. For example, large lattice structures can be created for criticality calculations. Additionally, a program was created called VISED which is a Graphical User Interface (GUI) for MCNPX. VISED can import extremely complex geometries from many common Computer Aided Design (CAD) programs.

Materials of these structures can be manually created using a simple programming method by describing the weight or atomic fractions of each element available or by utilizing an automatic generator in VISED from the data libraries available. The material database contains specific elements with varying libraries which can be utilized for the calculations.

In order to utilize these geometries for radiation transport simulations, there are several particles which can be utilized from low energy photons to high energy heavy ions which are listed in Table 2. MCNPX has the ability to use multiple particles for any simulation depending on the user's need. Each particle available for use will interact with different materials in different ways at various energy levels. The particle and material reactions are dependent on model or test data available in the MCNPX libraries. The particle model interactions will be described in the limitations section.

Table 2: A list of the available particles for MCNPX simulations (LANL, 2008).

Neutron	Anti-neutron	Photon	Electron
Positron	$Muon^-$	$Anti\text{-}muon^-$	Tau^-
Electron neutrino	Anti-electron neutrino	Muon neutrino	Tau neutrino
Proton	Anti-proton	$Lambda^0$	$Sigma^+$
$Sigma^-$	$Cascade^0$	$Cascade^-$	$Omega^-$
$Lambda_c^+$	$Cascade_c^+$	$Cascade_c^0$	$Lambda_b^0$
$Pion^+$	$Pion^-$	Neutral pion	$Kaon^+$
$Kaon^-$	K_0 short	K_0 long	D^+
D^0	D_s^+	B^+	B^0
B_s^0	Deuteron	Triton	Helium-3
Helium-4 (alpha)	Heavy ions		

Particle sources must be defined in order to perform radiation transport simulations. MCNPX has the ability to define various types of sources such as volume and surface sources. In addition, MCNPX has the ability to define source strengths and energies with various distributions across volumes and surfaces. In addition, MCNPX can produce multiple sources with multiple particles.

Producing various particles in geometries is only useful if data can be taken at various points in space, surfaces or volumes. The data taken in MCNPX encompasses fluxes, and energy deposition through various tallies. Table 3 shows the various tally types and their descriptions which can be used in MCNPX. The tallies can be used with almost any particle available in MCNPX for various energies.

Table 3: The types of tallies used in MCNPX, their description and the units used (LANL, 2008).

Tally Name	**Description**	**Units**
F1:<pl>	Current integrated over a surface	Particles
F2:<pl>	Flux averaged over a surface	$Particles/cm^2$
F4:<pl>	Flux averaged over a cell/volume	$Particles/cm^2$
F5a:N or F5a:P	Flux at a point or ring detector	$Particles/cm^2$
F6:<pl>	Energy deposition averaged over a cell	MeV/g
+F6	Collision heating	MeV/g
F7:N	Fission energy deposition averaged over a cell	MeV/g
F8:<pl>	Energy distribution of pulses created in a detector by radiation	Pulses
+F8:<pl>	Deposition	charge

In addition to normal tallies, there are four special tallies called mesh tallies which provide an overlaying mesh onto the geometry where data is taken in the simulated mesh cells of the problem. The four types of special tallies are called, (1) track averaged mesh tally, (2) source mesh tally, (3) energy deposition mesh tally, and (4) DXTRAN mesh tally. For the purposes of this paper, the energy deposition tally is of most importance. The energy deposition tally can limit itself to one particle or the total number of particles being utilized in the problem. In addition, there are three types of mesh structures, (1) a mesh

based on the typical Cartesian coordinate system (x-y-z), (2) a mesh based on the cylindrical coordinate system and (3) a mesh based on the spherical coordinate system. Each mesh system and mesh tally type can be determined by the user for optimizing their problem solution.

In addition to individual particle and small simulation models, MCNPX has the ability to determine the criticality of a system. MCNPX has the ability to calculate the k_{eff} of a system which is important for simulating reactors of various types. However, despite this useful feature, multiplication factors are beyond the scope of the research performed for this paper.

Limitations

MCNPX covers a wide variety of physics associated with particle interactions. However, MCNPX uses a combination of evaluated nuclear data and models/tables. The evaluated nuclear data only covers a limited range of energies. As the data becomes available, MCNPX has the ability to incorporate those libraries for use. However, in the meantime, MCNPX uses models or theoretical tables to calculate values beyond the energy range of the libraries. Table 4 shows the energy ranges applicable to the libraries for the four major types of particles. Beyond these limits, models are utilized. These models can be accurate or inaccurate which is why MCNPX is increasing the library size to cover a larger energy range for various particles.

Table 4: The 4 common sub atomic particles utilized in MCNPX. They are neutrons, photons, electrons and protons. The energy values are the energy ranges associated with evaluated nuclear data for running MCNPX simulations (Hendricks & Schwarz, 2010).

Particle	Minimum Energy	Maximum Energy
Neutrons	0 eV	150 MeV
Photons	1 keV	100 GeV
Electrons	1 keV	1 GeV
Protons	1 keV	150 MeV

The second limitation to MCNPX is the efficiency of the program itself. The efficiency of calculating a problem can be defined in MCNPX as the Figure of Merit (FOM). The FOM is shown in equation (10).

$$FOM \equiv \frac{1}{R^2 T} \tag{10}$$

Where FOM stands for Figure of Merit, R^2 is the relative error associated with a problem and T is the running time of the problem. The basic principal is to maximize this number by decreasing the relative error and/or decreasing the calculation time. The process of increasing the FOM is called variance reduction. There are four main types of variance reduction: (Hendricks & Schwarz, 2010)

1. Truncation method: provides energy cutoffs for various particles addressed in a problem
2. Population control method: controls the data samples taken in regions by utilizing particle splitting and Russian roulette which will be discussed.
3. Modified sampling method: increases the number of samples per particle

4. Partially deterministic method: bypasses the normal “random walk process” of a particle.

The advantage of variance reduction is significantly less computational times. However, there is more effort required by the user to manipulate the code and outputs to allow for shorter run times and more accurate data for a problem. There is no ideal FOM value for problem simulations. The maximum FOM value for a particular problem depends on the problem design and the acceptable accuracy deemed by the user.

Applications to Neutron Spallation Targets

MCNPX has the ability to model significant features surrounding a neutron spallation target in an ADSR. Generally, to model a neutron spallation target, the primary concern is maximizing neutron production. However, maximizing neutron production leads to heat production inside the target. To account for the energy deposition, an energy deposition tally can be utilized to determine the amount of heat deposited into neutron spallation source.

FLUENT

ANSYS FLUENT is a software product which is used to model fluid flows, heat transfer, and turbulence in various applications. For the purposes of this research, ANSYS FLUENT was utilized in modeling the thermo-hydraulics for the associated neutron spallation target cooling fluid. For the purposes of this research there were three primary areas in FLUENT which were of concern, basic fluid flow, turbulence, and heat transfer and solver theory. In addition, FLUENT is able to solve equations in both steady state and transient systems.

Basic Fluid Flow

For basic fluid flow in FLUENT, the continuity (mass conservation) and momentum equations must be satisfied to allow for convergence. Equation (11) shows the continuity equation which essentially states that the mass into the test system must equal the mass exiting the system. Equation (11) applies for both compressible and incompressible flows (Bejan, 2004).

$$\frac{\partial \rho}{\partial t} + \nabla(\rho \vec{v}) = 0 \tag{11}$$

Where ρ is the density and v is the velocity. In addition to continuity, momentum in the system is also conserved. Equation (12) is the general form in vector notation of the momentum conservation equation. A force balance is necessary for proper modeling of fluid flow in a system (Bejan, 2004).

$$\rho \frac{D\vec{v}}{Dt} = -\nabla P + \mu \nabla^2 \vec{\mathrm{v}} + \vec{\mathrm{F}} \tag{12}$$

Where $\vec{v}$ is the velocity of the fluid, *P* is the pressure, μ is the viscosity and $\vec{F}$ are the body forces on the fluid. For the purposes of this research, FLUENT has the capabilities of modeling inviscid flows, compressible flows, periodic flows and rotating flows. The user's inputs decide the validity of various models associated with a problem. In addition to basic fluid modeling, turbulence modeling is within the capability of FLUENT.

There are several models with various settings which can be utilized in FLUENT to obtain the proper answer. For the purposes of this research, the particular turbulence model is the k-ε model. The k- ε model is one of the more common models utilized for a majority of turbulent fluid flows which assumes completely turbulent flows. The k- ε model utilizes two equations, the k-equation and the ε-equation. The k-equation (equation (13)) is determined from the momentum equations which is essentially the turbulent kinetic energy. The ε-equation (equation (14)) is determined from a length scale and effectively acts as the turbulent dissipation of the k-equation to find equilibrium (Bejan, 2004).

(13) $$k = \frac{1}{2}[\overline{(u')^2} + \overline{(v')^2} + \overline{(w')^2}$$

(14) $$\varepsilon = C\, k^{1/2}\, L$$

Where k is the turbulent kinetic energy, and u, v and w are the turbulent velocities in the x, y, and z, directions respectively; where ε is the turbulent dissipation rate, C is a constant, and L is the length scale of the system being tested.

Turbulence: Standard k-ε Model

Within FLUENT there are three primary version of the k-ε model, the standard model, the RNG, and the realizable model. The standard model is the simplest model of the three primary models. For FLUENT, equations (15) and (16) are the transport equations for the fluid flow assuming a steady state condition. Equation (17) shows the equation to determine the turbulent viscosity (CFD Online, 2007).

(15) $$\frac{\partial}{\partial x_i}(\rho k u_i) = \frac{\partial}{\partial x_j}\left[\left(\mu + \frac{\mu_t}{\sigma_k}\right)\frac{\partial k}{\partial x_j}\right] + P_k + P_b - \rho\varepsilon - Y_M + S_k$$

(16) $$\frac{\partial}{\partial x_i}(\rho \varepsilon u_i) = \frac{\partial}{\partial x_j}\left[\left(\mu + \frac{\mu_t}{\sigma_\epsilon}\right)\frac{\partial \varepsilon}{\partial x_j}\right] + C_1\frac{\varepsilon}{k}(P_k + C_3 P_b) - C_2\rho\frac{\varepsilon^2}{k} + S_\varepsilon$$

(17) $$\mu_t = \rho C_\mu \frac{k^2}{\varepsilon}$$

Where ρ is the density, k is the turbulent kinetic energy, ε is the turbulent dissipation rate, μ is the viscosity, μ_t is the turbulent viscosity, σ_k is the turbulent Prandtl number for k, σ_ε is the turbulent Prandtl

number for ε, P_k is the generation of turbulent kinetic energy from velocity gradients, P_b is the turbulent kinetic energy due to buoyancy forces, Y_M is the ratio of the fluctuating dilation in compressible turbulence to overall dissipation rate, S_k and S_ε are user defined sources. For the standard k-ε model, there are five constants (C_1, C_2, C_μ, σ_k, and σ_ε) indicated by equation (15) and equation (16).

Appendix A: General Equations show the associated equations necessary to solve equations (15) and (16). Table 5 shows the five constants which control the k-ε model.

Table 5: Constants for the standard k-ε model.

C_1	1.44
C_2	1.92
C_μ	0.09
σ_k	1.0
σ_ε	1.3

Turbulence: Re-Normalization Group (RNG) k-ε Model

The second model utilized in FLUENT is called the RNG k-ε model. The RNG method stands for the Re-Normalization Group (RNG) method which renormalizes the Navier-Stokes equations. The renormalization of the Navier-Stokes equations takes account of the smaller scales of motion which the standard model lacks. The equations from the RNG model are similar to the standard model. However, equations (18) and (19) show the differences compared to the standard model. (CFD Online, 2007)

(18) $$\frac{\partial}{\partial x_i}(\rho k u_i) = \frac{\partial}{\partial x_j}\left[\alpha_k \mu_{eff}\frac{\partial k}{\partial x_j}\right] + P_k + P_b - \rho\varepsilon - Y_M + S_k$$

(19) $$\frac{\partial}{\partial x_i}(\rho \varepsilon u_i) = \frac{\partial}{\partial x_j}\left[\alpha_k \mu_{eff}\frac{\partial \varepsilon}{\partial x_j}\right] + C_1\frac{\varepsilon}{k}(P_k + C_3 P_b) - C_2{}^*\rho\frac{\varepsilon^2}{k} + S_\varepsilon$$

(20) $$C_2^* = C_2 + \frac{C_\mu \eta^3\left(1 - \frac{\eta}{\eta_0}\right)}{1 + \beta\eta^3}$$

(21) $$\eta = \frac{Sk}{\varepsilon}$$

(22) $$S = \sqrt{2S_{ij}S_{ij}}$$

Where α_k is the inverse effective Prandtl number for k, α_ε is the inverse effective Prandtl number for ε, μ_{eff} is the effective turbulent viscosity and C_2^* is a modified constant for the RNG model shown in equation (20). Equation (21) shows the η term to calculate C_2^* and equation (22) shows that S is a tensor. More equations associated with this model can be found in

Appendix A: General Equations. Table 6 shows the constants associated with the RNG turbulence model that FLUENT utilizes.

Table 6: Constants for the k-ε RNG model.

C_1	1.42
C_2	1.68
C_μ	0.0845
σ_k	0.7194
σ_ε	0.7194
η_0	4.38
β	0.012

Turbulence: Realizable k-ε Model

The primary solver utilized for this paper was the realizable k-ε model. This model is able to satisfy constraints on the Reynolds stresses which follow the physics of turbulent flows. The two main differences between the standard and RNG model are that there is a new formulation of turbulent viscosity and there is a new transport equation for ε. Equations (23) and (24) show the transport equations utilized for the realizable model for the steady state condition. Equation (23) is the same as the standard model.

$$\frac{\partial}{\partial x_i}(\rho k u_i) = \frac{\partial}{\partial x_j}\left[\left(\mu + \frac{\mu_t}{\sigma_k}\right)\frac{\partial k}{\partial x_j}\right] + P_k + P_b - \rho\varepsilon - Y_M + S_k \tag{23}$$

$$\frac{\partial}{\partial x_i}(\rho \varepsilon u_i) = \frac{\partial}{\partial x_j}\left[\left(\mu + \frac{\mu_t}{\sigma_\epsilon}\right)\frac{\partial \varepsilon}{\partial x_j}\right] + \rho C_4 S\varepsilon - \rho C_5 \frac{\varepsilon^2}{k + \sqrt{\nu\varepsilon}} + C_1 \frac{\varepsilon}{k} C_3 P_b + S_\varepsilon \tag{24}$$

The turbulent viscosity for the realizable model is the same as the standard model (equation (17)). However, the major difference is that C_μ is no longer constant. The equations associated with the realizable model can be found in

Appendix A: General Equations. Table 7 shows the associated constants with the realizable model.

Table 7: Constants for the k-ε RNG model.

C_1	1.44
C_5	1.9
σ_k	1.0
σ_ε	1.2

The advantage of the realizable k-ε model compared to the standard model is the ability to effectively map rotational flows and boundary layers under high pressure gradients, separation and recirculation flows. The consequence of using the realizable model in FLUENT is that the models utilized can potentially increase the turbulent viscosity to extreme values to allow for convergence of the model. The turbulent viscosity will be limited by FLUENT to a certain number until the model begins to converge.

Heat Transfer Theory

For the purposes of this paper, the two primary modes of heat transfer which were considered are conduction and convection. Radiation heat transfer is beyond the scope of this research. Conduction in FLUENT is Fourier's Law of Conduction which is shown in equation (25).

(25) $$Q_{cond} = -k\,A\,\frac{dT}{dx}$$

Where *k* is the thermal conduction of the material, *A* is the area, and $\frac{dT}{dx}$ is the thermal gradient across the material. FLUENT is able to model conduction through both solid materials and fluids. In terms of convection, there are two primary methods, either forced or natural convection. For the purposes of this research, natural convection was not a major concern. Convection is described by Newton's Law of Cooling which is depicted in equation (26).

(26) $$Q_{conv} = h\,A\,dT$$

Where Q_{conv} is the heat transferred through convection, *A* is the area, *h* is the convection heat transfer coefficient and *dT* is the temperature difference between the solid and surrounding fluid. The convection heat transfer coefficient is the difficult portion of convective heat transfer to determine. The area exposed to the fluid flow, temperature difference, fluid velocity, and fluid properties all affect *h* and the convective cooling. A dimensionless number utilized to describe the convection heat transfer is the Nusselt number, shown in equation (27).

(27) $$Nu = \frac{h\,L}{k}$$

Where Nu is the Nusselt number, h is the convective heat transfer coefficient, L is the length scale and k is the thermal conductivity of the fluid. Generally, the Nusselt number is a function of the Reynolds, Prandtl and Grashof numbers. In addition, if Nu = 1, there is only pure conduction occurring between the solid and the fluid. Using the Grashof, Reynolds, and Nusselt number, either forced convection, natural convection or mixed convection can be described using the conditions shown in Table 8 (CFD Online, 2007).

Table 8: The various conditions which dictate convection modes of either forced, natural or mixed convection.

Forced Convection	$Nu = f(Re, Pr)$	$\frac{Gr}{Re_L^2} \ll 1$
Natural Convection	$Nu = f(Gr, Pr)$	$\frac{Gr}{Re_L^2} \gg 1$
Mixed Convection	$Nu = f(Re, Pr, Gr)$	$\frac{Gr}{Re_L^2} = 1$

Solver Theory

In FLUENT, there are two primary solvers, which are either pressure based or density based. The pressure based solver is utilized for incompressible, low speed flows, while the density solver is used for high speed flows which can be compressed. For the version of FLUENT utilized for this research, either solver overlaps in their capabilities for various flows.

Chapter 5: Materials Utilized in the Neutron Spallation Target for GEM*STAR

For the design and simulation purposes of this research, there were three primary materials which were utilized. The three materials were:

1) Lithium Fluoride – Beryllium Fluoride (LiF-BeF_2) or FLiBe
2) Hastelloy-N
3) Natural Uranium

FLiBe was chosen because of the similarities to lithium fluoride which will be used in the fuel salt of GEM*STAR. The fuel salt uses a mix of LiF:UF4 in a ratio of approximately 70:30. FLiBe has similar properties to the fuel salt which would lend itself to be an ideal choice to simplify the design of the spallation target by using a natural uranium target and FLiBe as a coolant. The melting temperature of FLiBe is approximately 732 K, while the necessary melting point of the fuel salt is around 932 K. (Vogelaar & Bowman, 2010) Therefore, for practical purposes, the spallation target can be heated and melted and set in a steady state thermohydraulic setting before the heaters melt the fuel salt and bring the reactor up to operating temperature. In addition, FLiBe has about twice the density of water and a relatively high heat capacity. The ability to remove heat from the target was essential because at a minimum, the heat generated in the target would be approximately 1 megawatt. Cooling a target about 20 centimeters in diameter and 10 to 100 centimeters tall requires a liquid which can remove heat effectively. Appendix B: Material Properties contains the data associated with FLiBe.

Hastelloy-N is a metal alloy which was utilized as a structural material in the spallation target. Hastelloy-N is part of a family of Hastelloy alloys created by Haynes International. Hastelloy was used in the Molten Salt Reactor Experiment (MSRE) at Oak Ridge National Labs (ORNL) in the 1960's at an attempt to create a breeder reactor. The particular alloy which was used in the MSRE project was a modified Hastelloy-N which had a very short life span in the reactor due to high neutron fluxes which led to an increase of helium in the material due to alpha particles. (Vogelaar & Bowman, 2010) The actual corrosion resistance to molten salts at varying high temperatures was minimal between Hastelloy-N and modified Hastelloy-N. (Koger, 1972) In fact the corrosion rate of Hastelloy-N tested at 922K was less than 0.025 millimeters per year. Even under an oxidizing environment of UF_4, Hastelloy-N was much better than standard stainless steel or Inconel, which corroded at almost 0.45 millimeters per year.(Sohal, Ebner, Sabharwall, & Sharpe, 2010) ORNL did test the standard Hastelloy-N and found it to be compatible with a fuel salt up to 1200 K and high neutron fluxes. (McCoy, 1970) Therefore, Hastelloy-N for the time being is an ideal candidate for a neutron spallation source structure/containment vessel for GEM*STAR.

The key to GEM*STAR is the use of natural uranium as a spallation source for the subcritical core. Unlike previous designs which utilized lead and a liquid lead bismuth eutectic, the idea was to allow for an increased number of neutrons which could be used in the reactor chain reaction.

There are still alternatives to the aforementioned three primary materials. There was extensive testing done by ORNL in the late 1960's and early 1970's which tested Inconel and stainless steel as alternatives to Hastelloy. Additionally, the use of a carbon structure or supports would be adequately strong enough for a system using FLiBe and would allow the fast neutrons to be moderated to thermal energy levels. The use of metal coolants or liquid metal spallation sources have been tested extensively by PSI for the MEGAPIE project and could be an alternative to using FLiBe as a coolant due to the extensive knowledge database available. Finally, alternative solid targets such as solid lead or tungsten could be used. Liquid targets could also be used to provide additional spallation and have a secondary use as a coolant for a solid target structure.

Chapter 6: MCNPX Design Process

To begin the design process for the GEM*STAR target, the neutronics were the initial priority. Several neutronics assumptions were to be made in order to simplify the situation to allow enough time to do a coupled design with FLUENT to determine the feasibility of using solid uranium targets. In addition, there were several simulation constraints which were discussed in the MCNPX 2.6 Limitations section. The design basis began by utilizing a multiple plate design to potentially allow for cooling of the target. Since the planned beam power is assumed to be approximately 0.81 MW, a conservative assumption is that all the energy is turned directly into heat. 0.81 MW on a target which is 20 centimeters across and several centimeters thick would not allow for adequate cooling. Therefore, several plates were used at varying distances, followed by varying the thicknesses according to a natural logarithm then the Golden Ratio. Finally, a simulation utilizing a solid natural uranium cylinder was performed to refine a final design for FLUENT.

MCNPX Assumptions

The energy of the protons was assumed to be between 500 MeV and 1 GeV depending on the target material available which included tungsten, lead and uranium.(Vogelaar & Bowman, 2010) A proton energy of 600 MeV was chosen since it was a moderate number between the range and easily achievable for the purposes of GEM*STAR. A beam current of 1.35 mA was also assumed. (Vogelaar & Bowman, 2010) The window of the proton beam will be a Hastelloy-N because of anti-corrosion properties against molten salts. (Sohal, Ebner, Sabharwall, & Sharpe, 2010) The total beam power for GEM*STAR is 0.81 MW which is calculated in Appendix C: Important Analytical Calculations. The beam pattern is assumed to be a Gaussian density distribution in 2 axes, with the 3rd axis being the direction of the protons in the proton beam.

The target material which was tested in MCNPX was natural uranium. Natural uranium as chosen because of the ease of access and as an easy replacement material once a previous spallation target material was deemed unacceptable for service. The previous spallation target would then be melted down, fluorinated then mixed into the fuel salt of GEM*STAR as a recycling option. In addition, typical spallation sources do not use fissionable materials. Utilizing a fissionable material would significantly increase the number of neutrons being produced for utilization in the ADSR.

The material potentially cooling the target will be a molten salt, Lithium Fluoride-Beryllium Fluoride, FLiBe. The target material will be immersed in the FLiBe which acts as a coolant. Considering that GEM*STAR uses an enriched fuel-salt based on FLiBe and Uranium, utilizing unenriched fuel salt using FLiBe would be ideal for maintaining uniform manufacturing purposes. Figure 15 shows the neutron cross section of the molten salt for neutrons which is utilized for the spallation calculations in MCNPX. However, the data tables stop below 100 MeV as indicated in Figure 15 for FLiBe. To account for the missing data, built in MCNPX models are utilized. The accuracy of these models is debatable depending on the experimental situation. More experimental is required to determine the accuracy of the models for high energy particles.

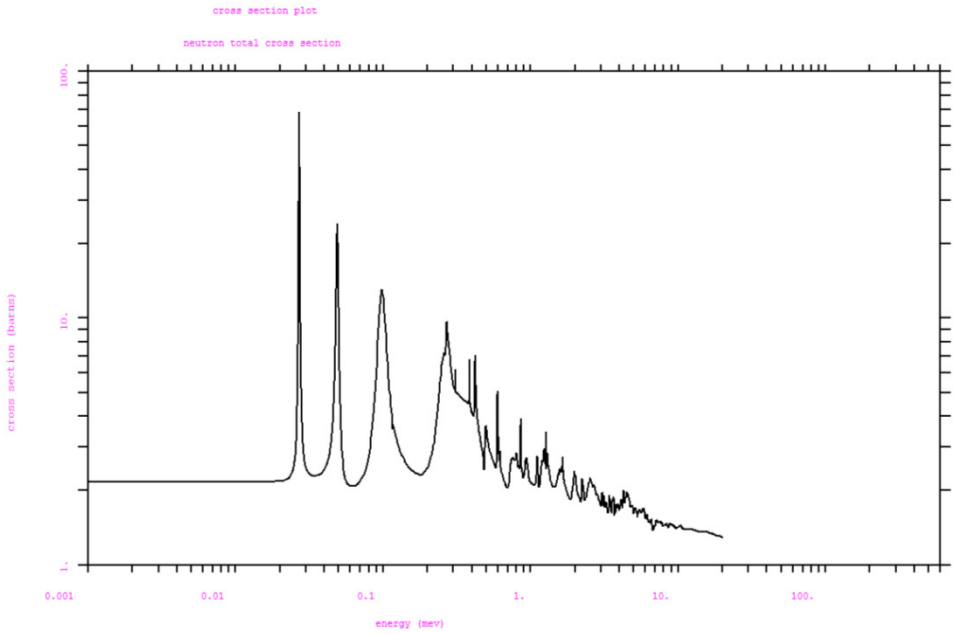

Figure 15: The cross section of molten salt, Lithium Fluoride-Beryllium Fluoride from 0.001 MeV to 600 MeV.

Figure 16 shows the energy deposition in FLiBe for 600 MeV protons at a 1.35 mA beam current. The initial proton source is at -1.5 centimeters and the energy deposition is summed every 2.5 mm and then plotted to produce the total energy deposition. The energy deposition begins almost immediately into the fluid but the energy deposition is limited to 8 kW per 2.5 mm cross-sectional slice. Although it appears to have a large energy deposition, the energy deposition is still less than natural uranium or Hastelloy-N. The peak energy deposition occurs about 7 centimeters after the Hastelloy window plate. To begin the design of the spallation source an arbitrary distance of 4.5 centimeters between plates and spallation material was created. The distance of 4.5 centimeters was chosen because the initial plate designs were assumed to be 0.5 centimeters thick. Factoring a distance of 5 centimeters between planes created a simple programming method for modifying distances and plate thicknesses inside MCNPX. In addition, there should be enough space to allow for cooling of the plate if significant heat was produced.

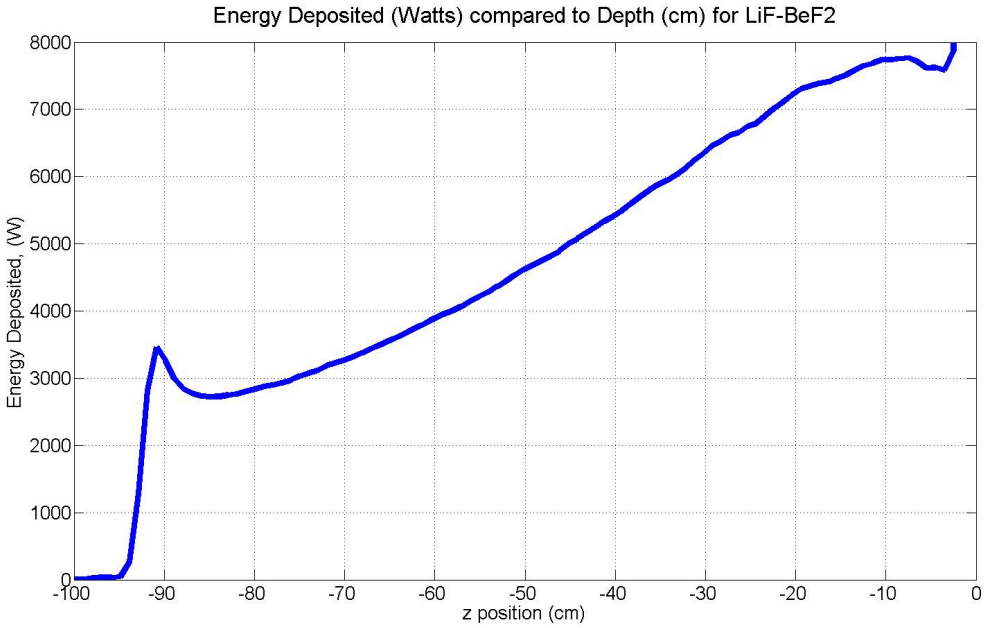

Figure 16: The total energy deposition in FLiBe with a 600 MeV proton beam at 1.35 mA beam current at -1.5 centimeters on the graph.

In addition to the FLiBe, the other material being utilized is Hastelloy-N. Similar to the FLiBe, Figure 17 shows the neutron cross section of the Hastelloy-N. The neutron cross section will be useful in determining the number of neutrons being produced from the structural materials. However the cross section is only useful in data format up until 100 MeV. After 100 MeV, models will be used for the 600 MeV proton simulations. There will be neutrons with energies higher than 100 MeV from the spallation source.

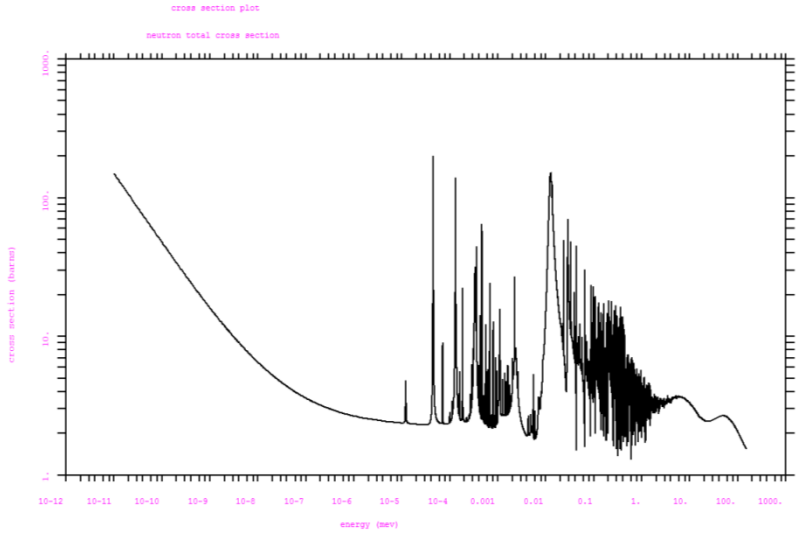

Figure 17: The neutron cross section of Hastelloy-N until approximately 100 MeV.

Figure 18 shows the energy deposition of 600 MeV protons in Hastelloy-N at 1.35 mA beam current. The properties of the Hastelloy-N were retrieved from datasheets from Haynes International. (Haynes International) Important data pulled from the data sheets can be found in Appendix B: Material Properties. Comparing Figure 16 and Figure 18, they appear to have similar shapes. However, the peak energy deposition for Hastelloy-N occurs at 2 centimeters at a peak of 10,000 watts compared to 10 centimeters at 7700 watts for FLiBe. Since the window in this case is Hastelloy-N in a Hastelloy-N based environment, the distance after the beam enters the world where the peak energy deposition occurs is 2 cm. In addition, all the proton energy is deposited within the first 25 centimeters of the Hastelloy-N while the FLiBe requires a distance of almost 100 centimeters to deposit all of the energy.

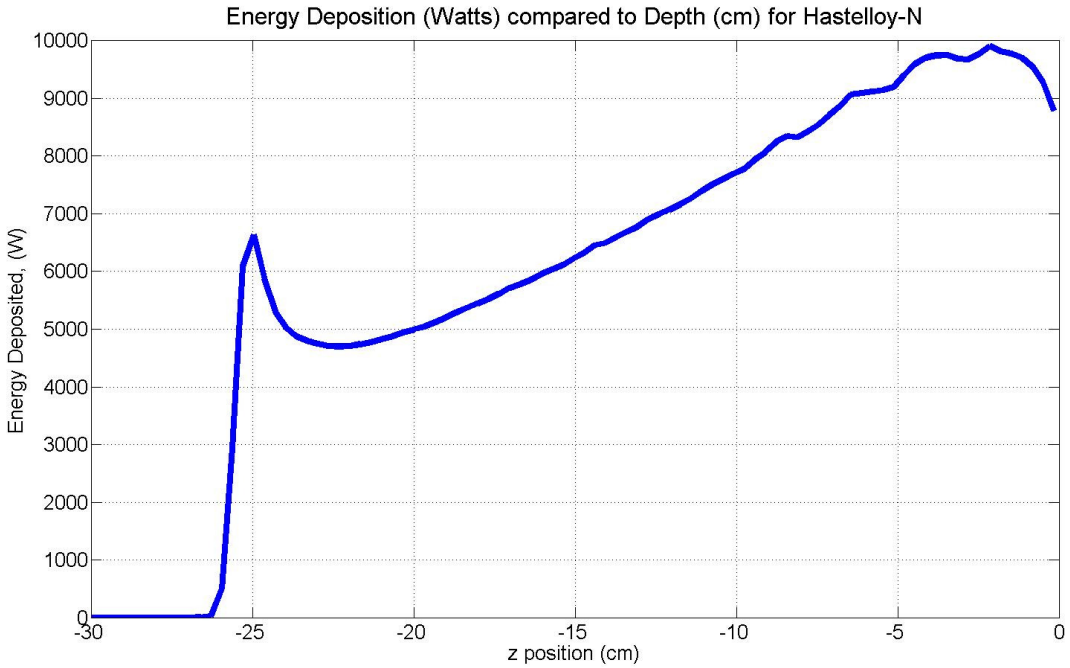

Figure 18: The total energy deposition in Hastelloy-N with 600 MeV proton beam at 1.35 mA beam current at -1.5 centimeters on the graph.

The energy deposition in FLiBe occurs at 10 centimeters into the material and the energy deposition for Hastelloy occurs at 2.5 cm. Once the protons and the spallation products have reduced in energy level, more energy may be deposited in the Hastelloy-N and the FLiBe. Therefore, flux and energy deposition tallies will be taken for the various designs tested. For initial design testing purposes, support structures using Hastelloy-N were ignored due to the lack of energy deposition by the high energy protons assuming that most structures would be less than 2 centimeters in thickness. In addition, fluid spaces should be kept less than 10 centimeters for the FLiBe.

The primary target structures for the testing will be constructed from natural uranium. Figure 19 shows the energy deposition in Watts in natural uranium using MCNPX. The total energy deposition for protons is about 50% more (15 kW) deposited compared to Hastelloy-N. The peak energy deposition occurs

almost immediately after the Hastelloy-N window. Therefore, a majority of the proton beam's energy is deposited in the uranium. However, the neutron fluxes and energy transfer will be addressed during the design process.

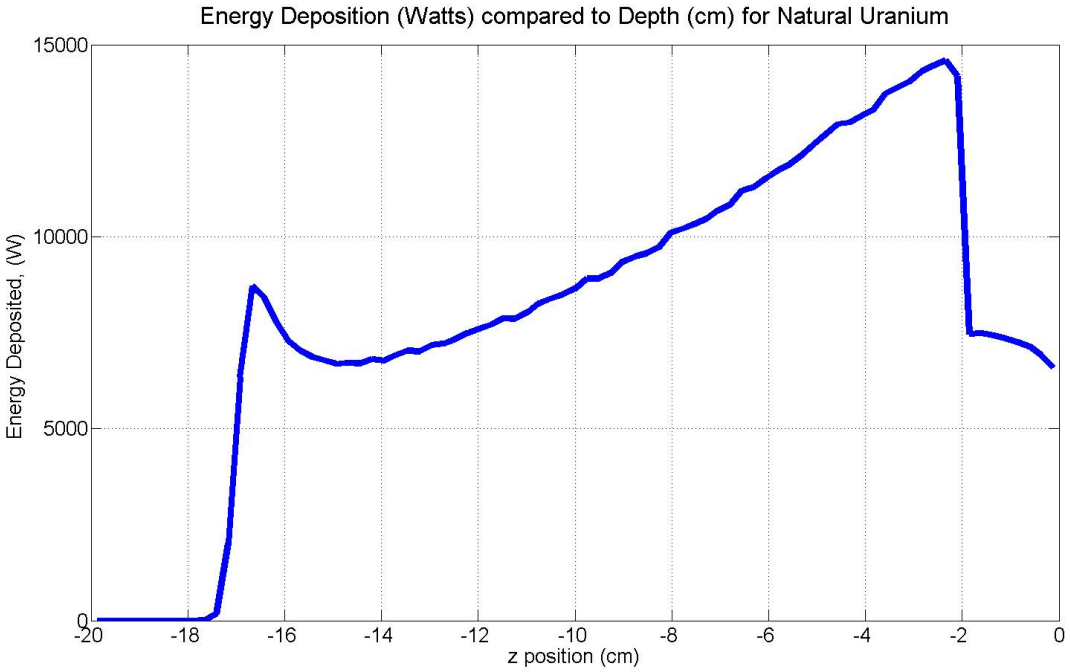

Figure 19: The total energy deposition in natural uranium with 600 MeV proton beam at 1.35 mA beam current at -1.5 centimeters on the graph.

Figure 20 shows the energy deposition comparison between all the materials for protons at 600 MeV with a 1.35 mA beam current which enters the window at -1.5 cm. By comparing all three graphs on one graph, the energy deposition differences are apparent for protons. FLiBe has the least amount of energy deposition while Hastelloy-N and natural uranium provides the highest amount of energy deposition. Uranium and Hastelloy have their peak energy deposition almost immediately after the beam window while the peak for FLiBe occurs at approximately -10 cm. By comparing the graphs, minimizing the use of Hastelloy will be necessary to avoid unnecessary energy deposition while the energy deposition in the FLiBe is a relatively minor concern.

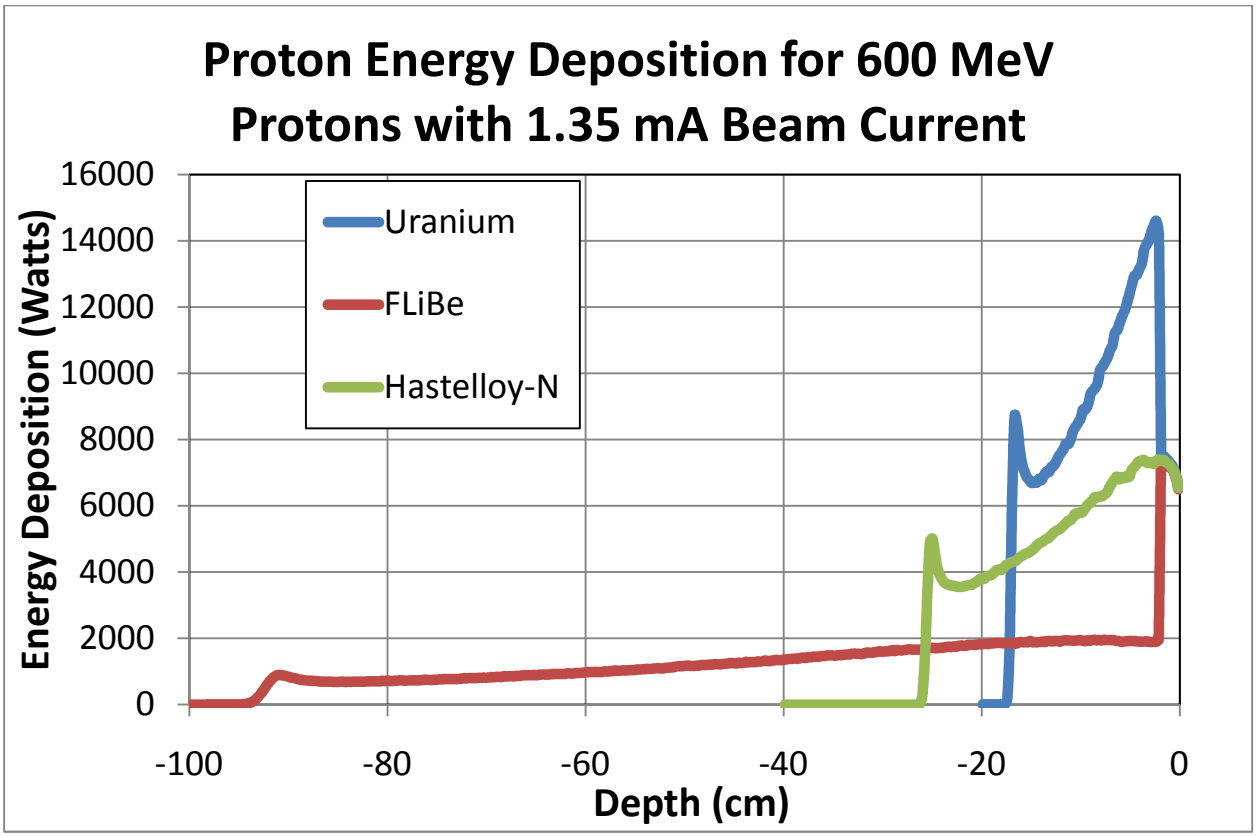

Figure 20: A comparison between the three major materials utilized in the spallation target design. The proton beam enters at -2 centimeters and continues downward as indicated by the Depth axis.

Simulation Constraints and Constants

There were design assumptions and constraints for testing each design variation of a spallation target. The plate and uranium cylinder diameters were 20 centimeters. The entire spallation structure was then surrounded by a Hastelloy target tube which was 28 centimeters in diameter and one meter long to ensure that all the neutron flux into the subcritical core could be tallied. The spallation target assembly was centered in the 1 meter long tube. The proton beam window had a set thickness of 0.5 centimeters which should allow little energy deposition in the plate based on Figure 18.

The proton beam used a Gaussian density beam distribution in one plane with 600 MeV protons incident on the beam window. In order to determine the amount of heat generated in each target, a mesh tally was created which overlays the spallation target. In addition energy deposition tallies were taken for each target structure and the proton beam accelerator window. The particles utilized for the energy deposition tallies were: neutrons, protons, photons, deuterons, tritons, helium-3, alpha particles and heavy ions. Sub-atomic particles and low mass particles were not considered because of the minimal impact they would have on heat deposition. Neutron fluxes were tallied for the target tube structure and the proton beam window. The neutron flux of the beam window was calculated to ensure minimal backscattering of each target design. Each test simulation used one million protons then the

data was extrapolated out to power levels which were calculated in MATLAB and transferred to Microsoft Excel.

Initial Plate Spallation Target Design

To start the design process, a plate target design method was a good starting point because it posed the least complex and easily modified design which was shown in the ADS Conference at Virginia Tech in September 2010 (Ferguson, 2010). The specific design utilized had several plates then a stopping block of uranium. Figure 21 shows a diagram of a sample target used for testing in MCNPX. In the figure, there were four uranium plates but each test simulation ran with varying numbers of plates from zero plates (only the cylinder) to five plates. Each plate had a set thickness of 0.5 centimeters to prevent melting from occurring. The stopping uranium cylinder was set at an arbitrary height of 15 centimeters.

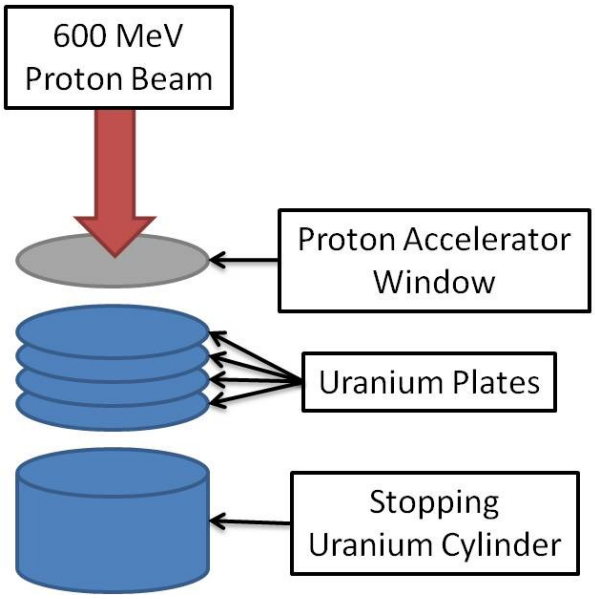

Figure 21: The sample plate design spallation target with a stopping uranium cylinder which stops the protons from going to the bottom of the reactor and irradiating the containment vessel. The proton beam enters through a Hastelloy proton accelerator window.

At this point in the design process, finding the features to maximize neutron flux radially into the potential reactor was the primary concern. Heat deposition was also noted and recorded using the special tallies available in MCNPX. The first test performed was to vary the number of plates in the spallation target structure and evaluate the neutron fluxes and energy deposition. The beam pattern distribution for these tests was a discrete beam density pattern which was modeled after the example in the MCNPX 2.6 Manual (LANL, 2008). There were six primary experiments performed which vary from no plates and the stopping cylinder up to five plates and a stopping cylinder. Total energy deposition and neutron flux tallies were taken for each experiment. Table 9 shows the neutron fluxes and counts radially from the target materials and the window flux.

Table 9: The various design iterations and the resultant neutron count/tallies in the radial direction and the backscatter through the beam window.

Design Iteration	Radial Direction		Window Backscatter		% of neutron window backscattering
	Count/Tally	Flux (neutrons/cm^2)	Count/Tally	Flux (neutrons/cm^2)	
0 plates, 1 cylinder	1.6698E+08	15632.76	1.5702E+07	49981.02	8.60%
1 plate, 1 cylinder	1.8169E+08	17009.92	1.0948E+07	34848.57	5.68%
2 plates, 1 cylinder	1.6488E+08	15436.16	8.0305E+06	25561.88	4.64%
3 plates, 1 cylinder	1.4990E+08	14033.72	6.3812E+06	20311.99	4.08%
4 plates, 1 cylinder	1.3592E+08	12724.91	5.4123E+06	17227.89	3.83%
5 plates, 1 cylinder	1.2456E+08	11661.38	4.8835E+06	15544.66	3.77%

The neutron counts were taken for one million protons incident on the window. The percent of neutrons backscattering was calculated from the count tallies rather than the flux. The flux for the window was much higher than the flux in the radial direction. The higher flux for the window was caused from the types of tallies performed in MCNPX. The radial direction tally was performed across a one meter long tube which surrounded the target. The larger surface area accounts for an apparent decrease in neutron flux even though the count is 10 to 100 times greater for the radial direction. Figure 22 shows the neutron tally along the major axes. The tally for the iteration with no plates and only the stopping cylinder, the neutron flux was slightly less compared to the design with 1 plate and the stopping cylinder. This was caused by the lack of extra material needed to allow for spallation to occur based on Figure 19. However, after the first cylinder, there was a linear decrease in the neutron flux tally. The height of 15 centimeters was maintained to allow for consistency between simulation variations.

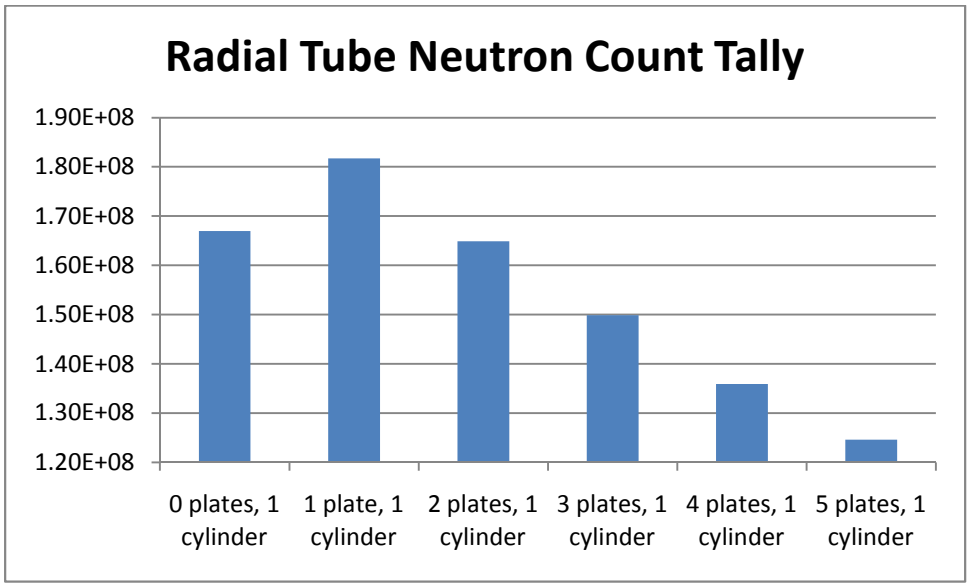

Figure 22: The tube/radial flux tallies for each design iteration using plates and a stopping cylinder for 1 million protons.

In addition, Figure 23 shows the percent of neutrons backscattering back into the proton beam window. The tally counts are shown for one million protons rather than the flux for reasons previously discussed. Based on the design iterations, there was a significant decrease of neutrons backscattering into the proton beam window as the number of plates increase. However, the results showed a decreasing logarithmic curve which levels out around the design iteration with 2 or 3 plates.

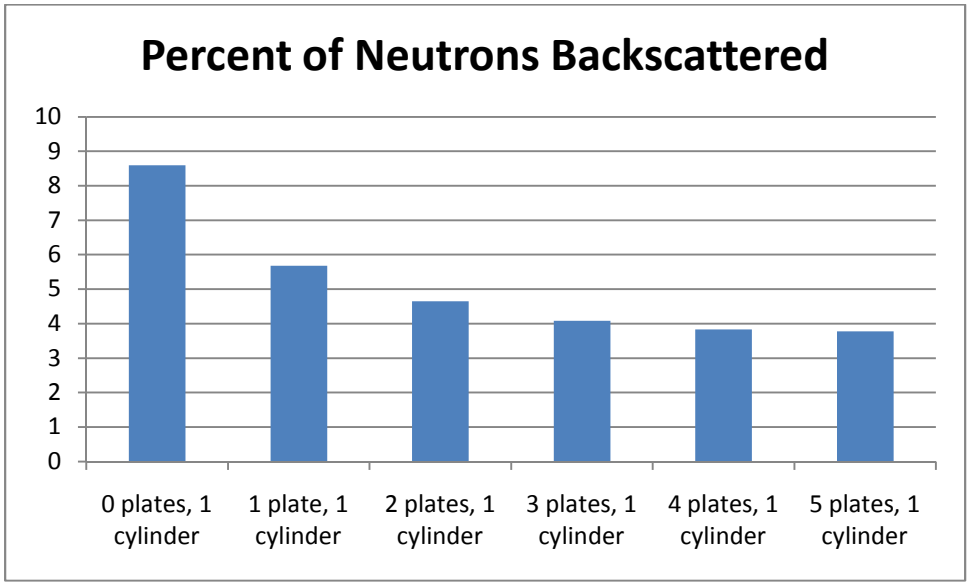

Figure 23: The percent of neutrons being backscattered back into the proton beam window using data from Table 9.

As stated earlier, at this stage of designing, maximizing neutron production was the primary goal while noting and recording energy deposition. Figure 24 shows the total energy deposition for all the target uranium materials and the proton beam window. There was a linear decrease in the total energy deposited in the target structures from zero plates through 5 plates.

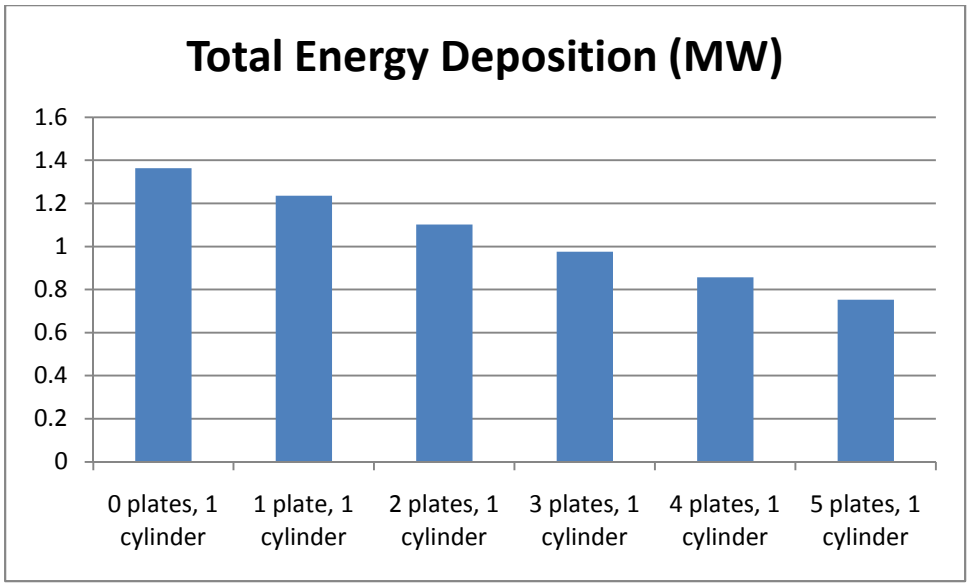

Figure 24: The total energy deposition in the target structures and proton beam window for each design iteration.

Since all the trends are linear, for the multiple plate designs of thickness 0.5 cm, the deciding factor for the next step in the design was the logarithmic decrease in the backscattering, since there were no appreciable changes in the other initial design considerations. Since the neutron percentage backscattered decreased until about 2 or 3 plates; the next design phase will only concern 2 and 3 plate designs. However, the amount of energy deposited in the FLiBe increased significantly with more plates as shown in Table 10. The FLiBe volume between the plates was increased with the number of plates which resulted in increase energy deposition in the coolant. Minimizing the amount of energy deposited in the FLiBe was ideal, so minimizing the number of plates by consequence minimizes the amount of energy deposited in the FLiBe.

Table 10: The energy deposited in the FLiBe and the percentage of energy deposited in the FLiBe over the entire structure and the fluid tested in MCNPX.

Design Iteration	MW deposited in FLiBe	percent energy deposited in FLiBe
0 plates, 1 cylinder	0.0872	6.01
1 plate, 1 cylinder	0.116	8.58
2 plates, 1 cylinder	0.153	12.19
3 plates, 1 cylinder	0.1885	16.20
4 plates, 1 cylinder	0.2211	20.53
5 plates, 1 cylinder	0.2509	24.99

The next designs used the 2 plate design buy varying the distances between the plates, window and stopping cylinder. Varying the distances could potentially increase or decrease the radial neutron flux and alter the backscattering properties.

Varying the Distance between the Target Structures in the 2 Plate Design

The intention behind varying the spacing between was to test the hypothesis that by increasing the spacing between two target structures the number of neutrons produced in the radial direction would increase due to more spacing and less chance of the target structures absorbing the spallated neutrons. Decreasing the spacing could have the opposite effect of reducing the number of neutrons produced in the radial direction. However, increasing the distance between the target structures could decrease the neutron backscatter as well and vice versa by decreasing the distance.

The experimental setup is the same for the Initial Plate Spallation Target Design considering the proton beam. Only the spacing between each plate was varied from 1.5 centimeters to 7.5 centimeters which seemed adequate for testing because the distance would reduce the chance of depositing significant amounts of energy into FLiBe based on Figure 18 but appeared to capture enough protons for spallation. For each design iteration, only the spacing between two structures changed while the distance between the remaining structures stays at 4.5 centimeters. A relatively significant change was an MCNPX error which appeared which concerned the cross section models of the Lithium used for analysis. There was a known issue with the photon libraries associated with lithium. So a switch was made to use elemental Lithium in the program simulations which utilize the models rather than the data tables. The increase in energy deposition was negligible and the trends were still maintained based on initial analysis.

The first design iteration was varying the distance between the proton beam window and the first plate between distances of 1.5 centimeters to 7.5 centimeters stepping at one centimeter intervals. Figure 25 shows the radial neutron flux for one million protons entering the target structures. Based on the graph, for every incoming proton there are approximately 150 to 175 neutrons which leave the target structure which would then enter the subcritical core. However, the trend predicted to have increasing neutron flux as the distance between the targets structures increased was incorrect for the first plate and proton beam window. As the distance between first plate and proton window decreased, the number of neutrons increased in the radial direction. Based on Figure 22, the values produced for the 4.5 centimeter spacing was approximately the same which provides some validation for the neutron counts.

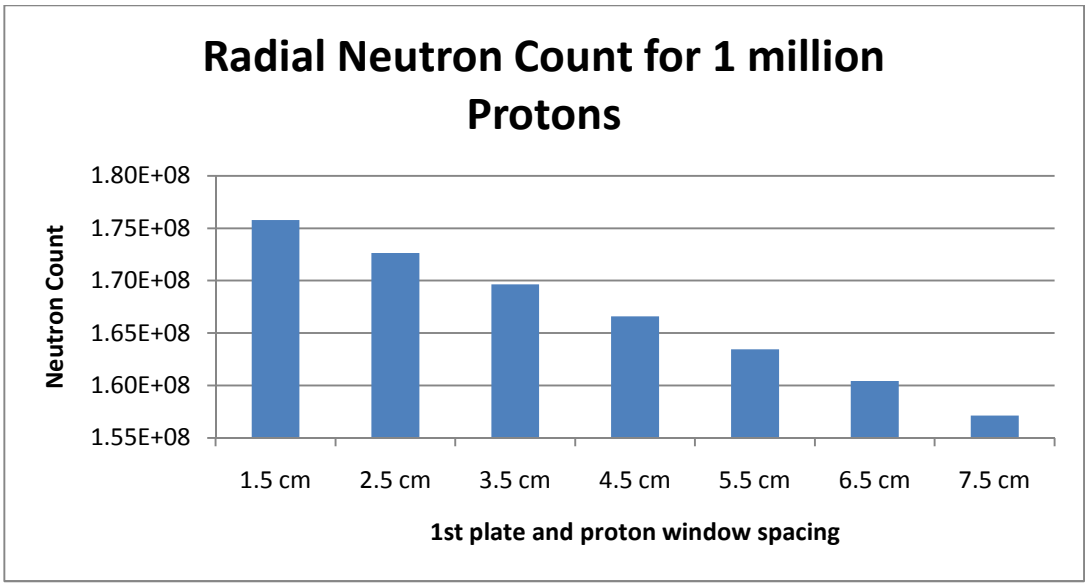

Figure 25: The radial neutron flux for the varying distances between the first plate and the proton beam window.

By contrast, the hypothesis for backscattering was confirmed where the number of neutrons backscattered increased as distance was decreased since there was less distance between the first plate and proton beam window. Figure 26 shows the associated trend between backscattering and the associated spacing. The less distance increased the number of reflections occurring which did not deposit in the FLiBe coolant.

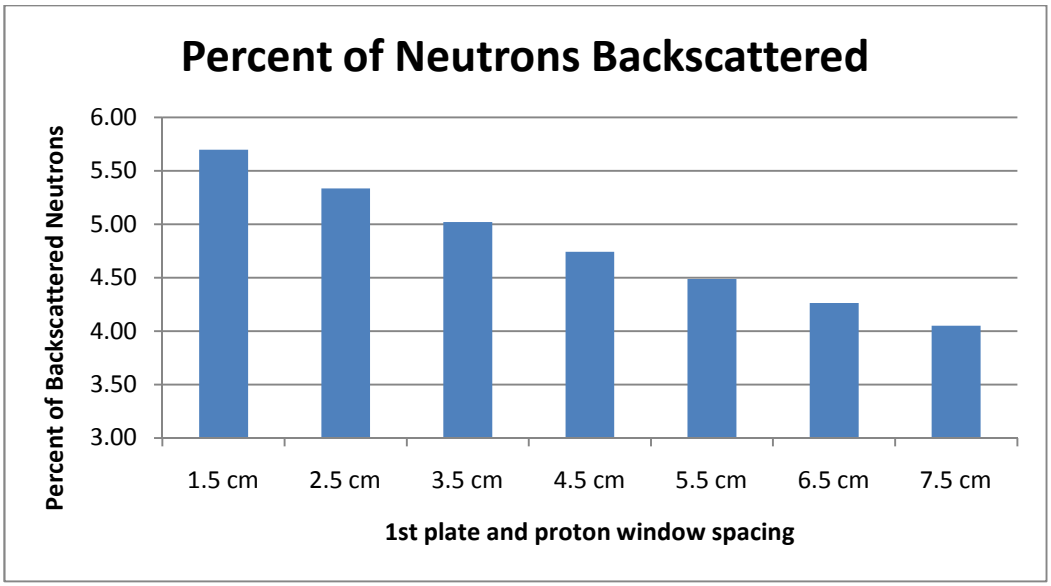

Figure 26: The percent of neutrons backscattered into the proton beam window compared to the 1st uranium plate and proton window spacing.

However, since the spacing between the first uranium plate and the proton beam window has a relatively small effect on the values produced in comparison to the initial multiple plate experimental design. The neutron backscatter varies between 4% and 5.7% while the neutron tube flux only varied approximately 11.4% with respect to the 1.5 centimeter spacing. There is no significant change between these designs, so there is no optimal positioning. For the next set of experiments, the first plate and the second target plate distances were varied while maintaining the distance between the first plate and the proton beam window of 4.5 centimeters.

Figure 27 shows the radial neutron counts for varying spacing between the first and second uranium target plates. Excluding the apparent outlier for 3.5 centimeter spacing, there is a linear trend similar to that of Figure 25.

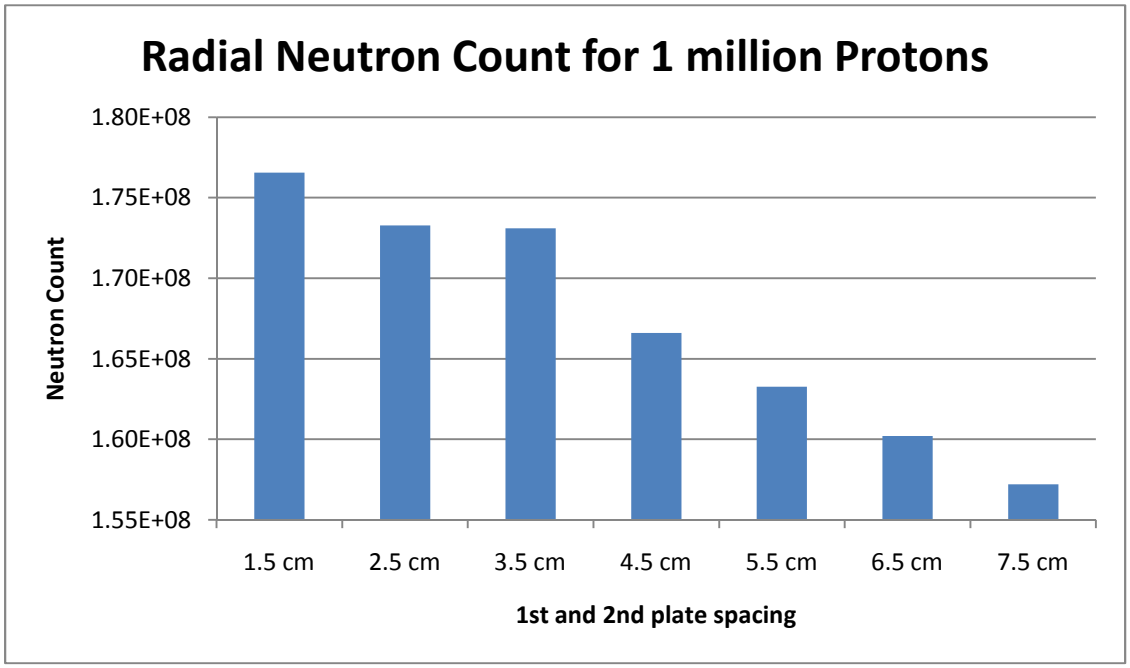

Figure 27: The radial neutron flux for the varying distances between the first uranium plate and second uranium plate.

The differences in neutron count between Figure 25 and Figure 27 data was relatively small. Table 11 shows the differences between the two neutron counts. Excluding the large percentage difference for the 3.5 centimeter spacing, the differences in radial neutron counts varied by less than half a percent in the worst case scenario. Based on these results, variable spacing had almost a non-existent effect on the radial neutron count.

Table 11: The percent differences between the 1st plate and proton beam window compared to the 1st plate and 2nd plate spacing with respect to the 1st plate and 2nd plate results.

spacing	1st plate and window	1st plate and 2nd plate	difference
7.5 cm	1.57E+08	1.57E+08	0.05%
6.5 cm	1.6E+08	1.6E+08	-0.14%
5.5 cm	1.63E+08	1.63E+08	-0.12%
4.5 cm	1.67E+08	1.67E+08	0.00%
3.5 cm	1.7E+08	1.73E+08	1.99%
2.5 cm	1.73E+08	1.73E+08	0.37%
1.5 cm	1.76E+08	1.77E+08	0.45%

Table 12 compares the neutron backscatter between the two test sets for varying spacing and the associated percentage difference with respect to the 1st plate and 2nd plate spacing. The percent of backscattering ranged from 4.2% up to 5.5% which was slightly different than the numbers produced from the spacing between the proton beam window and the first plate which ranges from 4% to 5.7%. There was an outlier at the spacing of 3.5 centimeters due to a simulation anomaly which was reproduced multiple times but was not explored further due to time constraints as well as the trend associated with the other spacing test simulations. As previously stated, MCNPX provided a guideline and determining the accuracy of the results requires variance reduction.

Table 12: Comparison of the percent of neutrons backscattered into the proton beam window for the 2 spacing designs, by find the percent difference with respect to the 1st plate and 2nd plate spacing.

	Percent Backscattered		
spacing	1st plate and window	1st plate and 2nd plate	difference
7.5 cm	4.051	4.190	3.31%
6.5 cm	4.263	4.355	2.11%
5.5 cm	4.486	4.532	1.02%
4.5 cm	4.741	4.741	0.00%
3.5 cm	5.021	5.266	4.65%
2.5 cm	5.336	5.221	-2.21%
1.5 cm	5.696	5.497	-3.62%

Since the number of neutrons backscattered did not vary compared to the first spacing iteration, and the spacing had no effect for the neutron counts between iterations, the decision was made to re-evaluate the testing methodology using natural functions such as the Golden Ratio and the natural logarithmic functions as a guide for plate thickness due to their prevalence in the natural world.

Golden Ratio and Logarithmic Plate Designs

Since the effect of spacing was minimal with constant thickness plates in FLiBe, the next major factor would have to be the amount of material utilized in each target structure. Varying the thickness of the target structure would allow for more spallation material and less opportunity for the energy to be deposited in the FLiBe coolant. To reduce the number of factors affecting the simulations, only the thickness of the plates was varied; the spacing between structures was maintained at 4.5 cm. There were four target structures utilized all with varying/increasing thickness the farther the distance from the proton beam window. Figure 28 shows a diagram of the general setup for both designs. Like the previous designs, there is a circular cross section for the target designs with a diameter of 20 centimeters.

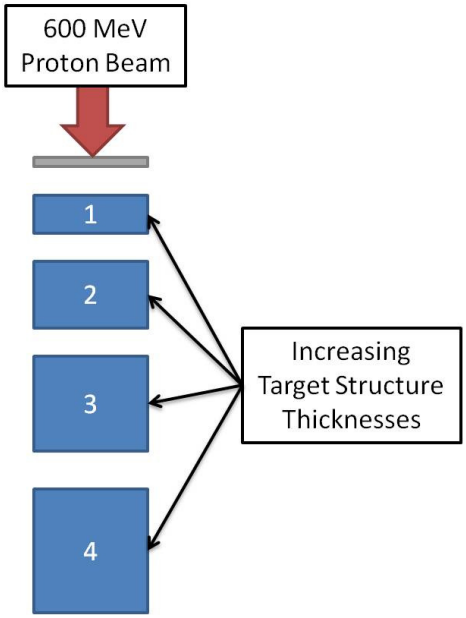

Figure 28: An example setup for the logarithmic and exponential designs which depicts the increasing thickness of the target material with increasing distance from the proton beam window.

In addition for this particular design, the beam pattern was altered from a discrete density setup to a continuous density function based on a Gaussian curve which was discovered in MCNPX. Although the change in beam design was intended to more closely mimic an actual proton beam, the change does not invalidate the findings of the previous trials. Based on testing the new beam design, the amount of energy deposited was significantly decreased and the neutron fluxes increased which are shown in the Logarithmic/Exponential Design section.

Logarithmic/Exponential Design

For the logarithmic design, the first uranium plate was maintained at 0.5 centimeters, as the initial size. Using a natural logarithm/exponential function, the remaining thicknesses were calculated rounding up to the nearest half centimeter. The thicknesses can be seen in Table 13 which was calculated using equation (28) as an estimation tool. The total target material thickness was summed up which indicated

there was enough uranium to ensure all the energy is deposited in the structures excluding the energy deposited in the FLiBe.

(28) $$T = 0.5\, e^{n-1}$$

Where *T* is the thickness in centimeters, *n* is the target structure number and 0.5 is the initial thickness of the first target structure.

Table 13: Thicknesses for the logarithmic/exponential design which was determined from an exponential function with the initial value of 0.5 centimeters thick.

exponential	
target number	thickness (cm)
1	0.5
2	1.5
3	3.5
4	10
total	15.5

The resultant neutron fluxes are shown in Table 14. The neutron flux out of the bottom of the target structure was considered for this design iteration to ensure that a majority of the neutrons were exiting radially following the drastic change in design. The significant change in beam patterns as mentioned earlier did have a relatively drastic effect in some design features. The Gaussian beam pattern led to an increase in the radial neutron flux of about 19%, a decrease in the window flux of about 31% and a decrease in the percent of neutrons backscattered into the proton beam window of about 72%. However, there was a significant increase in the neutron flux leaving the bottom of the target structures by a factor of about 82.5%. However, the amount of neutrons leaving the bottom of the target structures is still 1/10th of the radial neutrons.

Table 14: Compares the old discrete beam design to the new continuous Gaussian beam pattern as well as the good and bad features depicted in the green and red highlighted boxes compared to the Gaussian Beam pattern

Neutron Count for 1 million Protons			
Beam Pattern	Discrete Density Pattern (Old)	Gaussian Pattern (New)	Percent Difference
radial	1.53E+08	1.89E+08	19.20%
window	7.00E+06	5.35E+06	-30.98%
bottom	3.40E+06	1.93E+07	82.43%
percent backscattered	4.29%	2.50%	-71.58%

Therefore, the change in beam pattern did have a significant effect on the neutronics of the simulations. But since the final beam pattern has yet to be determined, for the final design and analysis, a continuous Gaussian beam was utilized to simplify programming and provide an ideal case. Table 15 shows the energy deposition comparison between the old beam pattern and the new Gaussian beam pattern. With the new pattern the good results show that the heat deposited in the structure is significantly less for the proton beam window and first two uranium target structures. However, there was a significant increase in energy deposition in the third target structure; approximately nine times the amount of heat was deposited in the third structure compared to the old beam. In addition, 1.2 times the amount of heat was deposited in the fourth and largest target structure which was intended to stop the remaining protons which did not cause spallation. The amount of energy deposited in the FLiBe was decreased by a factor of 0.15 which indicates more protons and spallated neutrons are depositing their energy in the target structures rather than the coolant. Finally, the total heat deposited was increased by a factor of 1.34. The total increased heat could potentially require additional cooling when the next design phase utilizing FLUENT was started.

Table 15: Target structure energy deposition in megawatts and the differences in values between the discrete density pattern and the continuous Gaussian pattern with the associated percent differences with respect to the new pattern.

Exponential Design Energy Deposition in Megawatts				
Beam Pattern		Discrete Density Pattern (Old)	Gaussian Pattern (New)	Ratio (New/Old)
window		0.0139	2.07E-04	0.01
Target Structure	1	0.0434	0.0051	0.12
	2	0.0464	0.0234	0.50
	3	0.0419	0.3808	9.09
	4	0.685	0.831	1.21
FLiBe		0.2601	0.2223	0.85
Total		1.0907	1.4628	1.34

The results of utilizing a new target design while altering the beam pattern was a complex analysis but considering the time constraints required by MCNPX and the processing capabilities available, it was a necessary requirement during the design process. By utilizing the old beam pattern and comparing the neutron count results, there was no significant advantage for a thickness exponential varying target design. The multi-plate design had a flux of approximately 1.67×10^8 neutrons compared to a radial neutron count of 1.53×10^8 neutrons which was a decrease of about 9%. However, compared to the 2 plate design at 4.5 centimeters spacing, the total heat energy deposited was 1.167 MW compared to 1.09 MW which is a decrease and potentially alleviated cooling issues. However, the new beam completely negated the decreased cooling issues in the third target structure and the overall heat deposition which increased to 1.46 MW

By factoring in the new Gaussian beam, various aspects of the heat and neutronics were altered for better and/or worse. Therefore, the next step was to move forward to test the Golden Ratio thickness variations.

Golden Ratio Design

The golden ratio has been used to describe many features in the natural world. The ratio is approximately 1.618 and has only one solution which can be expressed in equation (29) as an irrational number.

(29) $$Golden\ Ratio = \frac{1+\sqrt{5}}{2} \approx 1.618\ldots$$

To keep within the boundaries of the particular simulations performed, the thickness of each target structure is multiplied by the previous. The total target thickness was deemed to 15 centimeters or greater. Table 16 shows the resulting thicknesses based on the design constraint of a total target thickness of 15 centimeters or greater. Each target thickness was multiplied by the golden ratio to obtain the thickness of the following target structure. Beginning with a two centimeter thick initial target structure allowed for the total target material to be greater than 18 centimeters which would ensure minimal protons escaped the target structure without causing spallation.

Table 16: The target structure and their associated thicknesses to maintain the Golden Ratio concept.

Golden Ratio	
target number	thickness (cm)
1	2
2	3.2
3	5.12
4	8.192
total	18.512

Since the effects between the old beam and the new proton beam design were determined, the new beam design was utilized for the Golden Ratio design as well as the subsequent designs until the final data analysis. Table 17 shows the comparison of the neutronics between the exponential design and the Golden Ratio design. With the golden ratio design there were positive gains compared to the exponential design. The proton beam window backscatter had a decrease by about 27%, the neutrons leaving the bottom decreased by 12% and comparing the backscatter percentages, there was a decrease of approximately 21%. However, there was a 4.5% decrease in the radial neutrons, but considering the significant drops in backscatter and bottom neutrons, this design is better than the exponential design in terms of neutronics. The decrease in the neutrons leaving the bottom of the target was due to the difference of total uranium mass between the exponential and Golden Ratio design. The Golden Ratio design had about three centimeters of additional uranium in thickness.

Table 17: The neutronics results and compares the exponential design and the golden ratio designs.

Neutron Count for 1 million Protons			
Design Comparison	Exponential Design	Golden Ratio	Percent Difference
radial	1.89E+08	1.81E+08	-4.50%
window	5.35E+06	4.19E+06	-27.58%
bottom	1.93E+07	1.73E+07	-11.83%
percent backscattered	2.50%	2.07%	-20.81%

In addition to the associated neutronics, the heat deposition was critical in determining physical feasibility. The heat energy deposition determined for the Golden Ratio design was deemed unacceptable as shown in Table 18. By comparison between the Exponential Design and the Golden Ratio Design, the Exponential Design had the advantage in terms of minimizing heat generation. The Golden Ratio only had the advantage in two of the target structures, the proton beam window and the fourth target structure. The rest of the structures generate more heat by a factor greater than one or two. However, despite these numbers, cooling could still be possible for the initial three target structures due to their relatively thin nature. A disadvantage of the Golden Ratio Design was more energy deposited in the FLiBe. Overall the total energy deposited was approximately the same between the two designs.

Table 18: Compares the energy deposition in megawatts between the Exponential Design and the Golden Ratio design for the Gaussian proton beam pattern and the associated comparison ratios.

Heat Energy Deposition in Megawatts				
Design comparison		Exponential Design	Golden Ratio	Ratio (Golden Ratio/Exponential)
window		2.07E-04	1.63E-04	0.79
Target Structure	1	0.0051	0.0149	2.92
	2	0.0234	0.0443	1.89
	3	0.3808	0.569	1.49
	4	0.831	0.5972	0.72
FLiBe		0.2223	0.2304	1.04
Total		1.4628	1.4560	1.00

Since there was no distinct advantage utilizing natural functions of the logarithmic exponential and golden ratio designs, a back step was taken by using a long natural uranium cylinder which determined the overall energy deposition.

Solid Uranium Cylinder Target

In order to fully understand the effect the proton beam had on the system with the new Gaussian beam and to understand the various other interactions occurring, the initial design starting point was broken down into its basic form. A reevaluation of the priorities of the target was necessary, heat generation and energy deposition became critical with neutronics becoming a secondary concern despite its importance. The amount of heat being deposited from a proton beam in a spallation target 20 centimeters in diameter and approximately 30 to 50 centimeters tall is 0.8 MW. If all the energy was converted into heat, removing the heat generated using FLiBe at 750 K became a difficult engineering challenge. Based on the initial design testing, there was fission heat being generated in the targets based on the MCNPX simulations which increases the energy deposition to 1 MW or greater. Therefore, to understand the energy deposition more completely, a single uranium cylinder which was 30 centimeters tall and 20 centimeters diameter was simulated under the same 600 MeV and Gaussian distribution proton beam.

Table 19 shows the heat energy deposition in the simple uranium cylinder design, compared to the previous designs, the total energy deposition was almost 2 MW of heat energy, which was about 25% to 50% more than the previous designs. The energy deposition of the window was approximately the same, and the energy deposition is approximately half of the multiple structure designs.

Table 19: Target structure energy deposition in megawatts for the associated important structures, such as the proton beam window, uranium cylinder and FLiBe coolant.

		Heat Energy Deposited (MW)
Structure	window	2.31E-04
	cylinder	1.831
	FLiBe	0.1211
	Total	1.9523

Table 20 shows the neutron counts for the uranium cylinder. There was a 1% increase in the backscatter compared to the multi-structure designs. However, there was an increase in the radial neutron fluxes by a factor of two on average. Despite the higher neutron counts, such a large structure would prove impossible to cool properly without cooling channels which would affect the neutron fluxes and potentially the structure of the target itself and physical limit of the structure as a neutron spallation source.

Table 20: Neutron counts for 1 million protons at an energy of 600 MeV, in the radial direction, the window backscatter and the neutron flux out the bottom of the structure.

		Neutron Count
Neutron Directions	radial	2.21E+08
	window	6.78E+06
	bottom	1.57E+07

backscattered	2.78%

Since the neutron counts and fluxes were maximized for a uranium cylinder, the attention turned towards the heat generated in the structure. Figure 29 shows a cross section of the heat generated in the uranium cylinder in the middle of the structure. The peak energy deposition was approximately 25 watts per 0.0156 cm^3 which returns a peak volumetric heat generation of 1600 watts/cm^3. However, the average energy deposition across the cylinder itself was 194.3 watts/cm^3. The extreme energy densities required much thinner spallation target structures to prevent melting. Even if the center of the structure melts and the exterior remains solid, there could be unforeseen issues such as increased pressure inside the spallation structure. Therefore, keeping the entire structure either solid or purely a liquid was necessary for safety reasons, not including super-criticality issues associated with uranium and excess fissions.

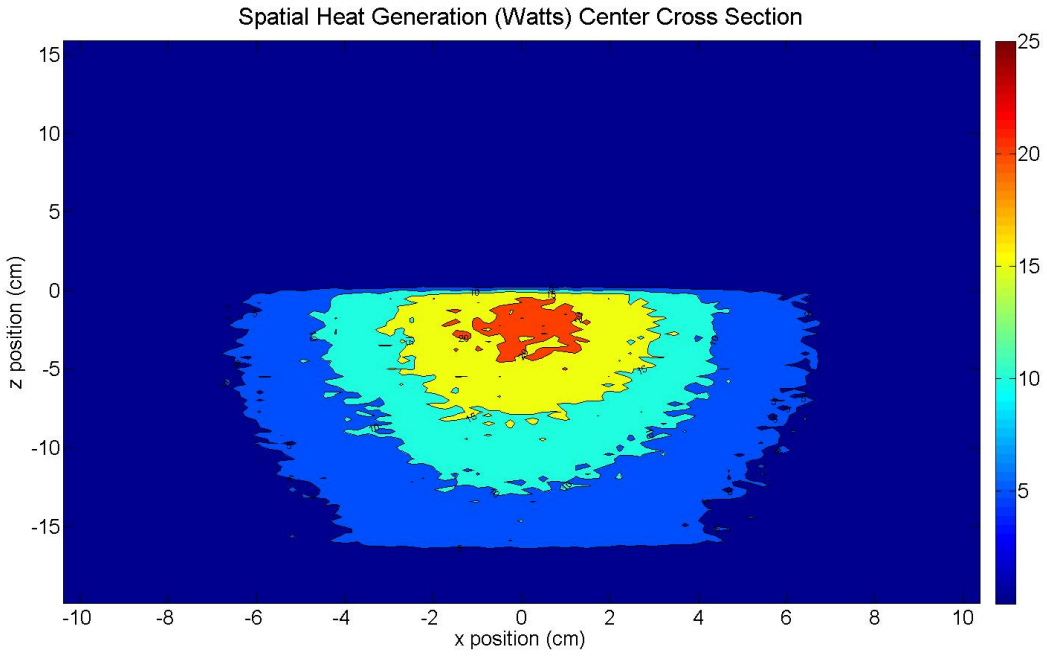

Figure 29: A cross section contour graph of the energy deposition/heat generation inside the solid uranium cylinder target. The proton beam begins at 15.5 centimeters on the z axis directed in the negative z direction. The heat generated includes all particles mentioned in Simulation Constraints and Constants.

The heat energy deposition peak correlated to neutron spallation based on the Bragg peak in a material. Figure 30 shows the energy deposition peak approximately 10 centimeters into the uranium cylinder. This peak continued to die off for the next 15 centimeters or so and then dropped off completely after a slight spike. Utilizing this graph gave a qualitative adjustment towards making a new design which will be discussed in the Chapter 7: Coupled MCNPX and FLUENT Design Process. Since the primary purpose of this research was to avoid melting of the structure, neutronics was a secondary goal as mentioned earlier. So the multiple target design was necessary for cooling purposes. However, determining the

amount of energy deposited in the FLiBe was a complex endeavor and was only generalized due to the fission heat generated and calculated based on qualitative results. The next design will utilize almost a "Sandwich" target structure to maximize the neutrons and allow for heat to be removed effectively.

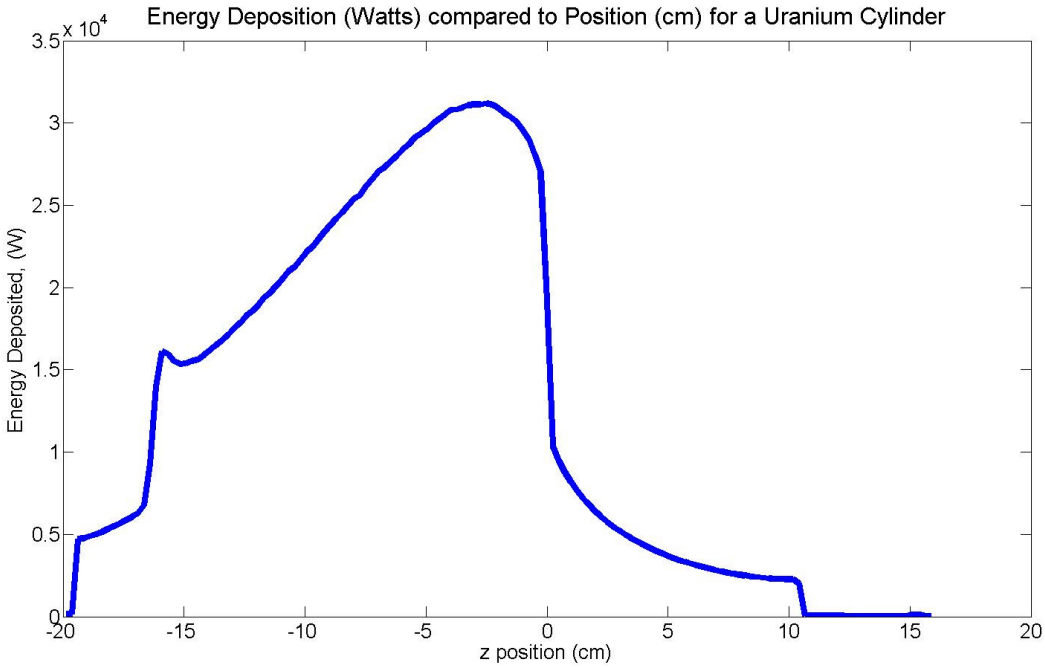

Figure 30: The peak energy deposition occurring in the uranium target cylinder. The peak energy deposition occurs from about 10 centimeters into the structure to about 15 cm.

Heat Implications of a Natural Uranium Spallation Target

Even though the beam energy utilized from the GEM*STAR accelerator was only 0.81 MW of beam power, the actual energy deposited in the structures can produce upwards of 2 MW of thermal energy due to fissions induced by the high energy protons. The increased heat posed a greater challenge to cooling the resultant design especially in the Sandwich Target Design section. However, the heat does vary based on the design, but an assumption for the target designs was at least 1.0 MW of thermal energy produced.

Chapter 7: Coupled MCNPX and FLUENT Design Process

Unlike the previous sections which only considered the MCNPX design iterations, this section used a design process which went back and forth between MCNPX and FLUENT. Any changes required for thermohydraulic purposes to prevent melting, would require changes in MCNPX and then retested in FLUENT. Using FLUENT required several assumptions which will be discussed in FLUENT Assumptions and Constraints. The central design utilized for the engineering process was the Sandwich Target Design. The "Sandwich" design uses a slowing down section which does not deposit a significant amount of energy, but allowed the proton energy to drop to a level where a majority of the energy was deposited in the primary target area. After the primary target area, there were stopping cylinder(s) to prevent the protons and a significant amount of neutrons striking the bottom of the target structure or bottom of the reactor vessel.

FLUENT Assumptions and Constraints

There were several general assumptions which were utilized for the FLUENT simulations. The target structure is assumed to have no heat flux entering or leaving the structure. The inlet temp of the FLiBe is 750 K considering the melting temperature of the FLiBe is approximately 732 K. Preliminary design simulations using simple flow channels utilized an inlet temperature of 800 K. However, a bigger temperature difference between the target structures and FLiBe would allow for a greater heat transfer which would then decrease the maximum temperatures in the target structures. In addition, all the FLUENT simulations were performed only for steady state results. The primary variation was only the flow rates through the structures of each design. Transient simulations are future areas of research.

For the initial set of simulations, the support structure was common steel in FLUENT. Figure 31 shows a CAD design of a support ring and the associated target structures. The support plates act as both a support structure for the plates and to direct the flow of FLiBe around the plates. The heat generation results from MCNPX indicate that a majority of the heat was deposited within a radius of four centimeters of the target plates. Therefore, a support ring could support the plates and cylinders approximately one centimeter inward from the outer edge of each circular target structure. For the multiple plate and cylinder arrangements, the flow openings were alternated at 180 to allow for cooling on either side of each target structure. The flow continued downward in an S-shaped pattern.

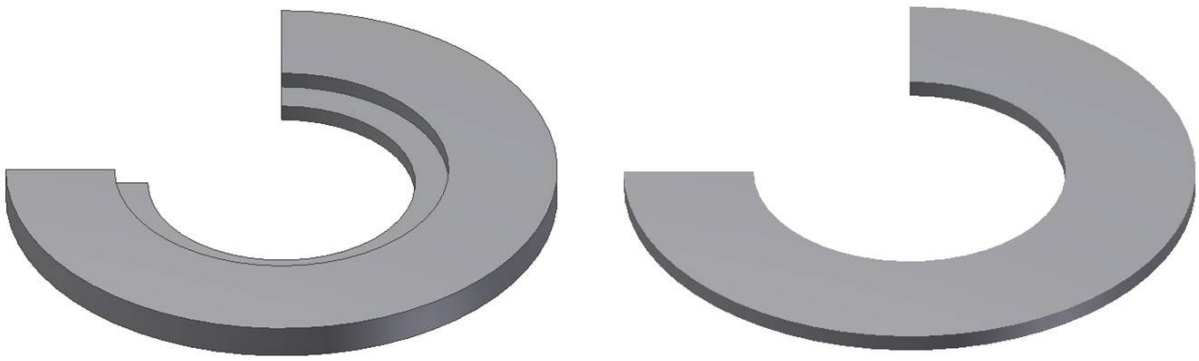

Figure 31: The support plates for the uranium targets were designed in Autodesk Inventor. The right support ring is used by designs which support the target plates using a machined groove. The left support ring is for target structures which sit in the machined lip area.

The maximum temperature was of the greatest concern due to the melting point of natural uranium at 1450 K. If the maximum temperature exceeded that temperature, the design would become invalidated. In addition, a buffer of 200 K to 300 K was created to prevent structural issues which may come from the natural uranium plates becoming soft under high temperatures. Additionally, Hastelloy-N is rated up for continuous usage in molten salts at 1200 K, so a maximum temperature of 1200 K was created as a design criterion. In addition, embrittlement and various other structural aspects of the uranium may come into play under long term usage in GEM*STAR.

Sandwich Target Design

There were four primary target design iterations utilizing FLUENT and MCNPX in alternating fashion. Several key factors were taken into consideration such as neutron counts and directions, proton counts and directions, heat deposited in various target structures and fluid velocities and heat transfer coefficients. Any thermohydraulic design changes between iterations automatically created a necessity to retest the neutronics and improve on the situation as the iterations increased. The four primary iterations are as follows which begins with the “Sandwich” design.

The First Iteration

The first iteration of the design was relatively simple in concept. The first design used three primary target plates, one centimeter in thickness and 20 centimeters in diameter where the Bragg peak would occur. In order to induce the Bragg peak to occur in those three primary target plates, a large cylinder of uranium would be used to essentially “slow down” the protons to an acceptable energy level where they would deposit their energy and cause spallation neutrons in the three primary target plates which correspond to the primary energy deposition. To account for the remaining protons which go beyond those plates, a stopping cylinder was used which was 15 centimeters thick. Figure 32 shows a simple diagram of the “Sandwich” design for testing. MCNPX simulations were performed without supporting structures except the containment tube and proton beam window. The results from the tallies

performed allowed for the calculation of heat generation in watts for each target structure as well as the associated support structures.

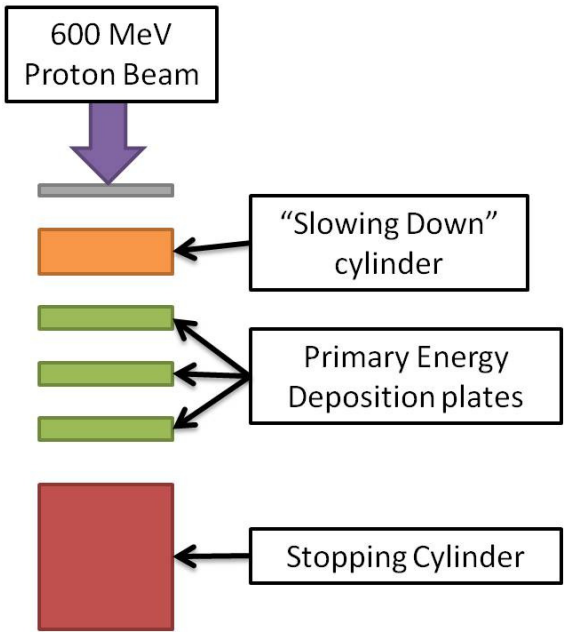

Figure 32: A simple setup of the Sandwich target design. The design uses a Slowing Down cylinder to induce the Bragg peak and peak energy deposition in the Primary Energy Deposition plates. The plates are then followed by a stopping cylinder to contain the remaining protons and associated fission products.

Two sub-iterations were performed to determine the optimal thickness of the Slowing Down cylinder to maximize the energy deposition in the middle three plates. The majority of the energy deposition should occur at the first plate to maximize the cooling available due to its proximity to the flow inlet. Any remaining energy deposition will occur in the stopping cylinder. The first sub-iteration utilized a five centimeter thick Slowing Down cylinder. Figure 33 shows a contour plot of the first iteration which allows for a qualitative judgment for the second iteration. The energy deposition was calculated as previously discussed, using a Cartesian mesh and summing the energy deposition per horizontal "slice" based on the mesh scaling. The first sub-iteration indicates minimal heat deposition in the first plate and a significant amount of heat deposition in the stopping cylinder which cannot be cooled easily due to its relatively large mass.

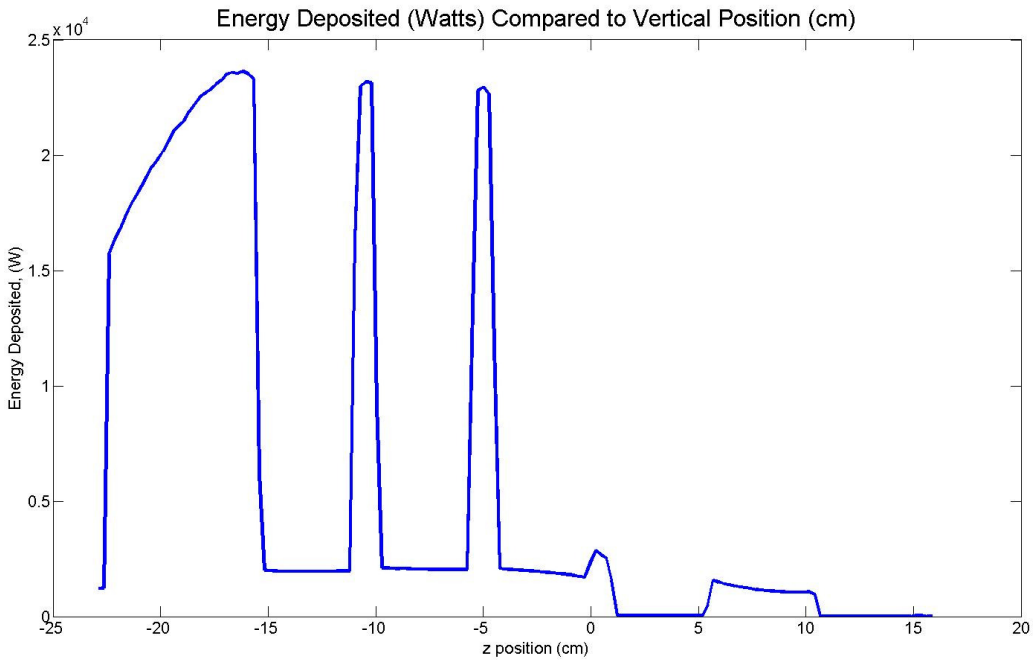

Figure 33: The energy deposition of the first sub-iteration to determine the size of the Slowing Down cylinder to maximize energy deposition in the primary target plates and reduce heat being deposited in the final target to prevent melting.

Based on Figure 33, a second sub-iteration was applied increasing the Slowing Down cylinder's thickness to seven centimeters as a rough judgment due to the minimal amount of energy deposited in the first one centimeter thick primary target plate and accounting for the volume of FLiBe between the Slowing Down cylinder and first primary target plate. Figure 34 shows the energy deposition with a seven centimeter thick Slowing Down cylinder. Using a Slowing Down cylinder with a thickness of seven centimeters allowed for the maximum energy deposition to occur in the three primary target plates. The middle plate receives the most energy deposition, but the energy deposition appeared to be relatively flat across the three plates. The stopping cylinder had a significant amount of energy deposition despite having a majority of the energy being deposited in the three plates.

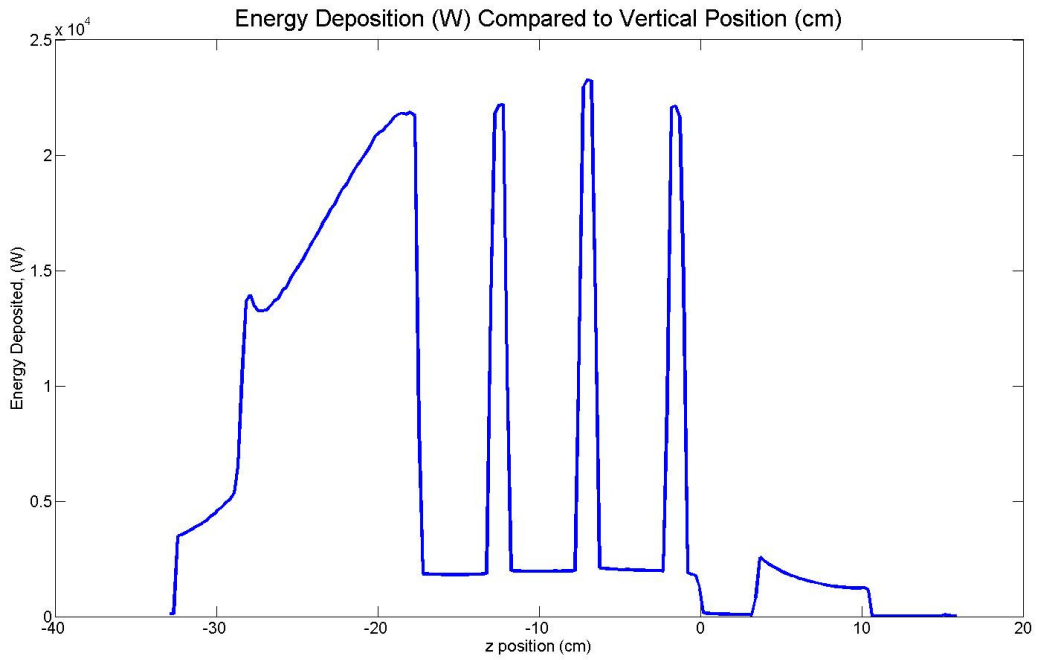

Figure 34: The energy deposition using a 7 centimeters Slowing Down cylinder, 3 primary target plates and a 15 centimeters stopping cylinder. The peak energy is deposited in the primary target plates while the remaining energy is deposited in the stopping cylinder.

The average energy deposition was determined using a F2 tally in MCNPX for each target structure. The peak energy deposition was used in the next iterations to refine the models for a final design. Table 21 shows several key neutron results. The neutronics and the heat generated were the two primary results which drove the design process. For the first design 92.37% of the neutrons were produced radially, while the remaining 7.63% either went back up the beam source or through the bottom of the stopping cylinder. The proton tallies were not taken for the first iteration because they were not a concern and energy deposition usually indicated when the protons would cease depositing energy and stop forward/downward motion.

Table 21: The neutron counts for 1,000,000 protons entering the window as well as the percentage of neutrons leaving the spallation source. The tallies were taken radially at the tube, the proton beam window and the bottom of the target structure.

	count	percent
radial	1.6410E+08	92.37%
window	2.8464E+06	1.60%
bottom	1.0709E+07	6.03%
total	1.7766E+08	

Figure 35 shows the flow setup for the first iteration. The design depicts an alternating cross flow pattern across and around the large target structures. The support rings act as flow channel walls and

the thickness was designed to take into account the weight of each target structure. Each plate weighed approximately 13 pounds while the slowing down cylinder would weigh 90 pounds while the stopping cylinder would weigh almost 200 pounds. There were no major structural calculations which were taken into account because flow velocities and body forces would change the design and cause an excess of design considerations which would be beyond this feasibility study.

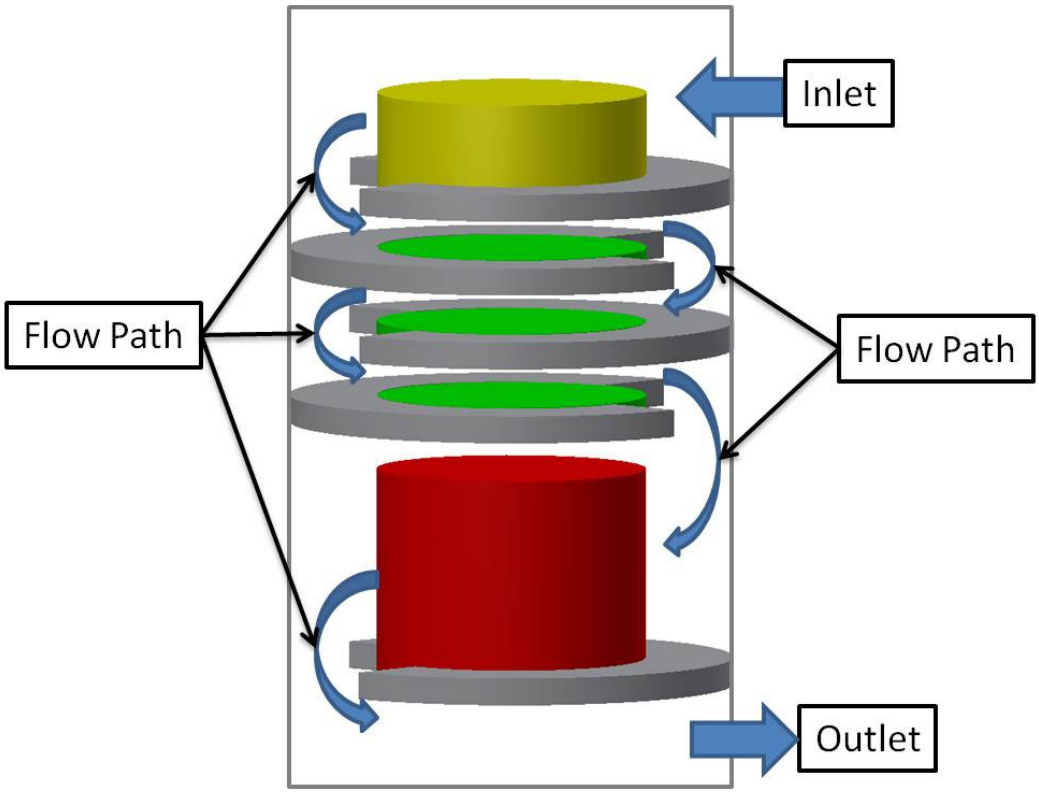

Figure 35: The design utilized for channeling flow around the target structures which were input into FLUENT.

Figure 36 shows a contour plot of the vertical cross section of the target structure. The flow rate at the inlet of the test structure is 10.2 gal/sec with an inlet velocity of 10 m/s. Due to the significant amount of energy deposited in the stopping cylinder, the ability to cool the stopping cylinder was inadequate to prevent melting in the center of each target structure. FLUENT capped the temperature at 5000 K for steady state operation. Note the scale depicts a maximum temperature of 5000 K for the stopping cylinder which indicates melting will occur considering the melting point of natural Uranium is 1450 K. The heat generated for each target structure is the average energy deposition determined from MCNPX. In addition for the target plates and stopping cylinder, the peak temperatures are located at the contact points of the supporting rings and the plates/cylinders.

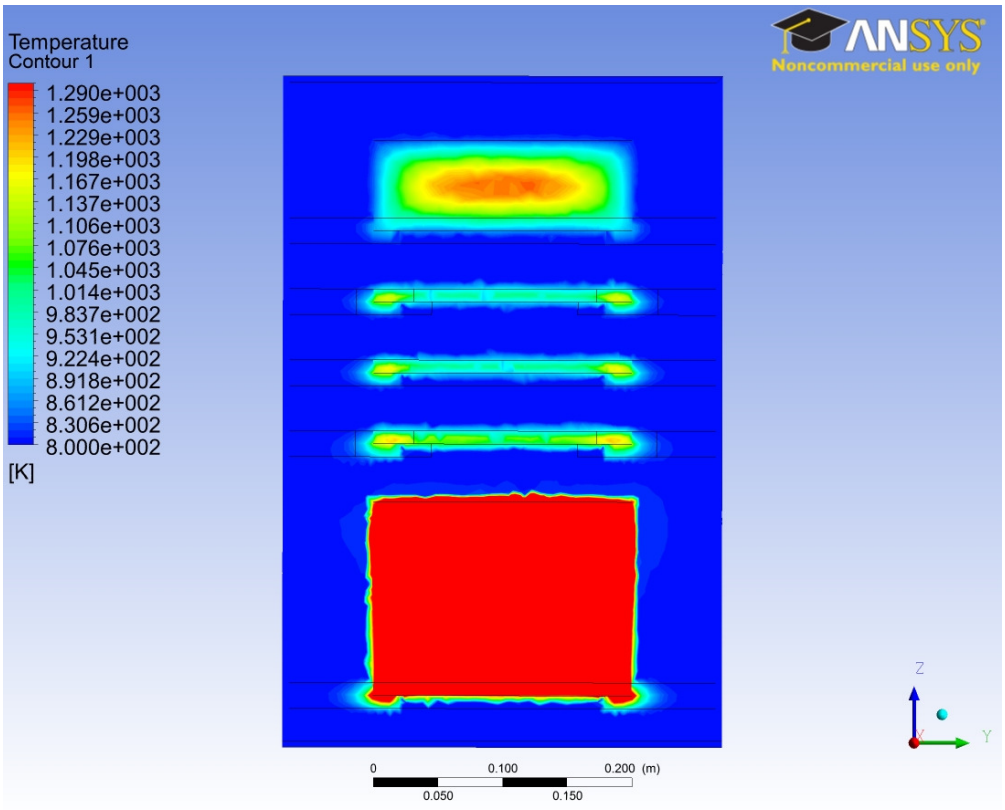

Figure 36: An example contour temperature plot (with a flow rate of 10 gallons per second) with fluid flow around the first iteration of the "Sandwich" design. The bottom stopping cylinder's temperature was maxed out by FLUENT at 5000 K which is beyond the scaling limits of the image processor so the cylinder appears as dark red.

However, to analyze the rest of the structures, various flow rates were tested to determine the peak temperatures associated with the remaining structures. Figure 37 shows the resultant peak temperatures for each structure using the average energy deposition. Based on the extreme temperatures as a result of having a large cylinder to stop the remaining protons from the primary plate targets, the next step was to mitigate those high temperatures by adding cooling channels. The stopping cylinder needed more effective cooling. In addition the Slowing Down cylinder required moderate cooling because the temperatures did not decrease with increasing velocities.

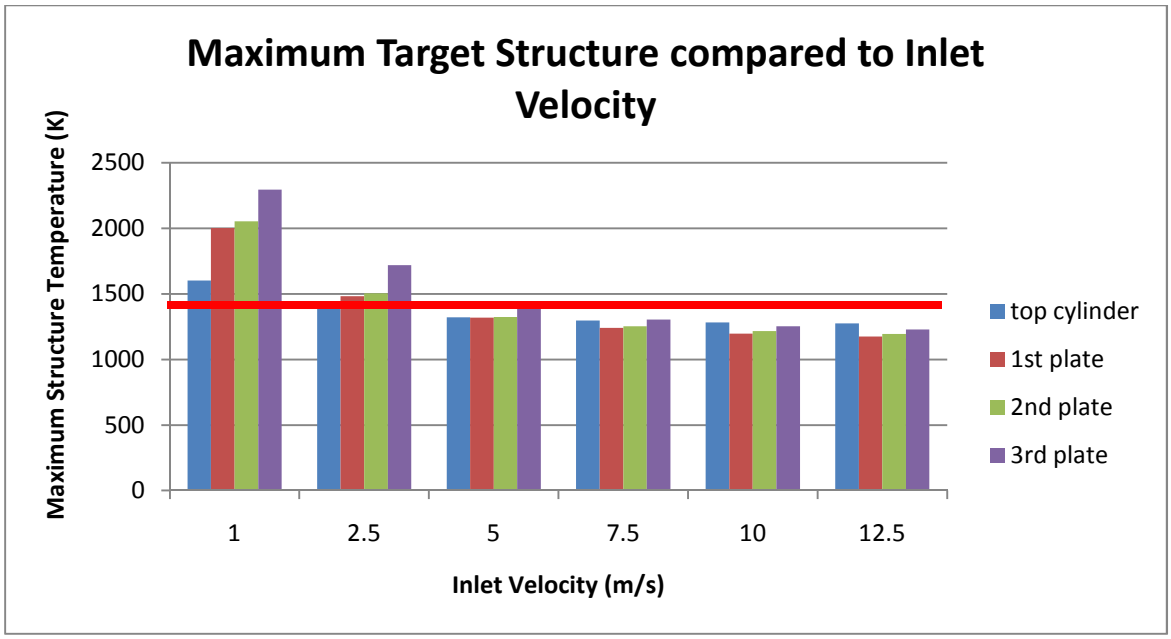

Figure 37: A plot of the peak temperatures of the target structures excluding the stopping cylinder to determine the next design change. The red horizontal line indicates the melting temperature of natural uranium which is approximately 1450 K. The data tables for this graph can be found in Appendix D: Data Tables.

The extreme temperatures produced from the preliminary runs indicated high flow rates would be necessary to effectively cool the target structures. Excluding the stopping cylinder, the lowest maximum temperature was 1175 K in the first plate. For structural reasons, keeping the highest maximum temperature approximately 200 K below the melting point of uranium was required since the natural uranium would have the lowest melting point of the spallation target structure. The top cylinder was at the design limitation of the 200 K criteria with a maximum temperature of 1274 K with an inlet velocity of 12.5 meters per second. As previously stated, material interactions between natural uranium and FLiBe were not considered as well as viscous heating effects and body forces on the uranium target structures.

The Second Iteration

The second iteration of the "Sandwich" design was to add cooling channels. Adding vertical cooling channels would have adversely affect the neutron fluxes and add a large amount of complexity which was not within the time allotted to determine the feasibility of using a natural uranium target for GEM*STAR. Therefore, to minimize the impact of adding cooling channels, the stopping cylinder and the Slowing Down cylinder were split up into multiple cylinders to allow for cooling. The space between the newly formed cylinders was maintained at a one centimeter spacing to allow for cooling and minimize the energy deposition in the FLiBe.

Figure 38 shows the second iteration of the design was slightly different than the first iteration. The design used two cylinders for the Slowing Down section and three cylinders for the stopping section. Each cylinder in the Slowing Down section was 3.5 centimeters thick, retained a diameter of 20 cm. The

three stopping cylinders had a thickness of five centimeters each and a diameter of 20 cm. In addition, instead of one large cooling passage, the target structure was broken into three separate flow channels; one section for the Slowing Down cylinders, one for the target plates and one for the stopping cylinders.

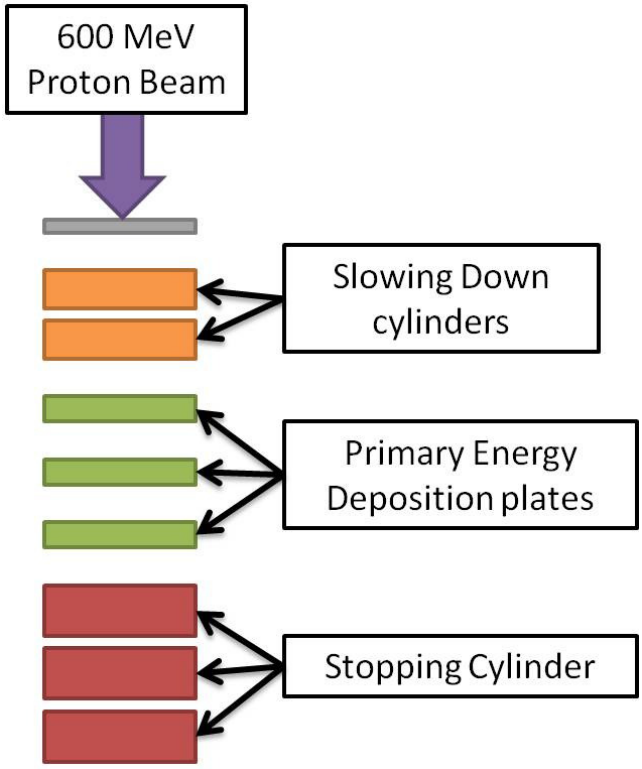

Figure 38: A simple diagram of the 2nd iteration of the "Sandwich" design.

Table 22 shows the neutronics associated with the second iteration. For this particular iteration, protons were tallied at the bottom of the target structure. The neutrons were tallied the same as the first iteration, in the radial, upwards and downwards directions. The protons which passed through the bottom of the target structures were a primary design concern. However, based on the number of protons leaving the bottom of the target structures which was around 1.6%, the second iteration had a sufficient amount target structure material to avoid proton damage to the bottom of the reactor of GEM*STAR. However, the tally for the protons did not take into account the original protons, so the protons tallied at the base of the target structure could potentially be spallation protons.

Table 22: The neutron counts and percentages as well as the proton counts and percentages associated with the second iteration design.

	Neutrons		Protons	
	count	percent	count	percent
radial	1.71E+08	84.49%	n/a	n/a
window	7.56E+06	3.73%	n/a	n/a
bottom	2.39E+07	11.78%	1.59E+04	1.59%
total	2.03E+08		1.00E+06	

Table 23 shows the energy deposition results from MCNPX. The total energy deposited is indicated in kW. However, the important values are the average and peak energy densities which were input into FLUENT. The Slowing Down cylinders have a moderate amount of energy deposition, where the second cylinder had a total energy deposition of 28.9 kW but compared to the primary target plates and stopping cylinders, the energy density is approximately a tenth of the values.

Table 23: Energy deposition for the second iteration from MCNPX including the average energy deposition, peak deposition and the ratio between the peak and average values.

	Target Structure	Total Energy Deposited (kW)	Average Energy Density (W/m^3)
Slowing Down Cylinders	1st cylinder	19.7	1.792E+07
	2nd cylinder	28.9	2.628E+07
Primary Target Plates	1st plate	88.3	2.811E+08
	2nd plate	93.2	2.967E+08
	3rd plate	88.6	2.820E+08
Stopping Cylinders	3rd cylinder	401.1	2.553E+08
	4th cylinder	236.6	1.506E+08
	5th cylinder	90.4	5.755E+07

Figure 39 shows the contour plot of the second iteration. Based on the image, the energy deposited in the target structures was not uniform with average heat generation. Rather, the heat deposited had peak values. The average energy deposition was determined from the generic volumetric tallies and not the mesh tallies utilized to depict the image. The peak energy deposited was in the three primary plates and a minor amount of energy is deposited in the flow separator. The energy deposited in the Slowing Down cylinders was so low; the image processor was unable to differentiate between the background and the first two cylinders. A large amount of energy is still deposited in the first two stopping cylinders but the energy deposited decreased by the third cylinder.

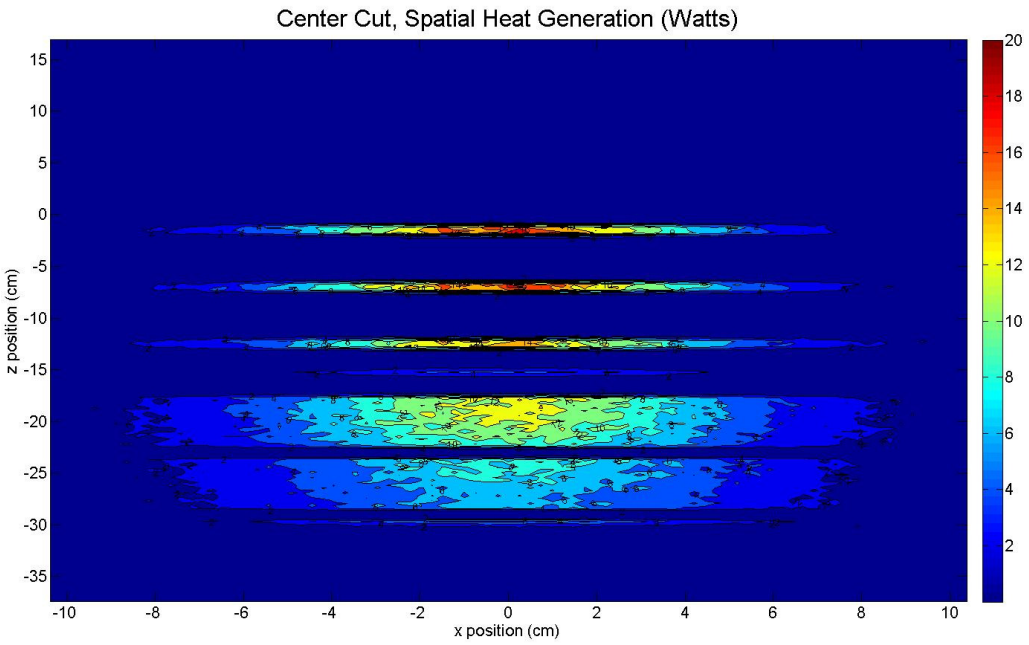

Figure 39: The temperature cross section contour plot of the second iteration. The slowing down cylinders do not indicate significant heat deposition, while the three target plates, two of the stopping cylinders and one flow separator (the thin increase in energy deposition after the third target plate) show significant energy deposition.

The average energy density values were utilized in FLUENT. The peak energy density values were planned for future iterations. For FLUENT, the fluid entered the side of each flow section through a rectangular inlet approximately two centimeters high and 30 centimeters wide.

Figure 40 shows a more detailed CAD design created in Inventor. Similar to the first iteration, each plate structure is supported from the bottom because associated body forces are ignored for the scope of this research. The Slowing Down cylinders and stopping cylinders have a one centimeters by one centimeters wide groove cut into their circumference to support them in the middle and direct the FLiBe cooling. The semi-transparent structures were the Hastelloy-N supports to clearly indicate the supporting areas and the target plates and cylinders. Based on the first iteration, a majority of the heat was not deposited in the outer edges of the targets. Therefore, for the MCNPX runs a constant solid structure was utilized in addition to ignoring the neutronics effects of the supports.

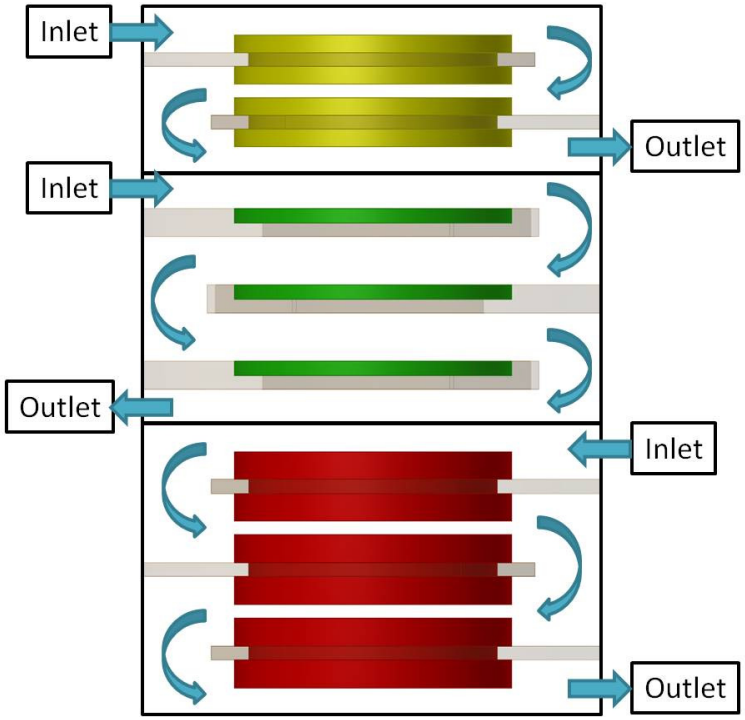

Figure 40: A CAD model of the support structures and flow structures for FLUENT for the second iteration of the "Sandwich" design. The flow paths are indicated by the turquoise arrows as well as the inlets and outlets for the various sections of the target structures.

Utilizing an inlet velocity of 10 meters per second as a starting point indicated from the first iteration, there was still a significant amount of heat being generated in the stopping cylinders which FLUENT peaks out the temperature at 5000 K. Table 24 shows some sample inlet velocities and resultant maximum temperatures inside each target structure. A flow rate of 14.17 gallons per section (inlet velocity of 10 m/s) was utilized as an arbitrary starting point. The Slowing Down section and the primary target plate section was able to maintain a flow rate of 14.17 gallons per section while the stopping cylinders had to have an increased velocity to make up for the extreme temperatures. The first stopping cylinder had a maximum temperature of 5000 K which was limited by FLUENT. However, the second and third stopping cylinders had a decreasing temperature as the flow rates increased.

Table 24: Some sample data for The second iteration, based on flow rates per section. The flow rates for the Slowing Down section and the plates was maintained at 10 meters per second and maintained. However, the stopping cylinder section was varied to decrease the maximum temperature.

			max temperatures (Kelvin)							
flow rate (gal/sec) by section			slow down cylinders		plates			stopping cylinders		
slowing	plates	stopping	1	2	1	2	3	1	2	3
14.17	14.17	14.17	915.67	967.97	1140.32	1159.06	1140.88	5000.00	2665.80	1505.57
14.17	14.17	21.25	918.35	967.89	1137.99	1144.31	1141.95	5000.00	2607.90	1487.79
14.17	14.17	28.33	915.67	967.57	1141.46	1164.37	1141.10	5000.00	2583.00	1477.58

Figure 41 shows a sample cross sectional temperature contour plot of the middle of the target structure. In addition, the maximum temperature of the target plates and Slowing Down cylinders appears to be localized at the support structure contact areas. The increased temperature at the contact areas for the support rings was due to the increased mass and inability to be cooled effectively by convection effects. For image processing purposes, the temperature was limited to 2000 K. Based on the raw data, the temperatures in the first and second stopping cylinders are beyond the temperature limit in the image.

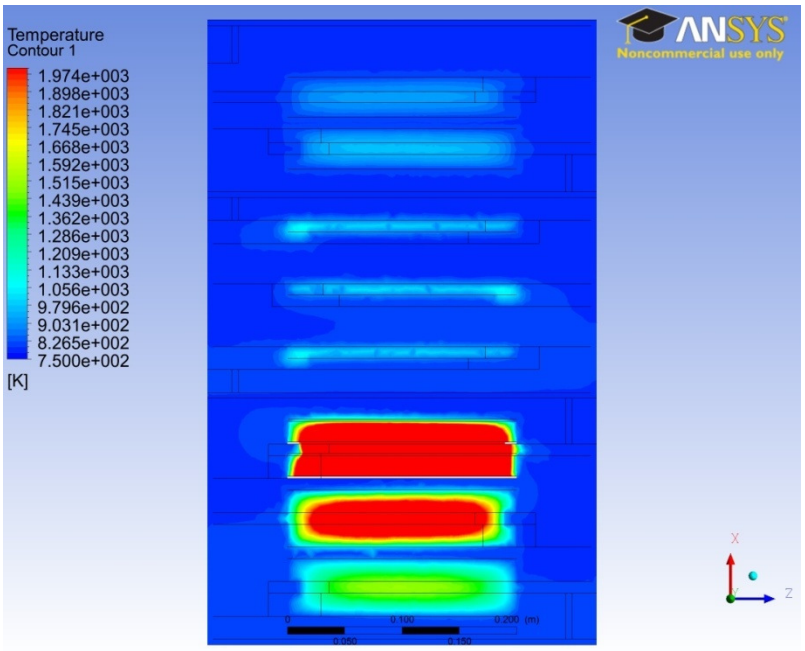

Figure 41: A sample cross section contour plot of temperature of the target structures for the second iteration of the "Sandwich" design. The flow rate for this image is 14.17 gallons per section for each target section.

Due to the extreme temperatures generated in the stopping cylinders, the stopping cylinder structures must be cooled more effectively. Therefore, increasing the number of target plates would provide a more effective method of reducing the maximum temperatures inside each target structure. However, separating the stopping cylinders into thinner plates would effectively result in high pressure drops and higher target outlet temperatures of the FLiBe which would require more extensive design of the external heat exchangers. Therefore, a third design iteration was considered to correct the issues with the first and second design iterations.

The Third Iteration

The third design iteration utilizes the previous MCNPX designs of multiple plates. To keep the effective energy deposition the same throughout the target structure, a system of two Slowing Down cylinders, eight primary target plates each one centimeter thick, and three stopping cylinders was utilized. Figure 42 shows a sample diagram of the target structure for the third iteration. Eight plates were utilized to provide the same effective stopping power as the second iteration by incorporating the stopping cylinders from that design into the target plates of the third iteration. The third iteration effectively

added more material than the previous two designs by adding three stopping cylinders. The purpose of the three stopping cylinders in this iteration is to stop protons and neutrons from striking the bottom of the reactor vessel.

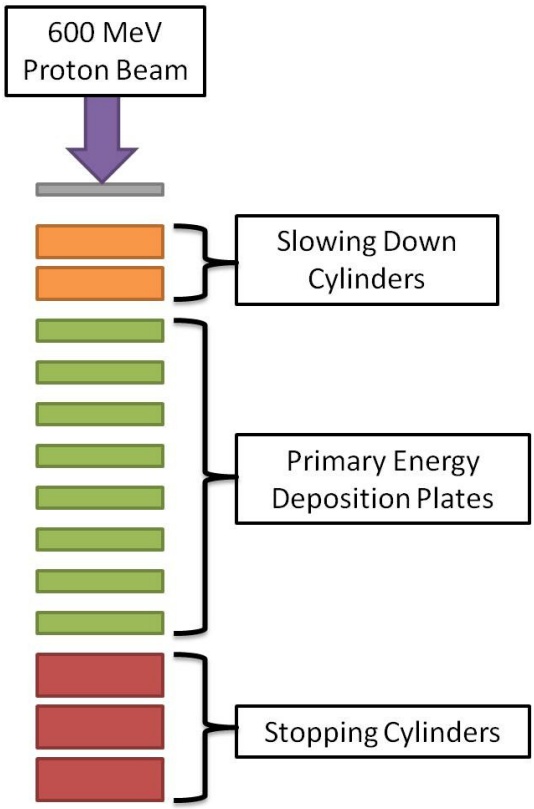

Figure 42: A diagram of the third iteration of the "Sandwich" design which utilizes eight target plates, two Slowing Down cylinders and three stopping cylinders.

Table 25 shows the neutron and proton tally results from the third iteration. Similar to the first iteration and 2, the third iteration included neutron tallies in the radial, upward and downward directions. However, the proton tallies taken for the third iteration included a newer tally of protons backscattering into the window/proton beam. With more physical structures, of the total number of neutrons produced, 92% exited the target structure radially, while less neutrons backscattered or through the bottom of the target structures. However, the total number of neutrons was reduced from the second iteration. The section on Neutron and Proton Tally Comparisons will compare the various neutronics and proton properties.

Table 25: The neutron count, proton counts for the radial, upward and downward directions for the third iteration.

	Neutrons		Protons	
	count	percent	count	percent
radial	1.30E+08	92.10%	n/a	n/a
window	5.93E+06	4.20%	4.91E+01	0.0049%
bottom	5.23E+06	3.70%	7.83E+03	0.7825%
total	1.41E+08		1.00E+06	

Using MCNPX, the results from the energy deposition tallies are shown in Table 26. Utilizing multiple target plates spread the heat across more volume with more effective cooling channels. In addition, peak energies were recorded compared to the first iteration and the second iteration. The peak energies can be compared to the average energy deposition with a ratio. The maximum ratios typically occurred in the flow separators which were not colored in Table 26. However, in the target structures, the maximum ratio of peak to average energy occurred in the first target plate which was to be expected.

Table 26: The resultant energy deposition per target structure, the average energy density, the peak energy density and the ratio of the peak to average energy deposition as well as the flow separators between the Slowing Down cylinders, Primary Target Plates and the Stopping Cylinders.

			Energy Density (Watts/cubic meter)		
	Target Structure	Total Energy Deposited (kW)	average	peak	ratio (peak/avg)
	window	2.32E-01	5.414E+05	1.529E+06	2.82
Slowing Down Cylinder	1st cyl	15.9	1.446E+07	2.276E+07	1.57
	2nd cyl	24.5	2.230E+07	4.506E+07	2.02
	1st sep	7.65E-04	1.949E+06	8.593E+06	4.41
Target Plates	1	86.4	2.751E+08	1.161E+09	4.22
	2	90.3	2.873E+08	1.137E+09	3.96
	3	83.8	2.667E+08	1.008E+09	3.78
	4	73.7	2.347E+08	7.862E+08	3.35
	5	62.5	1.991E+08	6.180E+08	3.10
	6	53	1.688E+08	4.995E+08	2.96
	7	44.5	1.417E+08	4.042E+08	2.85
	8	37.3	1.188E+08	3.119E+08	2.62
	2nd sep	7.07E-03	1.799E+07	1.051E+08	5.84
Stopping Cylinders	1st cyl	78.8	7.169E+07	2.815E+08	3.93
	2nd cyl	23	2.092E+07	4.110E+07	1.96
	3rd cyl	17.5	1.594E+07	3.305E+07	2.07
	3rd sep	4.67E-04	1.190E+06	4.165E+06	3.50

Figure 43 shows the energy deposition for each target structure in the design based on simulations conducted using MCNPX. The peaks indicated show the energy deposited in the separators to be relatively minimal compared to target structures themselves. The low energy combined with the relatively thin separator thickness can allow for adequate cooling. There were smaller peaks at the flow separators which can be addressed, but since the heat generated in the separators were not the concern with this research they were ignored for the FLUENT simulations but will need to be addressed in future research.

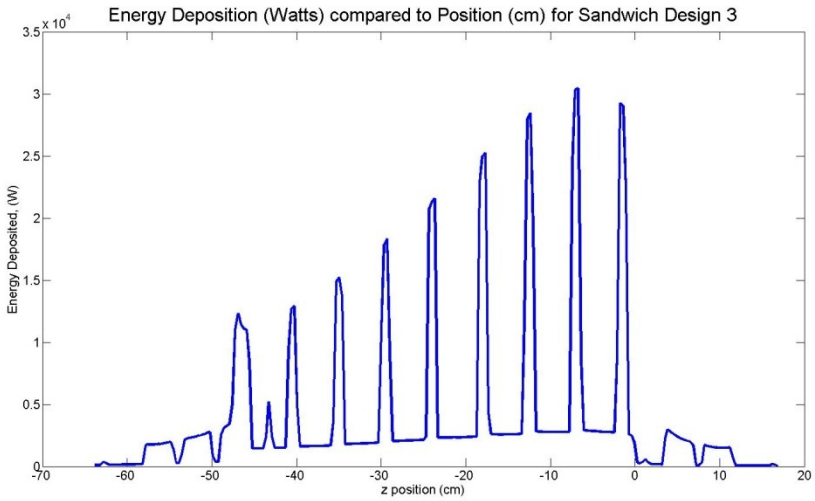

Figure 43: The energy deposition of the third iteration for the "Sandwich" design and the arrows indicate the peak energy deposited in the separator structures.

In addition, Figure 44 shows a contour plot of the center of the target structure which was exposed to a majority of the heat generated by the proton beam. The units were for the amount of heat generated per mesh cell size which was determined in MCNPX and then analyzed in MATLAB. The image does not contain the first two Slowing Down cylinders and the last two stopping cylinders due to minimal energy deposition in those target structures. As indicated from Figure 43, Figure 44 shows the energy deposited in a center cross section and visually depicts the heat which will be generated in the target structures. The peak energy density occurs in approximately a two centimeter radius from the center of each plate/cylinder.

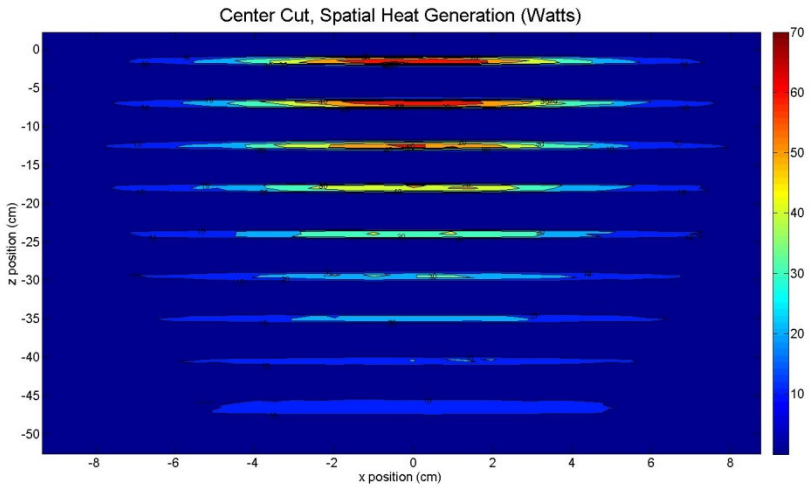

Figure 44: A contour plot of the energy deposited in watts in a center cross section of the target structure. The view does not include the Slowing Down cylinders and the last two stopping cylinders due to the minimal heat deposited in the structures.

To simplify the simulations in FLUENT, an assumption of no heat flux between the flow separators was created. Each flow structure was broken down into their respective sections to be tested in FLUENT due to computational limitations. The Slowing Down cylinder section, the stopping cylinder section and the target plates, which were broken into two sections of four plates each, were the designed sections which were tested in FLUENT. The target plates section was broken into two sections to allow for adequate mesh nodes to be utilized based on the memory limitations of the computer used to run the simulations. The addition of another flow separator was assumed to have minimal impact on the overall heat distribution based on the energy deposited in the separators from Figure 43 and Figure 44. In addition, adding a flow separator in the middle of the target plates section would effectively reduce the total heat deposited in the remaining target structures.

As opposed to utilizing the average energy deposition across each target structure such as in iteration one and two, an attempt to produce a relatively accurate 2-dimensional representation of the heat deposited in the structure was created. The heat being generated in the structure was similar to the proton beam pattern in the x-y plane of a Gaussian distribution. A center “plug” of uranium was created to be placed in the middle of the target structures; this plug was then allowed to produce the maximum local heat generation which was determined through the MCNPX simulations. Having a maximum energy density for heat generation in the center with an average volumetric heat generation for the rest of the structure produced a two-dimensional heat distribution for each structure. Figure 45 shows a more detailed image of a target plate with a two centimeter diameter plug in the middle. However, this simulation type was created only to simulate a Gaussian distribution, a User Defined Function (UDF) in FLUENT would have to be built for further research into these simulations.

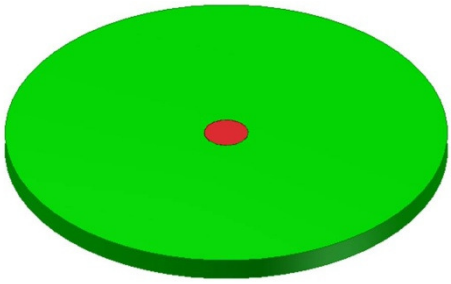

Figure 45: A detailed image of the maximum heat generation plug which was created for simulations in Fluent and would not exist in real life situations. The red plug uses the peak energy density, while the green section uses the average energy density.

Slowing Down Cylinders Cooling Section

Figure 46 shows the Slowing Down cylinders section designed in Autodesk Inventor® 2011. The sections still follow the planned cross flow pattern with the support rings acting as flow guides simultaneously. The inlet and outlets were rectangular (33 centimeters by 3.25 centimeters) to maximize the volume of FLiBe for cooling purposes. The target structures were supported in the middle using a channel which can be cut into the circumference of the target structures by a lathe. The channel was then utilized by the support rings. The channel was only one centimeter in depth to avoid exposure to high levels of energy deposition as indicated by Figure 44. The grey plugs in the middle of the yellow plates are utilized by FLUENT for the maximum energy density values while the yellow sections were utilized for the average energy density values. The semi-transparent sections were the FLiBe surrounding the Slowing Down cylinders and support rings. The outer structure was suppressed to show the inner structures.

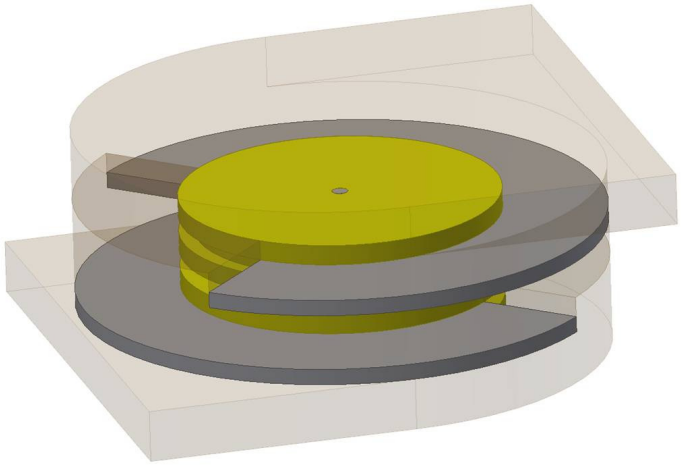

Figure 46: The CAD design of the Slowing Down cylinder cooling section which was built in Autodesk Inventor®. The semi-transparent sections indicate the fluid surrounding the Slowing Down cylinders. The grey plugs had the maximum energy density values while the yellow sections have the average energy density values for FLUENT simulations.

For the FLUENT simulations, the flow rates were varied from 0.03 to 14.17 gallons per second. Table 27 shows the resultant maximum temperatures produced for the Slowing Down cylinders. The faster the flow rate in the Slowing Down section resulted in a greater the reduction in maximum temperature. However, the curve appears to be leveling out after 1.4 gallons per second, which indicated diminishing returns in heat reduction. But since the maximum temperature in the target structure was several hundred degrees lower than the melting point of the target structures, pressure drop and various other factors such as embrittlement become more important in the design factors for the Slowing Down target section.

Table 27: The maximum temperatures produced from the Slowing Down cylinders for various flow rates and the pressure drop. The faster the flow rates, the lower the temperature and vice versa.

		max temp (Kelvin)		
flow rate (gallons/sec)	Reynolds	Top cylinder	Bottom cylinder	pressure drop (Pa)
0.03	130	1,372.55	1,468.34	4.48
0.14	650	1,108.12	1,203.49	57.09
0.28	1300	1,056.48	1,151.25	183.93
1.42	6500	867.95	915.40	5,881.88
2.83	13000	892.48	945.83	13,842.09
14.17	65000	868.90	900.10	279,898.14

In addition, flow rates were not the only concern; high pressure drops dictate pump size necessary for cooling. Using a flow rate of 1.42 gallons per second which was an entrance velocity of 0.5 meters per second, the minimum pressure drop across the Slowing Down section would be 5.88 kPa which does not include the pressure drop associated with the pipes. Therefore, the pump necessary to flow FLiBe through the Slowing Down target section would need to have a pressure greater than 6 kPa and a flow rate greater than 1.42 gallons per second. Figure 47 shows the velocity cross section contour plot. With an approximate maximum velocity of 1.5 meters per second, body forces could become an issue which must be addressed for refining this design.

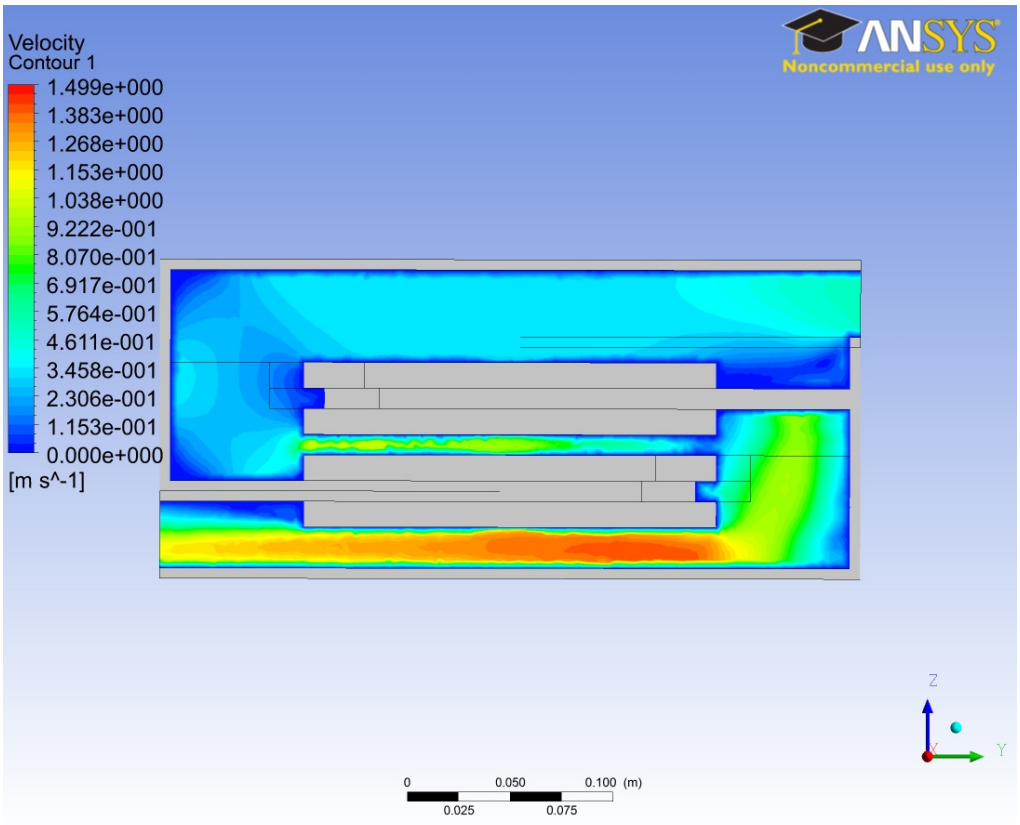

Figure 47: A sample velocity contour plot cross section of the Slowing Down section cooling FLiBe fluid.

However maintaining a flow rate of about 0.15 gallons a second would reduce the pressure drop to about 60 Pa while keeping the hydraulic forces at relatively low levels inside the structure and maintain a temperature below 1200 K.

Target Plates Cooling Section

The target plates were broken up into two primary sections, each containing four plates. However, based on computational limitations, a full scale test of the alternating cross flow design like the Slowing Down section was inadequate and produced incorrect and inconsistent results. Figure 48 shows a CAD image of the cross flow section design. The red plugs in the middle of the green target plates will utilize the maximum energy density determined from MCNPX for the FLUENT simulations while the rest of the plate will utilize the average energy density values. The semi-transparent region indicated the FLiBe fluid flow. The outer support tube was suppressed for demonstration purposes.

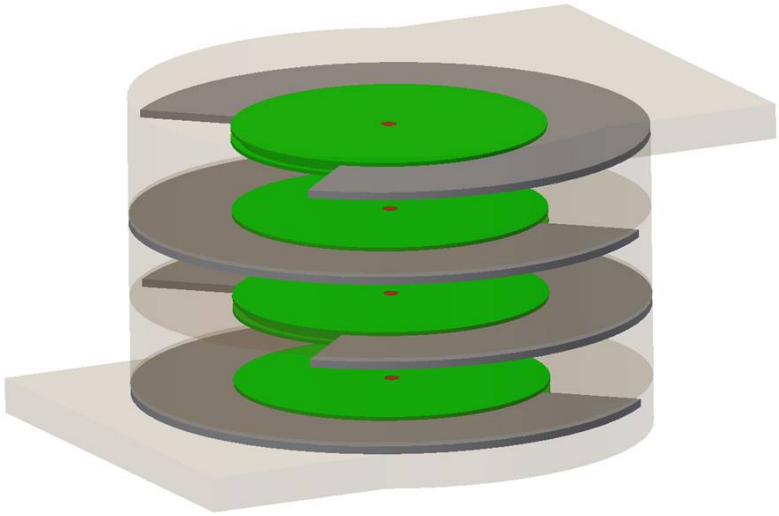

Figure 48: A CAD drawing of the cross flow section of the target with four one centimeter thick plates, the support rings which direct the cross flow and the fluid which is shown as the semi-transparent structures. The outer shell was hidden to indicate the flow paths.

Therefore, a simplified version negating the support plates but keeping the hydraulic diameter was maintained. Figure 49 shows the simplified cooling design to determine the feasibility for the one centimeter plate under maximum heat generation situations. The entry height of the FLiBe from the design in Figure 48 was effectively doubled to 33 centimeters by 10 centimeters. The reason was to allow for flow on both sides of the plate per the initial design. The primary difference was mono-directional flow of the FLiBe versus the original alternating one. Removing the reversal of the flow simplifies the meshing for FLUENT. In addition, potentially altering the design to only incorporate a mono-directional flow could take into account an alternate method of cooling for the overall spallation target for future designs.

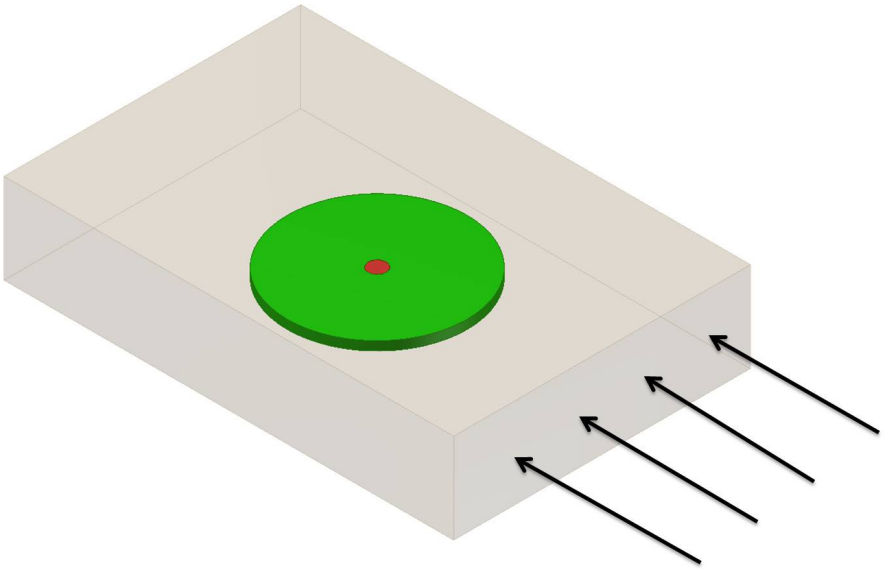

Figure 49: The test plate sections without the support plates and with fluid flowing over the plates evenly in one direction. The arrows indicate the direction of the fluid flow of the FLiBe.3

The simplified flow utilized the maximum heat deposition from the MCNPX simulation run which was 2.873×10^8 Watts per cubic meter for the average deposition and 1.137×10^9 Watts per cubic meter for the maximum deposition from Table 26. A "plug" was created in the center of the plate which contained the maximum energy density and the rest of the plate utilized the average energy deposition. The purpose of the plug was to mimic a Gaussian energy deposition in the plate and provide a potential overdesign of the target structure to encourage feasibility. The only variable which was varied was the inlet velocity which was utilized to determine the optimal flow rate.

Table 28 shows various properties and values produced from FLUENT for various flow rates for the one test plate section. With one plate, the only flow rate which could provide barely enough cooling was at 90 gallons per second or greater. However, the internal Reynolds number would be greater than 300,000. The convection coefficient was very high for the plate because the boundary layers were still developing from the thinner sides of the rectangular channel. The outlet temperature only increases by 0.06 K or less as velocity increases. The lack of temperature increase indicates that the heat was not being effectively transferred from the plate to the fluid.

Table 28: The various properties obtained from FLUENT simulations of the one centimeter thick simplified plate with maximum heat generation possible determined from MCNPX.

flow rate (gal/sec)	Reynolds Number	pressure drop (Pascal)	maximum plate temp (K)	average outlet temp (K)	convection coefficient ($W/m^2/K$)
0.872	3,000.00	52.61	2,220.09	751.003	2,513.92
4.359	15,000.00	331.24	1,889.78	750.648	3,189.55
8.718	30,000.00	729.87	1,788.22	750.457	3,569.32
43.588	150,000.00	6,006.09	1,631.26	750.127	4,322.35
87.177	300,000.00	15,892.02	1,492.91	750.064	5,350.74
435.884	1,500,000.00	286,618.70	1,296.56	750.013	7,744.41

In addition, if the design was increased to include four plates with a mono-direction flow, the flow rate would increase to 360 gallons per second. Having very high flow rates would require extensive design of the support structures to account for viscous effects, body forces and the pressure drop across the structure. Despite the massive flow rates, the maximum plate temperature still exceeds the ideal maximum temperature of 1200 K. Therefore, to reduce the maximum temperature more effectively, a decreased plate thickness would decrease the heat generation in the structure.

The stopping cylinder was ignored and the design was maintained through the next iteration based on the logic that if the target plate required an extraordinary amount of cooling, any design changes would require new neutronics which therefore would make any further design analyses useless.

The Fourth Iteration

The fourth design iteration utilized the same Slowing Down cooling section as the third iteration, but the primary target plate thicknesses were reduced to 0.5 cm. In addition, the number of plates was increased to 24 which were then split up into three, eight plate sections. At the base of the target structure there were three stopping cylinders, each of which was 3.5 centimeters thick. Figure 50 shows a basic design setup of the fourth iteration. Between each section were flow separators which were taken into account in the MCNPX simulations. In addition, the space between the target plates was decreased to one centimeter. The distance was decreased based on the previous designs from MCNPX which indicated that distance had a relatively minimal effect on neutron production as found in Varying the Distance between the Target Structures in the 2 Plate Design in Table 11 and Table 12

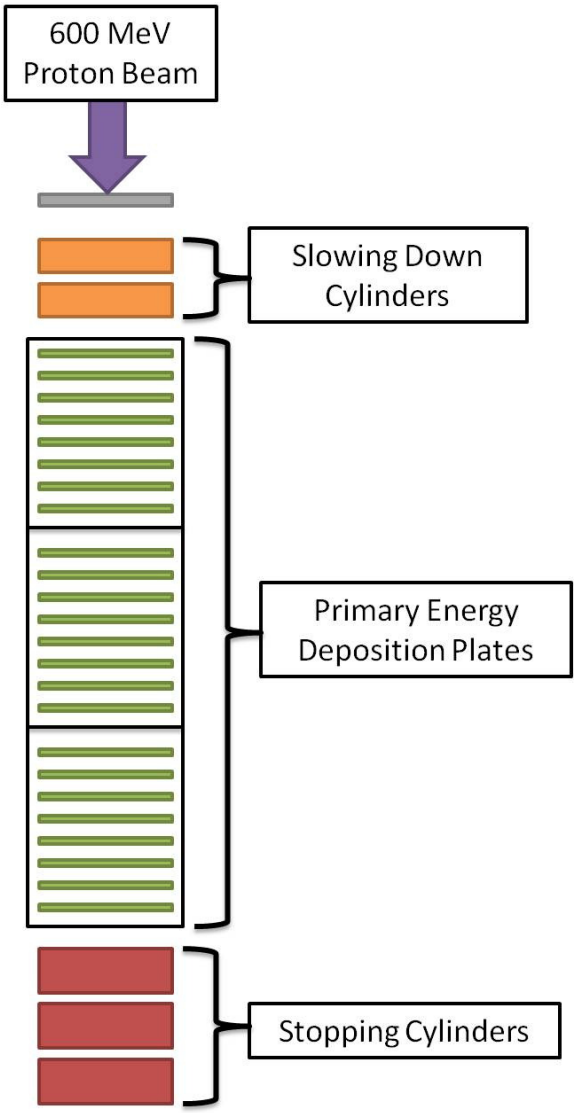

Figure 50: The basic setup of the 4th iteration with the 24 target plates, the 3.5 centimeters thick Slowing Down cylinders and the 3.5 centimeters thick stopping cylinders with the flow separators for each.

Not all the tallies converged for the MCNPX runs for the fourth iteration due to the complex geometry and computational hardware limitations with MCNPX 2.6 running on Windows 7. Table 29 shows the neutron and proton counts associated with the fourth iteration. The comparison between the various iteration's neutronics will be discussed in Neutron and Proton Tally Comparisons. Like the third iteration, about 92% of the neutrons produced were in the radial direction from the spallation target while the remaining 8% was backscattered or went through the bottom of the target structure. The backscatter was extremely low and the percentage of protons impacting the bottom of the target structure was less than a percent.

Table 29: The neutron count, proton counts for the radial, upward and downward directions for the fourth iteration.

	Neutrons		Protons	
	count	percent	count	percent
radial	1.48E+08	92.38%	n/a	n/a
window	6.33E+06	3.96%	33.91362	0.0034%
bottom	5.86E+06	3.67%	6750.316	0.6750%
total	1.60E+08		1.00E+06	

Figure 51 shows the energy deposition cross section based on the 29 target structures and the flow separators. Like the previous iterations, the support rings were ignored for neutronics calculations. Based on this image, the highest energy deposition occurs in approximately the sixth plate. Therefore, by using the tally results which can be found in Appendix D: Data Tables, the average and peak energy density deposition was approximately the same as the third iteration. However, the maximum energy deposited in the sixth target plate was only 47.6 kW compared to 90.3 kW from the third iteration. The total energy deposited in the target structure was reduced by half. In addition, the first two plates do not receive a high amount of energy deposition compared to the plates from the third iteration, but the energy deposited in the bottom stopping cylinders was significantly lower and along the same energy deposition values as the slowing cylinders.

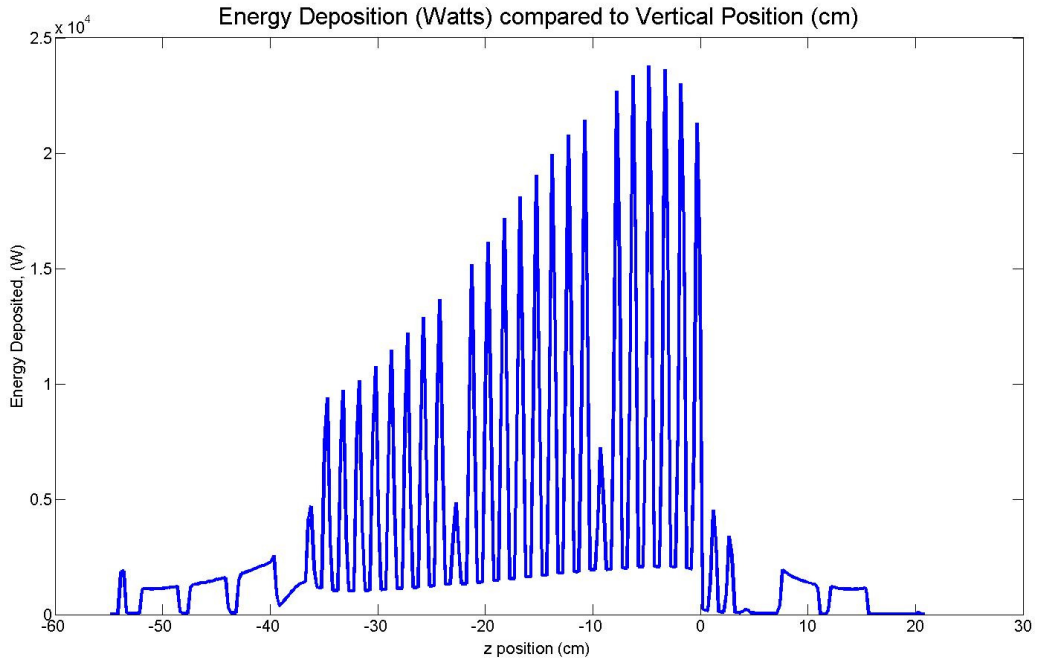

Figure 51: The energy deposition based on height for the fourth iteration which includes the 29 uranium target structures and the flow separators and proton beam window.

An initial attempt to build an alternating cross flow design for the target plate cooling sections failed due to computational hardware inadequacies to create a proper mesh. Therefore, the design was simplified to a feasibility design as in the third iteration. However, the hydraulic diameter was reduced to take into account an "effective" cross flow if multiple plates were utilized. The effective flow channel was reduced to a height of 2.5 centimeters and a width of 33 centimeters with no structural supports and then modeled in FLUENT.

Figure 52 shows the FLUENT simulation setup for the fourth iteration. The simulation was designed to mimic the internal flow of an alternating cross flow design, similar to the Slowing Down cylinder cooling section shown in the Slowing Down Cylinders Cooling Section. The setup looked very similar to Figure 49, except that the flow channel was much thinner because the distance between each plate side and the shell wall which is not shown, was decreased from 4.5 centimeters to one centimeter. The distance between the wall and the plate was meant to mimic the flow between the plates in a full design with a mono directional cross flow. The next design step would have been to create a setup with eight plates and then created a setup with the alternating cross flow.

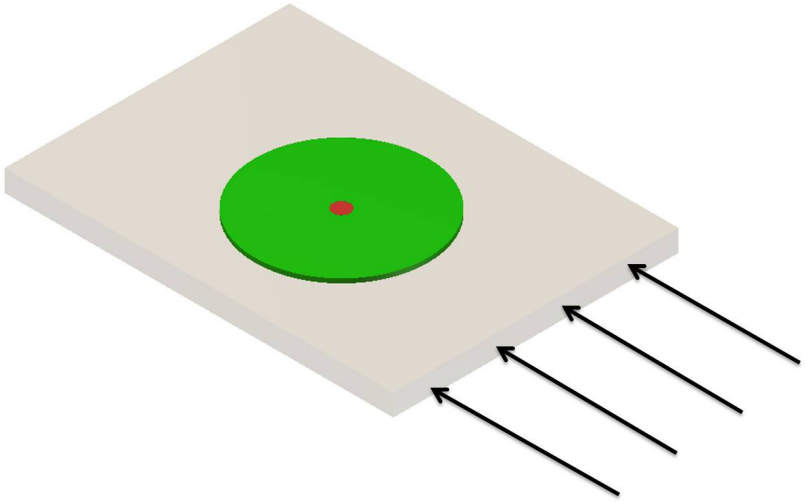

Figure 52: The fluid and a 0.5 centimeters target plate with a center plug for maximum energy density for the fourth iteration. The arrows indicate the fluid flow direction; the semi transparent region is the FLiBe while the plate is locked to the simulation axis.

However, Table 30 shows the important parameters for various flow rates for the design in Figure 52. The key resultant parameter was the maximum temperature of the plate. The only parameter which was varied was the flow rate. The energy density values utilized were 3.032×10^8 for the average energy density and 1.087×10^9 for the peak energy density from the sixth plate values determined from MCNPX. As stated previously the maximum temperature allowed for the target plates was less than 1200 K. Based on the coloring of the cells in Table 30, the red shaded cells indicate flow rates which would be inadequate for cooling, while the green cells indicate flow rates which would be adequate. Therefore, approximately 17 gallons per second was needed for one plate. If one plate needs 17 gallons per second, a mono directional flow across eight plates would require approximately 136 gallons per second.

Table 30: Key parameters as a result from a 0.5 centimeters plate using maximum energy deposition in the 6th plate of the complete MCNPX results. All parameters are utilizing turbulent flow models.

Flow rate (gal/sec)	Reynolds	max temp (K)	average outlet temp (K)	pressure drop (Pa)	average convection coefficient (W/m2/K)
2.179	10000	1764.40	751.64	1,040.06	1622.28
10.897	50000	1280.39	750.29	16,138.09	2913.23
13.077	60000	1246.29	750.22	23,134.72	3087.92
15.256	70000	1218.16	750.19	30,697.49	3240.30
17.435	80000	1190.50	750.17	36,882.48	3399.97
19.615	90000	1171.59	750.15	45,303.81	3511.61
21.794	100000	1161.89	750.13	54,661.81	3584.17

Even utilizing a borderline flow rate of 17.4 gallons per second, the Reynolds number was 80,000 for just one plate which indicated a difficulty in designing such flows in a confined space inside GEM*STAR. The average outlet temperature only increases by 0.17 degrees compared to the inlet temperature which indicates that the heat was not being transferred effectively to the fluid and then taken away which was similar to the results from the third iteration. In addition, the minimum pressure drop across the test structure was 37 kPa which indicates the body forces on any supporting structures holding the uranium must be robust and support the uranium properly to avoid structural damage and potentially flow blockage. Therefore, a design using a flow rate using 136 gallons a second would be practically infeasible due to the fluid forces as a result of the flows necessary to cool the spallation target plates.

Additionally, based on the average temperature increase across the plates for the third and fourth iteration designs, as well as contour plots of the temperature profiles, the heat generated in the plates was not being effectively conducted to the fluid where it could be taken away. Essentially, the thermal boundary layer must form much faster on the plate than the hydraulic boundary layers. This can only be achieved by a fluid with a low Prandtl number such as a liquid metal. Molten salts by comparison have a relatively high Prandtl number which leads them to having a rapid hydraulic boundary layer formation and a slowly developing thermal boundary layer which hinders heat transfer. The appeal of FLiBe despite this short coming is its ability to retain heat effectively for heat transfer if the fluid was allowed enough time and surface area to transfer the heat. However, in a situation with high energy densities, high Prandtl number fluids are not effective in heat transfer.

Concerning the stopping cylinders, the energy deposited in the cylinders was on the same order of magnitude as the Slowing Down cylinders. A reasonable assumption was cooling would be possible in a similar manner to the Slowing Down section for the third and fourth iterations with a reasonable flow rate and low hydraulic forces. However, further testing will be necessary to determine the feasibility of using stopping cylinders to prevent damage to the base of the target structure or the bottom of the containment vessel.

Neutron and Proton Tally Comparisons

Similar to the previous designs to the "Sandwich" design, the neutron tallies were analyzed and compared. Since the "Sandwich" design was similar across the four iterations, a direct comparison between each iteration was necessary. Figure 53 shows the neutron tallies associated with each design iteration as well as the number of neutrons tallied in each direction. Based on a visual inspection, the second iteration produced the most neutrons overall and in the radial direction. However, of the neutrons produced, only 85% of them would go in the radial direction which could allow for a significant amount of irradiation on the bottom of the target structure or reactor vessel. The proton window neutron count stayed at a relatively constant percentage of 4% across all the iterations. Additionally, in terms of feasibility, iterations one through three was not practically feasible and coincidentally the fourth iteration was feasible and produces an acceptable level of neutrons. For the fourth iteration, the number of potentially usable neutrons (in the radial direction) per proton was about 148 neutrons per proton. However, these neutrons were not tallied into fast or thermal a spectrum which was deemed beyond the scope of this research and should be considered for future neutronics studies.

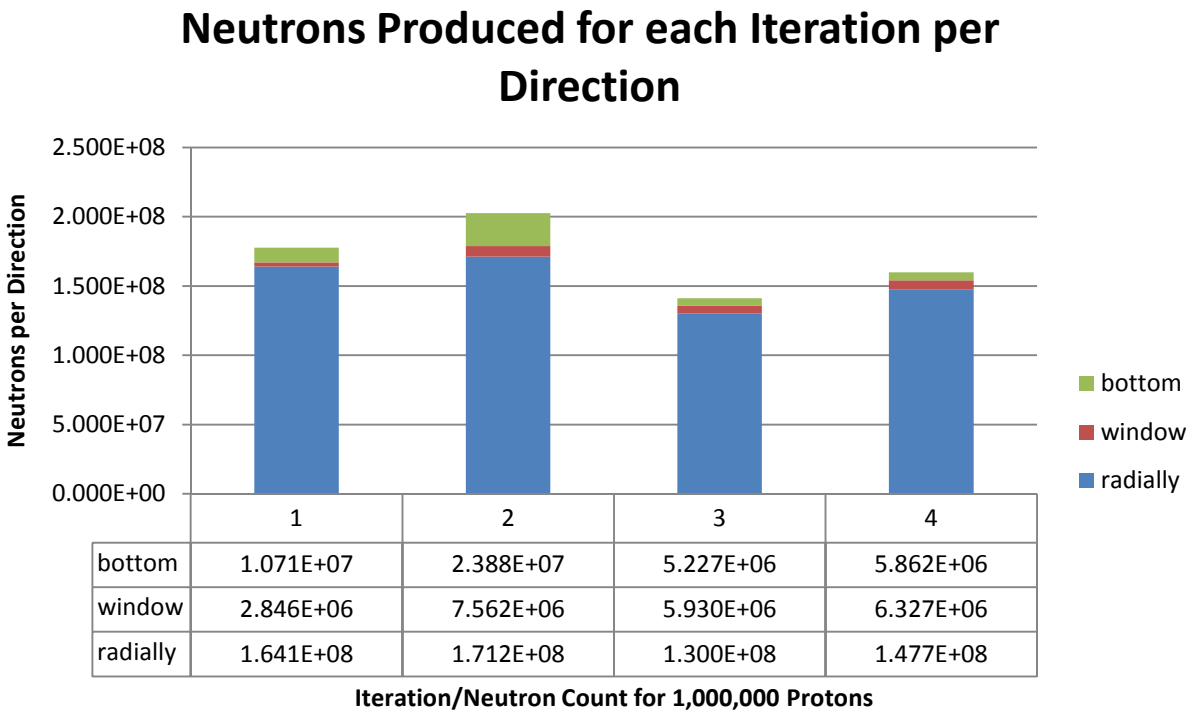

	1	2	3	4
bottom	1.071E+07	2.388E+07	5.227E+06	5.862E+06
window	2.846E+06	7.562E+06	5.930E+06	6.327E+06
radially	1.641E+08	1.712E+08	1.300E+08	1.477E+08

Figure 53: A graph depicting the neutron counts for 1 million incoming protons in three primary directions, radially, upwards and downwards. The upwards direction tally was taken at the proton beam window and the bottom tally was taken at the bottom of the target structure.

Several proton tallies were taken for the second through the fourth iteration. The first iteration tally was ignored after it was deemed that the design would not be feasible in a thermal setting. Therefore, Table 31 shows the remaining tallies taken for the second through fourth iteration. The primary purpose of

taking proton tallies was to determine the backscatter up the proton beam and the protons coming out the bottom of the spallation target structure which could potentially damage the bottom of the GEM*STAR reactor vessel. Out of the one million incoming protons, only 0.6% strikes the bottom of the reactor vessel for the feasible the fourth iteration design. In addition, the percentage of protons backscattering up the proton beam is 0.0034%. The backscatter is very low in comparison to the proton beam experiments from Oak Ridge National Labs which determined the neutron production and leakage which varied upwards of 16% neutron backscatter.(Ferguson, 2010)

Table 31: The proton counts for upwards direction (proton beam window) and the bottom of the target structure. The second iteration did not have a tally taken for the window. The total number of protons entering the target structure is 1,000,000.

	Iteration		
	2	3	4
window	n/a	49	34
bottom	15883	7825	6750

Additionally, the benchmark created by a solid cylinder of uranium was compared to the fourth iteration's spallation design in terms of total number of neutrons produced. The solid cylinder produced 2.21×10^8 neutrons while the fourth iteration produced 1.477×10^8 which was about 33% less neutrons produced. However, the practicality of the fourth iteration design was much greater than a partially melted solid uranium cylinder which could pose a significant hazard inside the GEM*STAR reactor. Although the backscatter of neutrons back up the beam is about the same 3% for both designs, but the number of neutrons backscattering for the fourth iteration was less than the cylinder design. The limiting factor in maximizing the number of neutrons was the cooling ability of the system utilizing FLiBe. A suggested design change should include a coolant which can doubly act as a spallation source to improve the number of neutrons produced from the spallation source.

Compared to the RACE experiment which performed high power simulations of their initial design, their potential design could have produced around 5×10^{13} to 10^{14} neutrons per second from the spallation source. The full power RACE reactor would operate between 50 and 150 MW_{th}. (Beller, et al., 2006) By comparison, the neutrons which could be produced by this GEM*STAR target design would be around 1.25×10^{18} neutrons per second. GEM*STAR would operate around 600 to 700 MW_{th}. Therefore, the spallation source using natural uranium as a primary spallation target and cooled with FLiBe could be producing approximately 1000 times the necessary neutrons for the subcritical core. The benefit of having excess neutrons is to transmute waste. However, in this particular case, for steady state operation of GEM*STAR could lead to the reactor going super critical. Reducing the number of neutrons will be necessary for full scale testing of a combination of the subcritical core and spallation source for GEM*STAR. Suggested design changes could be reducing the kinetic energy of the incoming protons or reducing the beam power to a level which would result in a neutron flux decrease by a factor of 1000. A benefit to a reduction in beam power or proton energy would result in less heat deposited in the spallation target which would allow for a practical design of a spallation source with uranium plates using FLiBe as a coolant.

Summary of Results

The fourth iteration of the "Sandwich" design was the optimal design created for the GEM*STAR neutron spallation source using FLiBe as a coolant. The fourth iteration was the optimal balance between neutronics and cooling capacity. The neutron production was only 67% of an ideal solid natural uranium target, but the neutron backscatter and protons going through the target were minimized to acceptable levels. The fourth iteration had approximately 3% for the neutron backscatter and less than one percent for the protons going through the target. However, based on the cooling requirements using FLiBe, the hydraulic forces make the fourth design iteration impractical despite adequately cooling of the Slowing Down cylinders and primary target plates.

Based on the requirements set forth by GEM*STAR, a proton beam energy of approximately 0.8 MW would be imparting its energy on a solid uranium target about 20 centimeters in diameter and an unknown depth into the natural uranium material. Assuming that all the energy from the beam was converted into heat energy, cooling a structure with 0.8 MW of heat energy was a difficult engineering task. Additionally, based on the initial tests, the natural uranium began to fission under the proton beam's energy which produced upwards of 2 MW of thermal energy deposited in the structure depending on the design being utilized.

In addition, the results from MCNPX indicated design trends for neutronics and heat generation. Large continuous structures such as a target cylinder would prove impossible to cool in a practical setting. Additionally, in a multiple plate target setup, varying the distances between the plates with a FLiBe coolant has a negligible impact on the heat deposited and neutron production. Therefore, the Bragg peak and the solid cylinder design were used as a guide to design the final "Sandwich" design. The idea was to induce a Bragg peak in the target plates, which required a method to "slow down" the protons to an acceptable level. This section was called the Slowing Down cylinder(s) which were able to induce peak energy deposition in the plates. Having a peak energy deposition in the plates would allow for effective cooling.

Due to the low energy density of the Slowing Down cylinders, a low flow rate of 0.15 gallons per second of FLiBe can effectively cool the Slowing Down cylinder structures. Additionally, the flow channel was an alternating cross flow pattern which used the cylinder supports as flow guides. However, due to the high energy densities found in the target plates, very high flow rates are necessary due to the nature of FLiBe being a high Prandtl number liquid which varies based on temperature. A simplified simulation was created which utilized one plate and a mono-direction cross flow, essentially a structure inside a narrow channel. A one centimeter thick plate was too thick to adequately cool at a reasonable flow rate. So the thickness of the plate was reduced to 0.5 centimeters thick and a feasible flow rate of about 17 gallons a second was achieved. However, if the design were to use an eight plate setup per flow section in the fourth iteration design, a mono directional flow rate of 136 gallons per second would be necessary. The hydraulic forces involved in such a design would prove to be impractical for the space constraints in GEM*STAR. Based on the energy densities from the fourth iteration for the stopping cylinders, cooling flow rates from the Slowing Down section would be adequate and practically feasible using FLiBe as a coolant.

The neutron fluxes produced by the fourth iteration's design were significantly higher than the neutron fluxes produced by full power simulations to the follow-up RACE program. The fourth iteration produced about 1000 times the neutrons necessary for GEM*STAR which can lead to some significant system design changes for GEM*STAR.

Overall, the use of FLiBe as a coolant and uranium as a target for GEM*STAR's neutron spallation target is feasible utilizing a "Sandwich" design which incorporates a set of Slowing Down cylinders to induce a Bragg peak in a set of primary target plates which produce the significant majority of the neutrons which can be used in the subcritical core. A set of stopping cylinders are at the bottom which contain about the same energy density as the Slowing Down cylinders which can be adequately cooled in the same fashion. However, based on the flow rates necessary to cool the target plates, the hydraulic forces would prove the design used in this thesis to be impractical for GEM*STAR and therefore more optimization of geometries will be necessary. Nevertheless, the use of a natural uranium spallation target proved promising. With further optimization of the target geometry and/or cooling flow paths, a practical design for GEM*STAR could be achievable."

Recommendations

There are several recommendations needed for future work on the GEM*STAR neutron spallation target related to the thermohydraulics of the designs and the use of FLiBe as a coolant. There are three primary methods to improve the spallation target while still utilizing a natural uranium target. The first method would require a refinement of the cooling flow around the primary target plates by either reducing the thickness of the plates below 0.5 centimeters or do an extensive design to account for the increased hydraulic forces to maintain the 0.5 centimeters thickness. Additionally, a more complete design should take into consideration the space constraints associated with the GEM*STAR reactor. The pump sizes and flow channels should also be considered as well as the pressure drop and power consumption if FLiBe is utilized. The final method to improve the spallation target would be to test alternate geometries and compare the neutron production.

The material interaction between the uranium and the FLiBe should be considered. The natural uranium could potentially dissolve in the FLiBe especially at high velocities at the boundary where the viscous forces can physically damage the natural uranium structures. Additionally, the neutron fluxes are extremely high for the target structure and the fluxes exceed that from the MSRE project from ORNL. Extensive testing of Hastelloy-N is necessary to determine the longevity of the entire target structure under high neutron fluxes and the proton fluxes at the beam window.

If the uranium dissolves in the FLiBe, coatings of another material can be used, but with high temperature gradients during start up and shut down of GEM*STAR, the coatings may crack over time due to the thermal expansion coefficient differences between the materials. The use of other materials could be explored for their structural, chemical and neutronics properties which may be better than Hastelloy-N because the cost of Hastelloy-N is very high.

Another option to alter GEM*STAR's design significantly is to utilize an alternative coolant, specifically a fluid which has a low Prandtl number such as liquid lead or lead bismuth eutectic. Compared to FLiBe, the melting point is much lower and has 10 times the thermal conductivity which would allow an energy dense system to remove heat more effectively with lower flow rates. The major problem based on qualitative observations of the thermal contour plots using FLiBe, is that the heat is not increasing the temperature of the fluid surrounding heat generating structures during steady state operation by any significant amount. A liquid metal could pull the heat from the uranium target through conduction more effectively. Essentially, FLiBe acts like a liquid ceramic, which is unwilling to absorb heat readily, but once it does, it has the ability to retain the heat. A liquid metal is willing to absorb heat but will not readily retain the heat which would be ideal for an energy dense structure such as a spallation target.

Programs such as MEGAPIE utilized a fully liquid lead bismuth eutectic spallation target under a 1 MW beam power proton accelerator. A pure liquid target has several advantages over solid targets, such as an ability to remove impurities as they form and maintain relatively low temperatures. The Russians have perfected lead and lead bismuth technologies in modern reactors so the metallurgy technology is readily available as well. Cooling is easily taken care of using radiators external to the reactor as well and the only concern for the target is the structures containing the spallation material. It would be useful to

explore a hybrid target design using lead bismuth eutectic with uranium plates. The lead-bismuth eutectic coolant would act as a supplementary spallation target in conjunction with the multiplying medium of the uranium plates. This particular design could maximize the production of neutrons while allowing for adequate cooling.

On the computational end of the spallation target, for complex flows for cooling, large computationally intense based computers or a cluster would be ideal for designing the GEM*STAR fluid flows especially under high flow rates which can turn turbulent. The computer hardware available for this research was not adequate to provide optimal designs or in some cases the hardware/software was only able to provide results for simplistic feasibility studies. In addition, the entire spallation source for GEM*STAR should be broken up into two separate projects concerning the neutronics and the thermohydraulics for separate professionals to collaborate on the designs. Finally, optimizing and validating thermohydraulic parameters of the designs will be necessary to move beyond a feasibility study.

Additionally, the research performed was intended to be a feasibility study towards a potential application of a natural uranium neutron spallation target using FLiBe as a coolant. Simple and complex geometries and scenarios were performed to explore as many options as possible towards determining some degree of validity. However, many of the conclusions drawn from this research were not validated due to time constraints and hardware computational limitations.

Bibliography

1. (2007, June 21). (MediaWiki) Retrieved April 12, 2011, from CFD Online: http://www.cfd-online.com/Wiki/Standard_k-epsilon_model
2. *Ask a Mathematician/Ask a Physicst*. (2011, March 13). (WordPress) Retrieved April 10, 2011, from Q: Are all atoms radioactive?: http://www.askamathematician.com/?p=5726
3. Audi, G., A.H., W., & C, T. (2003, December 22). *Atomic Mass Adjustment.* Retrieved Febuary 2011, from National Nuclear Data Center: http://www.nndc.bnl.gov/amdc/masstables/Ame2003/mass.mas03
4. Bauer, G., Salvatores, M., & Heusener, G. (2001). MEGAPIE, a 1 MW Pilot Experiment for a Liquid Metal Spallation Target. *Journal of Nuclear Materials* , 17-33.
5. Bejan, A. (2004). *Convection Heat Transfer.* Durham: John Wiley & Sons, Inc.
6. Beller, D., Harmon, F., O'Kelly, S., Charlton, W., Lee, J., Ward, T., et al. (2006). *Final Report of the U.S. Reactor-Accelerator Coupling Experiments (RACE) Project.*
7. Beller, T. E. (2007). *Neutronics analysis of the high-power race target.* Dissertation, University of Nevada, Nuclear Physics, Las Vegas.
8. Ferguson, P. (2010). Neutron Sources Globally. *International Workshop on Accelerator Drive Sub-critical systems & Thorium Utilization* (p. 51). Blacksburg, VA: Oak Ridge National Lab.
9. *Generation IV Nuclear Reactors.* (2010, December). Retrieved January 2011, from World Nuclear Association Web Site: http://www.world-nuclear.org/info/inf77.html
10. Haynes International. (n.d.). *Haynes International.* Retrieved Febuary 21, 2011, from Haynes International Website: http://www.haynesintl.com/pdf/h2052.pdf
11. Hendricks, J., & Schwarz, R. (2010, September 20-24). MCNPX Intermediate Workshop. Virginia Beach.
12. Idaho Accelerator Center. (2007). *Reactor-Accelerator Coupling Experiments (RACE) Project*. (Idaho State University) Retrieved 3 27, 2011, from AFCI RACE Project: http://iac.isu.edu/research/RACE.html
13. Kadi, Y., & A., H.-M. (2006). Energy amplifier systems: Simulation and experiments in the field. *7th International Conference on Accelerator Applications* (pp. 573-577). Elsevier.
14. Koger, J. W. (1972). *Evaluation of Hastelloy N Alloys After Nine Years Exposure to Both a Molten Fluoride Salt and Air at Temperatures from 700 to 560 C.* Oak Ridge: Oak Ridge National Labs.
15. Lamarsh, J. R., & Baratta, A. J. (2001). Binding Energy. In *Introduction to Nuclear Engineering* (Third ed., p. 33). Prentice Hall.
16. LANL. (2008, April). MCNPX USER's MANUAL. *(Version 2.6.0)* . (D. B. Pelowitz, Ed.)
17. LeCounte, R. D. (2007). *Thermal hydraulic analysis of the High-Power Race Target.* Dissertation, University of Nevada, Las Vegas, Mechanial Engineering, Las Vegas.
18. McCoy, H. J. (1970). *An Evaluation of the Molten-Salt Reactor Experiment Hastelloy N Surveillance Specimens - Third Group.* Oak Ridge: Oak Ridge National Labs.
19. Nifenecker, H., Meplan, O., & David, S. (2003). *Accelerator Driven Subcritical Reactors.* (R. R. Greiner, Ed.) London, France: Institute of Physics Publishing Bristol and Philadelphia.

20. Nifenecker, H., Meplan, O., & David, S. (2003). ADSR Principals. In H. Nifenecker, O. Meplan, & S. David, *Accelerator Driven Subcritical Reactors* (pp. 93-98). London: Institute of Physics Publishing.
21. Oak Ridge National Lab. (n.d.). *How the Spallation Neutron Source Works*. (UT-Battelle LLC) Retrieved 1 19, 2011, from Oak Ridge National Lab: http://neutrons.ornl.gov/facilities/SNS/works.shtml
22. Oak Ridge National Lab. (2005). *SNS Parameters List.* Oak Ridge, TN: UT-BATTELLE, LLC.
23. Oak Ridge National Lab. (2006). *Spallation Neutron Source Project Completion Report.* Oak Ridge: UT-BATTELLE, LLC.
24. Oak Ridge National Laboratory. (1964). *Molten-Salt Reactor Program Semi Annual Progress Report .* Oak Ridge: Oak Ridge National Labs.
25. O'Kelly, D. S. (2008). *Operation and Reactivity Measurements of an Accelerator Driven Subcritical TRIGA Reactor.* Dissertation, University of Texas at Austin, Austin.
26. Paul Scherrer Institut. (2008, July). *Megapie*. Retrieved January 2011, from PSI: Paul Scherrer Institut: http://megapie.web.psi.ch/
27. Paul Scherrer Institute. (2004, November 3). The PSI/MEGAPIE Target. *BENE Workshop, DESY* . Europe.
28. Smith, B., Leung, W., & Zucchini, A. (2007). Coupled fluid/structure analyses of the MEGAPIE spallation source target during transients. *11th International Topical Meeting on Nuclear Reactor Thermal Hydraulics* (pp. 1656-1667). Elsevier.
29. Sohal, M. S., Ebner, M. A., Sabharwall, P., & Sharpe, P. (2010). *Engineering Database of Liquid Salt Thermophysical and Thermochemical Properties.* Idaho Falls: Idaho National Laboratory.
30. Turner, J. E. (2007). Nuclear Binding Energies. In J. E. Turner, *Atoms, Radiation, and Radiation Protection* (pp. 58-60). Oak Ridge, TN, United States: WILEY-VCH Verlag GmbH&Co. KGaA.
31. Vogelaar, B. (2010). GEM*STAR. *International ADS Conference*, (p. 38). Blacksburg.
32. Vogelaar, R. B., & Bowman, C. D. (2010). GEM*STAR: The Alternative Reactor Technology Comprising Graphite, Molten Salt and Accelerators. Los Alamos, NM; Virginia Tech, Blacksburg; Duke University, Durham, NC.

Appendix A: General Equations

The turbulence model equations were determined from the wiki from CFD Online. (CFD Online, 2007)

A.1 Standard k-ε Model

Equations (30) and (31) are the transport equations utilized by the k-ε model during a steady state flow.

$$\frac{\partial}{\partial x_i}(\rho k u_i) = \frac{\partial}{\partial x_j}\left[\left(\mu + \frac{\mu_t}{\sigma_k}\right)\frac{\partial k}{\partial x_j}\right] + P_k + P_b - \rho\varepsilon - Y_M + S_k \tag{30}$$

$$\frac{\partial}{\partial x_i}(\rho \varepsilon u_i) = \frac{\partial}{\partial x_j}\left[\left(\mu + \frac{\mu_t}{\sigma_\epsilon}\right)\frac{\partial \varepsilon}{\partial x_j}\right] + C_1\frac{\varepsilon}{k}(P_k + C_3 P_b) - C_2\rho\frac{\varepsilon^2}{k} + S_\varepsilon \tag{31}$$

Where ρ is the density, k is the turbulent kinetic energy, ε is the turbulent dissipation rate, μ is the viscosity, μ_t is the turbulent viscosity, σ_k is the turbulent Prandtl number for k, σ_ε is the turbulent Prandtl number for ε, P_k is the generation of turbulent kinetic energy from velocity gradients, P_b is the turbulent kinetic energy due to buoyancy forces, Y_M is the ratio of the fluctuating dilation in compressible turbulence to overall dissipation rate, S_k and S_ε are user defined sources. Equation (32) shows the equation utilized to find the turbulent viscosity

$$\mu_t = \rho C_\mu \frac{k^2}{\varepsilon} \tag{32}$$

Where C_μ is a constant associated with the turbulent viscosity. Equation (33) and (34) show how the generation of turbulent kinetic energy from velocity gradients is determined.

$$P_k = \mu_t S^2 \tag{33}$$

$$S \equiv \sqrt{2S_{ij}S_{ij}} \tag{34}$$

Where S is the modulus of the mean rate-of-strain tensor. Equations (35) and (36) show the turbulent kinetic energy due to buoyancy forces.

(35) $$P_b = \beta g_i \frac{\mu_t}{Pr_t} \frac{\partial T}{\partial x_i}$$

(36) $$\beta = -\frac{1}{\rho}\left(\frac{\partial \rho}{\partial T}\right)_\rho$$

Where β is the coefficient of thermal expansion, g_i is the gravitational constant and Pr_t is the turbulent Prandtl number. Table 5 shows the constants associated with the standard k-ε model.

Table 32: The constants for the standard k-ε model.

C_1	1.44
C_2	1.92
C_μ	0.09
σ_k	1.0
σ_ε	1.3

A.2 RNG k-ε Model

Equations (18) and (19) show the transport equations for the RNG turbulence model, while equations (20) through (22) show the supporting equations for steady state flow.

(37) $$\frac{\partial}{\partial x_i}(\rho k u_i) = \frac{\partial}{\partial x_j}\left[\alpha_k \mu_{eff} \frac{\partial k}{\partial x_j}\right] + P_k + P_b - \rho\varepsilon - Y_M + S_k$$

(38) $$\frac{\partial}{\partial x_i}(\rho \varepsilon u_i) = \frac{\partial}{\partial x_j}\left[\alpha_k \mu_{eff} \frac{\partial \varepsilon}{\partial x_j}\right] + C_1 \frac{\varepsilon}{k}(P_k + C_3 P_b) - C_2{}^* \rho \frac{\varepsilon^2}{k} + S_\varepsilon$$

(39) $$C_2^* = C_2 + \frac{C_\mu \eta^3 \left(1 - \frac{\eta}{\eta_0}\right)}{1 + \beta \eta^3}$$

(40) $$\eta = \frac{Sk}{\varepsilon}$$

(41) $$S = \sqrt{2 S_{ij} S_{ij}}$$

Where α_k is the inverse effective Prandtl number for k, α_ε is the inverse effective Prandtl number for ε, μ_{eff} is the effective turbulent viscosity and C_2^* is a modified constant for the RNG model shown in equation (39). Equation (40) shows the η term to calculate C_2^* and equation (22) shows that S is a tensor. Table 33 shows the constants associated with the RNG turbulence model.

Table 33: The constants for the k-ε RNG model.

C_1	1.42
C_2	1.68
C_μ	0.0845
σ_k	0.7194
σ_ε	0.7194
η_0	4.38
β	0.012

A.3 Realizable k-ε Model

Equations (42) and (43) show the transport equations associated with the Realizable k-ε model for steady state flows. Equations (44) through (47) show the supporting equations necessary to solve the transport equations.

(42) $$\frac{\partial}{\partial x_i}(\rho k u_i) = \frac{\partial}{\partial x_j}\left[\left(\mu + \frac{\mu_t}{\sigma_k}\right)\frac{\partial k}{\partial x_j}\right] + P_k + P_b - \rho\varepsilon - Y_M + S_k$$

(43) $$\frac{\partial}{\partial x_i}(\rho \varepsilon u_i) = \frac{\partial}{\partial x_j}\left[\left(\mu + \frac{\mu_t}{\sigma_\epsilon}\right)\frac{\partial \varepsilon}{\partial x_j}\right] + \rho C_4 S\varepsilon - \rho C_5 \frac{\varepsilon^2}{k + \sqrt{\nu\varepsilon}} + C_1 \frac{\varepsilon}{k} C_3 P_b + S_\varepsilon$$

(44) $$C_4 = \max\left[0.43, \frac{\eta}{\eta + 5}\right]$$

(45) $$\eta = \frac{Sk}{\varepsilon}$$

(46) $$S = \sqrt{2S_{ij}S_{ij}}$$

(47) $$\mu_t = \rho C_\mu \frac{k^2}{\varepsilon}$$

The variables stay the same as the standard and RNG models, however the major difference is C_μ is no longer constant. Equations (48) through (52) show the supporting equations to determine C_μ.

(48) $$C_\mu = \frac{1}{A_0 + A_s \frac{kU^*}{\varepsilon}}$$

(49) $$U^* \equiv \sqrt{S_{ij}S_{ij} + \widetilde{\Omega}_{ij}\widetilde{\Omega}_{ij}}$$

(50) $$\widetilde{\Omega}_{ij} = \overline{\Omega_{ij}} - 3\varepsilon_{ijk}\omega_k$$

(51) $$A_s = \sqrt{6}\,\cos\left[\frac{1}{3}\cos^{-1}\left(\sqrt{6}\,\frac{S_{ij}S_{jk}S_{ki}}{\left(S_{ij}S_{ij}\right)^{3/2}}\right)\right]$$

(52) $$S_{ij} = \frac{1}{2}\left(\frac{\partial u_j}{\partial x_i} + \frac{\partial u_i}{\partial x_j}\right)$$

Where $\overline{\Omega_{ij}}$ is the mean rate-of rotation tensor in the rotating reference frame with ω_k as the angular velocity.

Table 34: The constants for the k-ε RNG model.

C_1	1.44
C_5	1.9
σ_k	1.0
σ_ε	1.2
A_0	4.04

Appendix B: Material Properties

B.1 Lithium Fluoride- Beryllium Fluoride, FLiBe

Lithium fluoride-beryllium fluoride ($2LiF\text{-}BeF_2$) has a 67%-33% mol composition, the short name is FLiBe. The properties were obtained from the Engineering Database of Liquid Salt Thermophysical and Thermochemical Properties from Idaho National Laboratory. (Sohal, Ebner, Sabharwall, & Sharpe, 2010)

Equation (53) shows the density for the temperature range of 732.2K up to 4498.8K

$$\rho = 2415.6 - 0.49072\,T \tag{53}$$

Equation (54) shows the viscosity equation from 873K to 1073K

$$\mu = 0.000116\,e^{3755/T} \tag{54}$$

Table 35 shows the specific heat capacity and thermal conductivity utilized.

Table 35: The heat capacity (c_p) and thermal conductivity (k) utilized for FLiBe in the MCNPX and FLUENT simulations.

c_p	2365 J/kg K
k	1.0 W/m K

B.2 Hastelloy-N

All data was obtained from datasheets available from Haynes International.(Haynes International) Hastelloy-N has very good anti corrosion properties against molten salts up to temperatures around 1200 K The melting point of Hastelloy-N is in the range of 1600 K to 1700 K. The density of Hastelloy-N is 8.86 g/cm^3. The thermal conductivity is about 20 W/m K and the specific heat is around 500 J/kg K. The physical properties of Hastelloy-N are very close to the values of standard carbon steel which was utilized for FLUENT simulations. Table 36 shows the chemical composition of Hastelloy-N based on a weight percentage which was utilized for MCNPX calculations.

Table 36: The chemical composition in weight percent of Hastelloy-N which was used for MCNPX simulations. The [a] indicates as a balance and the * indicates a maximum.

Nickel	71[a]
Chromium	7
Molybdenum	16
Iron	5*
Silicone	1*
Manganese	0.8*
Carbon	0.08
Other	Co = 0.2* Cu = 0.35* W = 0.5* Al+Ti = 0.35*

B.3 Natural Uranium

MCNPX has a built in material generator for natural uranium which was used for the neutronics simulations. FLUENT used the basic properties of natural uranium. The density of natural uranium is 18.9 g/cm3, the specific heat is 120 J/kg K and the thermal conductivity is 27.5 W/m K.

Appendix C: Important Analytical Calculations

*C.1 GEM*STAR Beam Power Calculation*

The proposed beam power of GEM*STAR could use a wide range of beam currents and proton kinetic energies. For the purposes of this research, the beam power was set at 1.35 mA and the proton kinetic energy was set at 600 MeV. Table 37 shows the conversion factors necessary to determine the beam power associated with the GEM*STAR proton accelerator.

Table 37: The conversions necessary to determine the beam power associated with GEM*STAR's proton accelerator.

1 Coulomb = $6.24150965 \times 10^{18}$ protons
1 MeV = $1.60217646 \times 10^{-13}$ Joules

The following is the calculation necessary to determine the beam power.

$$0.00135\ amps * \frac{1\ Coulomb/sec}{amp} * \frac{6.24150965(10^{18})\ protons}{Coulomb} = 8.426(10^{15})\ protons/sec$$

$$600\ \frac{MeV}{proton} * \frac{1.60217646(10^{-13})\ Joules}{1\ MeV} * 8.426(10^{15})\ \frac{protons}{sec} = 809996.33\ \frac{Joules}{sec}$$

$$\sim 0.81\ Megawatts\ of\ beam\ power$$

C.2 Theoretical Flow Rate for Cooling a Cylinder in a Cross-flow

For the purposes of determining the feasibility of cooling a cylinder 20 centimeters in diameter and 30 centimeters thick, an analytical model was used in the context of an external flow. The surface temperature was set at 1200 K which indicates the internal temperature of a cylinder would be even greater. However setting the surface temperature to 1200 K would indicate a minimum velocity required to potentially cool the cylinder.

$$\overline{Nu_D} = 0.68\ Re^{1/2}\ Pr^{1/3} = \frac{\bar{h}D}{k}$$

$$\frac{Q}{A} = \bar{h}(T_s - T_\infty)$$

$$Re = \frac{\rho U D}{\mu}$$

$$\Pr = \frac{c_p \mu}{k}$$

Table 38: The constants associated with a simple analytical model for a cylinder with constant heat generation.

Q	1.83 MW
A	0.1885 m^2
D	0.2 m
k	1 W/m K
T_s	1200 K
T_∞	750 K
ρ	2000 kg/m^3
μ	0.008 kg/m s
c_p	2365 J/kg K

The resultant velocity associated with the constants in Table 38 is the following velocity required to meet a surface temperature of 1200 K with a constant heat generation of 1.83 MW.

$$U = 113.41\ m/s$$

Appendix D: Data Tables

D.1 "Sandwich" design: The first iteration

Table 39: The energy deposited in the target structures for the first iteration of the "Sandwich" design.

		Energy Deposited (kW)
	Slowing Down cylinder	45.7
Plates	1st	87.6
	2nd	92.6
	3rd	88.2
	stopping cylinder	838.6

Table 40: The neutron counts for the first iteration of the "Sandwich" design with the percentage of neutrons based on direction, radially, back up the proton beam window and through the bottom of the target.

	count	percent
radial	1.6410E+08	92.37%
window	2.8464E+06	1.60%
bottom	1.0709E+07	6.03%
total	1.7766E+08	

The first design iteration used an inlet and outlet cross sectional area of 38.5 cm^2.

Table 41: The maximum temperatures associated with the various target structures for the "Sandwich" design the first iteration from FLUENT. All temperatures are in Kelvin and other values are specified.

		Plate				
inlet velocity (m/s)	Slowing Down cylinder	1st	2nd	3rd	bottom cylinder	inlet pressure (Pa)
1	1602.08	2003.14	2052.82	2294.33	5000	7,563.36
2.5	1397.42	1481.67	1503.90	1719.65	5000	31,450.19
5	1321.81	1319.83	1324.03	1404.10	5000	124,597.70
7.5	1295.81	1241.18	1253.89	1304.65	5000	279,459.28
10	1282.20	1196.54	1217.11	1253.26	5000	496,469.31
12.5	1274.12	1175.02	1194.95	1228.08	5000	781,666.13
15	1268.79	1160.68	1179.01	1204.33	5000	1,114,554.30
17.5	1264.90	1149.59	1167.27	1189.93	5000	1,521,205.00
20	1261.96	1141.25	1157.94	1177.79	5000	1,998,174.10

D.2 "Sandwich" design: The second iteration

Table 42: The energy deposited in the target structures for the 2nd iteration of the "Sandwich" design as well as the energy density values and the ratio of those densities.

			Energy Density (W/m^3)		
	Target Structure	Total Energy Deposited (kW)	Average	Peak	ratio (peak/avg)
Slowing Down Cylinders	1st cylinder	19.7	1.792E+07	5.135E+07	2.87
	2nd cylinder	28.9	2.628E+07	8.577E+07	3.26
Primary Target Plates	1st plate	88.3	2.811E+08	1.422E+09	5.06
	2nd plate	93.2	2.967E+08	1.422E+09	4.79
	3rd plate	88.6	2.820E+08	1.422E+09	5.04
Stopping Cylinders	3rd cylinder	401.1	2.553E+08	1.422E+09	5.57
	4th cylinder	236.6	1.506E+08	1.422E+09	9.44
	5th cylinder	90.4	5.755E+07	1.422E+09	24.71

Table 43: The neutron and proton counts for the second iteration of the "Sandwich" design with the percentage of neutrons or protons per direction

	Neutrons		Protons	
	count	percent	count	percent
radial	1.71E+08	84.49%	n/a	n/a
window	7.56E+06	3.73%	n/a	n/a
bottom	2.39E+07	11.78%	1.59E+04	1.59%
total	2.03E+08		1.00E+06	

Table 44: The maximum temperatures associated with the target structures for the second iteration of the "Sandwich" design.

			max temperatures (Kelvin)							
flow rate (gal/sec) by section			slow down cylinders		plates			stopping cylinders		
slowing	plates	stopping	1	2	1	2	3	1	2	3
14.17	14.17	14.17	915.67	967.97	1140.32	1159.06	1140.88	5000.00	2665.80	1505.57
14.17	14.17	21.25	918.35	967.89	1137.99	1144.31	1141.95	5000.00	2607.90	1487.79
14.17	14.17	28.33	915.67	967.57	1141.46	1164.37	1141.10	5000.00	2583.00	1477.58

D.3 "Sandwich" design: The third iteration

Table 45: The energy deposited in the third iteration of the "Sandwich" design with the energy density values. In addition the flow separator values are given.

			Energy Density (Watts/cubic meter)		
	Target Structure	Total Energy Deposited (kW)	average	peak	ratio (peak/avg)
	window	2.32E-01	5.414E+05	1.529E+06	2.82
Slowing Down Cylinder	1st cyl	15.9	1.446E+07	2.276E+07	1.57
	2nd cyl	24.5	2.230E+07	4.506E+07	2.02
	1st sep	7.65E-04	1.949E+06	8.593E+06	4.41
Target Plates	1	86.4	2.751E+08	1.161E+09	4.22
	2	90.3	2.873E+08	1.137E+09	3.96
	3	83.8	2.667E+08	1.008E+09	3.78
	4	73.7	2.347E+08	7.862E+08	3.35
	5	62.5	1.991E+08	6.180E+08	3.10
	6	53	1.688E+08	4.995E+08	2.96
	7	44.5	1.417E+08	4.042E+08	2.85
	8	37.3	1.188E+08	3.119E+08	2.62
	2nd sep	7.07E-03	1.799E+07	1.051E+08	5.84
Stopping Cylinders	1st cyl	78.8	7.169E+07	2.815E+08	3.93
	2nd cyl	23	2.092E+07	4.110E+07	1.96
	3rd cyl	17.5	1.594E+07	3.305E+07	2.07
	3rd sep	4.67E-04	1.190E+06	4.165E+06	3.50

Table 46: The proton and neutron count tallies for the third iteration of the "Sandwich" design. The percentage of neutrons and protons per direction is also shown.

	Neutrons		Protons	
	count	percent	count	percent
radial	1.30E+08	92.10%	n/a	n/a
window	5.93E+06	4.20%	4.91E+01	0.0049%
bottom	5.23E+06	3.70%	7.83E+03	0.7825%
total	1.41E+08		1.00E+06	

Table 47: The maximum temperatures and pressure drop associated with the Slowing Down cylinder cooling section.

		max temp		
flow rate (gallons/sec)	Reynolds	Top cylinder	Bottom cylinder	pressure drop (Pa)
0.03	130	1,372.55	1,468.34	4.48
0.14	650	1,108.12	1,203.49	57.09
0.28	1300	1,056.48	1,151.25	183.93
1.42	6500	867.95	915.40	5,881.88
2.83	13000	892.48	945.83	13,842.09
14.17	65000	868.90	900.10	279,898.14

Table 48: The feasibility of using a 1 centimeters thick plate for the third iteration under the maximum energy density values obtained. Additionally the pressure drop and convection coefficient are shown.

flow rate (gal/sec)	Reynolds Number	pressure drop (Pascals)	maximum plate temp (K)	average outlet temp (K)	convection coefficient (W/m2/K)
0.872	3,000.00	52.61	2,220.09	751.003	2,513.92
4.359	15,000.00	331.24	1,889.78	750.648	3,189.55
8.718	30,000.00	729.87	1,788.22	750.457	3,569.32
43.588	150,000.00	6,006.09	1,631.26	750.127	4,322.35
87.177	300,000.00	15,892.02	1,492.91	750.064	5,350.74
435.884	1,500,000.00	286,618.70	1,296.56	750.013	7,744.41

D.4 "Sandwich" design: The fourth iteration

Table 49: The energy deposited in each target structure in kW as well as the energy densities and the ratio between peak/average.

					Energy Density (W/m^3)		
		tally	raw data	kW	average	peak	ratio
	window	16	4.78E-05	1.340079	1.219E+06	1.038E+06	0.851676
Slowing Down Cylinders	1st cyl	26	0.000564	15.83523	1.440E+07	1.885E+07	1.308608
	2nd cyl	36	0.000769	21.58728	1.963E+07	3.000E+07	1.528082
	sep	46	0.000132	0.675645	1.580E+06	3.089E+06	1.955303
Plate Section 1	plates	56	0.001683	6.746115	4.295E+07	6.388E+07	1.487304
		66	0.002225	8.91831	5.678E+07	1.060E+08	1.866341
		76	0.010475	41.98342	2.673E+08	1.058E+09	3.956728
		86	0.011439	45.84662	2.919E+08	1.087E+09	3.722931
		96	0.01178	47.21371	3.006E+08	1.132E+09	3.767581
		106	0.011885	47.63173	3.032E+08	1.087E+09	3.585445
		116	0.011662	46.73998	2.976E+08	1.039E+09	3.492635
		126	0.011315	45.35084	2.887E+08	9.838E+08	3.407437
	sep	136	0.002948	15.079	3.526E+07	3.467E+08	9.833085
Plate Section 2	plates	146	0.010702	42.8904	2.730E+08	9.042E+08	3.311591
		156	0.010346	41.4668	2.640E+08	8.383E+08	3.17537
		166	0.009919	39.75403	2.531E+08	8.053E+08	3.18182
		176	0.009485	38.01569	2.420E+08	7.582E+08	3.132749
		186	0.009011	36.11491	2.299E+08	6.878E+08	2.99166
		196	0.008533	34.20098	2.177E+08	6.431E+08	2.95343

		206	0.008026	32.16602	2.048E+08	6.287E+08	3.069993
		216	0.007536	30.20243	1.923E+08	5.618E+08	2.922114
	sep	226	0.002054	10.50491	2.456E+07	1.987E+08	8.090117
Plate Section 3	plates	236	0.006791	27.21772	1.733E+08	4.744E+08	2.738023
		246	0.006405	25.67152	1.634E+08	4.334E+08	2.652049
		256	0.006042	24.21714	1.542E+08	4.079E+08	2.645787
		266	0.005684	22.77887	1.450E+08	3.818E+08	2.632856
		276	0.005335	21.38099	1.361E+08	3.622E+08	2.661039
		286	0.005036	20.18552	1.285E+08	3.168E+08	2.465098
		296	0.00481	19.27962	1.227E+08	3.083E+08	2.511578
		306	0.004706	18.86168	1.201E+08	2.914E+08	2.426741
	sep	316	0.002005	10.2579	2.399E+07	1.550E+08	6.461416
Stopping Cylinders	3rd cyl	326	0.001008	28.27067	2.571E+07	4.913E+07	1.910796
	4th cyl	336	0.000704	19.7562	1.797E+07	3.170E+07	1.764532
	5th cyl	346	0.000564	15.82555	1.439E+07	2.117E+07	1.470544
	sep	356	0.000651	3.329044	7.785E+06	2.182E+07	2.803075

Table 50: The neutron and proton counts per direction for the fourth iteration as well as the associated percentages.

	Neutrons		Protons	
	count	percent	count	percent
radial	1.48E+08	92.38%	n/a	n/a
window	6.33E+06	3.96%	33.91362	0.0034%
bottom	5.86E+06	3.67%	6750.316	0.6750%
total	1.60E+08		1.00E+06	

Table 51: The FLUENT results for the 0.5 centimeters target plate feasibility study with mono-directional flow across a target plate with maximum energy density determined from MCNPX.

flow rate (gal/sec)	Reynolds	max plate temp (K)	average outlet temp (K)	pressure drop (Pa)	average convection coefficient (W/m2/K)
0.109	500	2392.86	782.47	19.47	996.05
0.218	1000	2183.99	765.57	46.29	1162.27
1.090	5000	1834.12	753.13	468.02	1563.55
2.179	10000	1764.40	751.64	1,040.06	1622.28
10.897	50000	1280.39	750.29	16,138.09	2913.23
13.077	60000	1246.29	750.22	23,134.72	3087.92
15.256	70000	1218.16	750.19	30,697.49	3240.30
17.435	80000	1190.50	750.17	36,882.48	3399.97
19.615	90000	1171.59	750.15	45,303.81	3511.61
21.794	100000	1161.89	750.13	54,661.81	3584.17